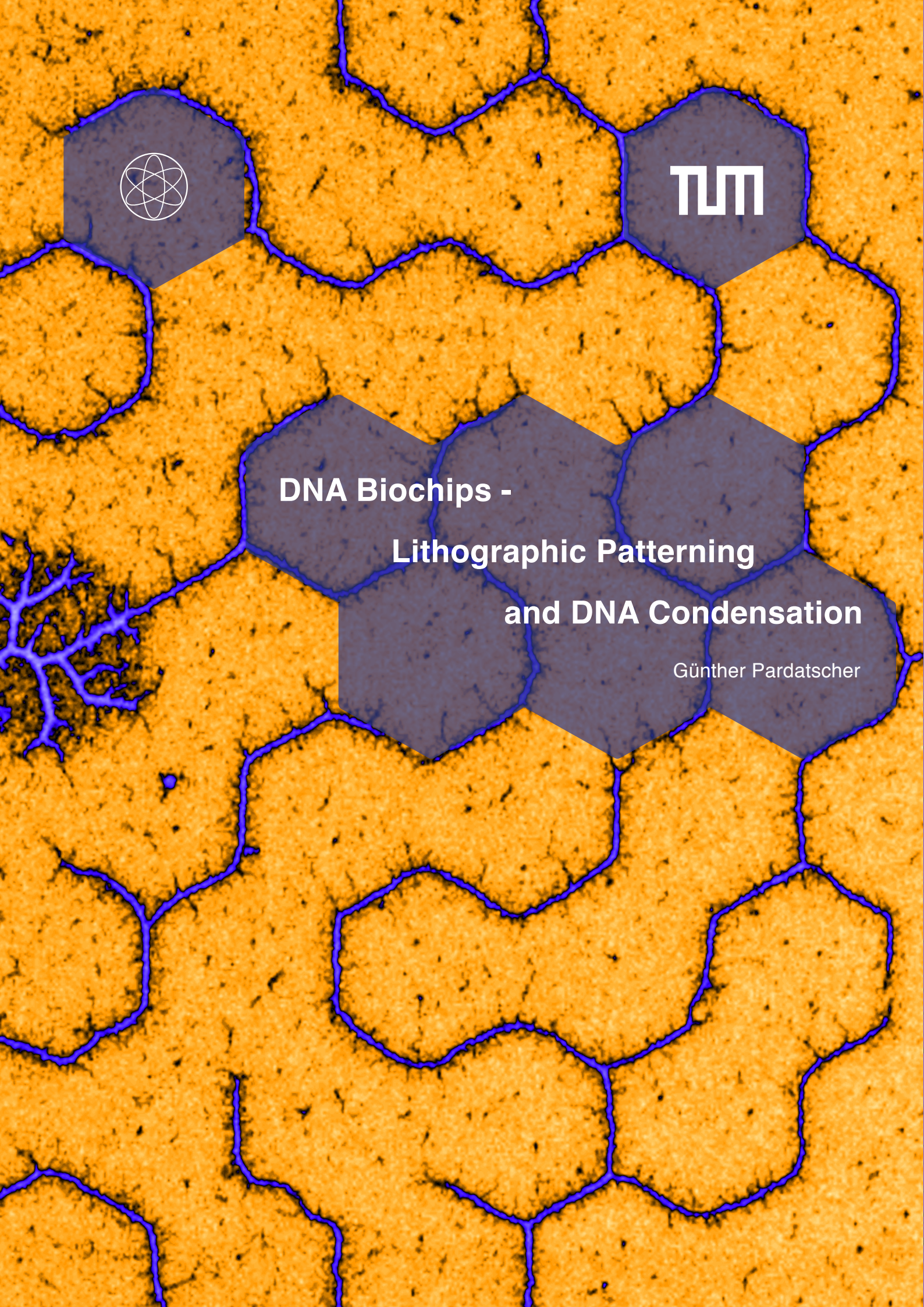

DNA Biochips - Lithographic Patterning and DNA Condensation

Günther Pardatscher

Technische Universität München
Fakultät für Physik
Physik synthetischer Biosysteme

DNA Biochips - Lithographic Patterning and DNA Condensation

Günther Pardatscher

Vollständiger Abdruck der von der Fakultät für Physik der Technischen Universität München zur Erlangung des akademischen Grades eines

Doktors der Naturwissenschaften

genehmigten Dissertation.

Vorsitzender: Prof. Dr. Ulrich Gerland

Prüfer der Dissertation:

1. Prof. Dr. Friedrich C. Simmel
2. Prof. Dr. Hendrik Dietz
3. Prof. Dr. Joachim Rädler

Die Dissertation wurde am 18.01.2018 bei der Technischen Universität München eingereicht und durch die Fakultät für Physik am 13.06.2018 angenommen.

Contents

List of Figures

List of Publications

G. Pardatscher, M. Schwarz-Schilling, S. S. Daube, R. H. Bar-Ziv, F. C. Simmel,
Gene Expression on DNA Biochips Patterned with Strand Displacement Lithography.
Manuscript submitted.

K. Vogele, J. List, **G. Pardatscher**, N. B. Holland, F. C. Simmel, T. Pirzer,
A Self-Assembled Active Plasmonic Waveguide with a Peptide-Based Thermo-Mechanical Switch.
ACS Nano **10**, 11377–11384 (2016).

G. Pardatscher, D. Bracha, O. Vonshak, S. S. Daube, F. C. Simmel, R. H. Bar-Ziv,
DNA condensation in one dimension.
Nature Nanotechnology **11**,1076–1081 (2016).

J. List, E. Falgenhauer, E. Kopperger, **G. Pardatscher**, F. C. Simmel,
Long-Range Movement of Large Mechanically Interlocked DNA Nanostructures.
Nature Communications **7**:12414 (2016).

M. B. Scheible, **G. Pardatscher**, A. Kuzyk, F. C. Simmel,
Single Molecule Characterization of DNA Binding and Strand Displacement Reactions on Lithographic DNA Origami Microarrays.
Nano Letters **14**, 1627-1633 (2014).

A. Kuzyk, R. Schreiber, Z. Fan, **G. Pardatscher**, E. Roller, A. Högele, F. C. Simmel, A. Govorov, T. Liedl,
DNA-based self-assembly of chiral plasmonic nanostructures with tailored optical response.
Nature **483**, 311-314 (2012).

R. Jungmann, M. Scheible, A. Kuzyk, **G. Pardatscher**, C. E. Castro, F. C. Simmel,
DNA origami-based nanoribbons: assembly, length distribution, and twist.
Nanotechnology **22**, 275301 (2011).

Zusammenfassung

Die Immobilisierung von DNA auf der Oberfläche eines Substrates ermöglicht die Untersuchung biochemischer und biophysikalischer Prozesse *in vitro* unter streng definierten Randbedingungen.
Die vorliegende Arbeit beschäftigt sich zunächst mit lithographischen Strukturierungsverfahren zur Befestigung von DNA-Molekülen auf zwei verschiedenen Typen biokompatibler Siliziumchips. Auf sogenannten „Daisy"-Biochips, welche von R. H. Bar-Zivs Gruppe entwickelt wurden, konnten wir DNA nicht nur mittels Photo-, sondern auch durch Elektronenstrahllithographie gezielt anbringen. Außerdem entwickelten wir den sogenannten „Bephore"-Biochip, welcher besonders für mehrstufige Lithographieverfahren geeignet ist und gänzlich aus kommerziell verfügbaren Materialien hergestellt werden kann. Auch Bephore kann mittels Photo- und Elektronenstrahllithographie strukturiert und zu Genexpressionsexperimenten verwendet werden.
Auf Daisy-Chips nutzten wir Elektronenstrahllithographie, um schmale Streifen immobilisierter, 1 μm langer DNA zu erzeugen und diese daraufhin zu kondensieren. Die DNA kollabierte bei der Zugabe von trivalentem Spermidin zunächst nur lokal zu Nukleationskeimen. Diese Keime bildeten anschließend durch die Adsorption benachbarter DNA-Stränge Bündel aus, welche wie in einer Kettenreaktion weiter anwuchsen, bis die Streifen vollständig kondensiert waren. Mit abnehmender Breite der Streifen beobachteten wir einen Übergang von zweidimensionalem, dendritischem Wachstum der Kondensate hin zu eindimensionalen DNA-Bündeln. Das Wachstum dieser Bündel konnte entlang vorgegebener Pfade über viele Mikrometer hinweg gesteuert werden, wodurch sich Kondensate beliebiger Form erzeugen ließen. Zuletzt erforschten wir die Kondensation ausgedehnter Netzwerke aus miteinander verbundenen Pfaden. Wir verfolgten das Wachstum von DNA-Bündeln durch ein labyrinthförmiges Muster und bestimmten daraus den schnellsten Weg durch das Labyrinth. Außerdem regelten wir die Kondensation entlang von Pfaden durch Verzögerungselemente, die einem Modell „stochastischer Schalter" aus der Computerwissenschaft nachempfunden sind.

Abstract

The immobilisation of DNA on a solid substrate enables the *in vitro* observation of biochemical and biophysical processes under strictly defined conditions.

First, we here assembled and characterised brushes of DNA on two types of biocompatible silicon chips. "Daisy"-biochips were developed in R. H. Bar-Ziv's lab to investigate gene expression from lithographically patterned DNA brushes. We augmented the capabilities of the Daisy system with electron beam lithography, thereby increasing the patterning precision from the micrometer- to the nanometer-scale. Additionally, we developed an alternative resist termed "Bephore", which is especially suited for multi-step lithography and assembled entirely from commercially available materials.

On Daisy chips, we applied electron beam lithography to create thin DNA brush stripes and to investigate DNA condensation by trivalent spermidine, *i.e.* the compaction of DNA from a brush-like conformation to a dense, bundled phase. DNA molecules of 1 μm length were patterned as brush stripes of various widths and condensed by the addition of spermidine. Starting in a nucleation site, condensates grew similar to a domino effect by adsorbing neighbouring DNA strands and forming elongated bundles. With decreasing brush width, we observed changes in morphology and condensation dynamics from two-dimensional, dendritic condensates to one-dimensional DNA bundles. In contrast to previously described DNA condensates, 1D bundles could be guided over tens of micrometers along arbitrary pathways.

Eventually, we explored the condensation of extensive DNA brush networks. We tracked bundle growth through a maze-shaped brush to determine the fastest route through the maze. Also, we tuned the propagation of condensation *via* delay elements inspired by a computer model of "stochastic switches".

1 Introduction

The spatial organisation of biomolecules and biochemical reactions plays a significant role in all types of living organisms. On the cellular level of eukaryotes for instance, the segregation of processes in the nucleus and in the cytoplasm opens a variety of options for the regulation of gene expression. Also on larger scales, spatial distributions of molecules called morphogens direct cell differentiation in the embryogenesis of higher organisms, inducing the formation and structuring of tissues, organs or limbs.

The overarching goal of the projects presented hereafter was the generation of biomolecular patterns in an *artificial* environment on a chip, so they could act as a template for biochemical or biophysical processes. In this context we created various types of spatial patterns, combining inorganic and organic materials, top-down semiconductor fabrication, collective transitions of molecules and concepts from computer science. The resulting chip-based, hybrid technologies may bear great potential for the investigation of synthetic biological systems due to their versatility, modularity and the ease of production scaling.

One principal topic was the development and application of biochips, which consist of an inorganic supporting material like a silicon chip or a glass slide, and biological components interacting on the chip. Commercially available biochips are used in biotechnological research and healthcare for high-throughput screening in analytics or diagnostics. For our research project we employed a biochip developed by the group of Roy H. Bar-Ziv with a surface coating termed "Daisy" [1]. It allows for the photolithographically patterned immobilisation of linear DNA and other biomolecules. It was previously used to study physical properties of brushes of DNA [2, 3] or protein expression from gene brushes [4]. We here investigated the patterning of Daisy by electron beam lithography (section 4.1), which enabled the generation of very thin DNA brushes [5]. We further developed an alternative, DNA-based chip coating termed "Bephore", which is well-suited for multi-step lithography and can be assembled entirely from commercially available materials (section 4.2).

In order to create Daisy and Bephore biochips, we first prepared the inorganic chips using techniques primarily developed for semiconductor applications (cutting, etching, cleaning *etc.*). Second, we provided the chips with a biocompatible coating in order to enable biochemical and biophysical processes on the surface, *e.g.* gene

expression from immobilised DNA or DNA brush condensation. "Biocompatibility" mainly implies the prevention or at least a strong reduction of the adsorption of nucleic acids or proteins to the surface. It is often realised *via* a passivation of the substrate by biochemically inert molecules like polyethylene glycol (PEG) or bovine serum albumin (BSA). On top of the passivating molecules, both Daisy and Bephore carry a photo- and electron-sensitive chemical group, which only upon activation allows for the attachment of DNA (figure 1). Different DNA brushes may then interact with each other *via* biomolecular signals encoded in the DNA, thereby potentially mimicking *e.g.* biological structure formation processes.

In the context of generating synthetic biological systems, biochips so far remain largely unconsidered as a platform, in spite of recent demonstrations of compartmentalised oscillating or bistable systems [6, 7]. Most commonly, potential elements for artificial cells, for example genetic circuits, are studied in bulk [8, 9], in steady-state reactor setups [10], in vesicles [11] or in emulsion droplets [12]. While such systems are often easier to generate than a biochip and regarding their encapsulation more similar to biological cells, compartments on a biochip offer various unique properties. Compartments can be fabricated with DNA densities similar to those inside living cells [13] and they may accumulate active biomolecules from a dilute

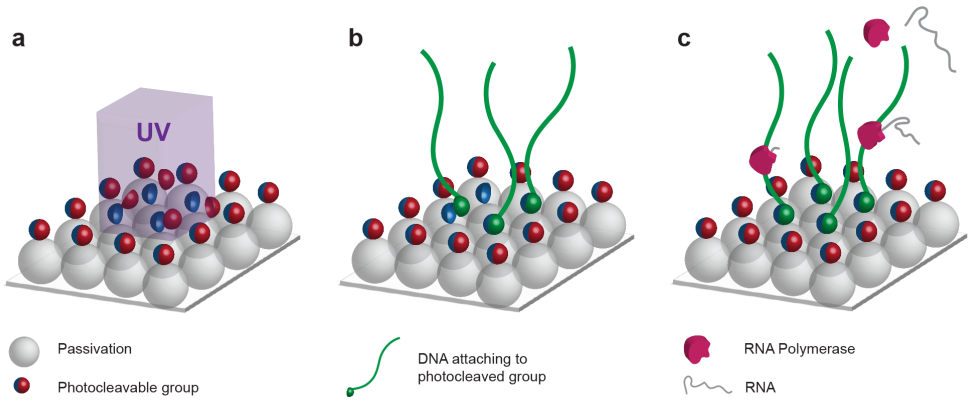

Figure 1: **Photolithographic biochip. a,** Biochips with a photosensitive coating like Daisy or Bephore consist of a solid support like a silicon or a glass chip, and a layer of passivating molecules which carry a photocleavable chemical group or another photoactive molecule. **b,** After illumination with UV light, biomolecules like DNA or proteins can be attached to the activated regions, *e.g. via* streptavidin-biotin interaction (Daisy) or DNA hybridisation (Bephore). **c,** The biocompatibility of the chip enables biochemical processes like the transcription of immobilised DNA to RNA.

cell-free expression system. In contrast to other setups, the immobilised DNA in a compartment is conserved, while nutrients can be exchanged *via* a feeding channel. With a proper supply of nutrients, an immobilised system can run over a long time, in principle as long as the DNA is not degraded. Furthermore, such compartments can be generated in highly reproducible geometries and - in contrast to many types of vesicles or droplets - with biologically inert and non-leaky walls. Hence, biochips may serve as a testing ground for genetic circuits, featuring very controllable and defined experimental conditions. Eventually, we hope that the commercial availability of the Bephore technology will enable more biochip-based research in this direction.

Beyond the mere development of biochip technology, we applied the precision of our electron beam patterning technique on Daisy chips to investigate the condensation of DNA brushes by multivalent ions [5]. Generally, DNA condensation corresponds to processes of DNA compaction induced by multivalent ions, charged proteins, or by DNA-precipitating solvents or chemical agents. In cells, the condensation of DNA plays an important role in the regulation of genes and metabolism, influencing *e.g.* the expression of genes among different cell types in an organism. *In vitro* experiments showed that multivalent ions condense DNA to toroidal or rod-shaped structures [14], while recent work by D. Bracha and R. H. Bar-Ziv on Daisy chips described the formation of dendritic DNA bundles from DNA brushes by nucle-

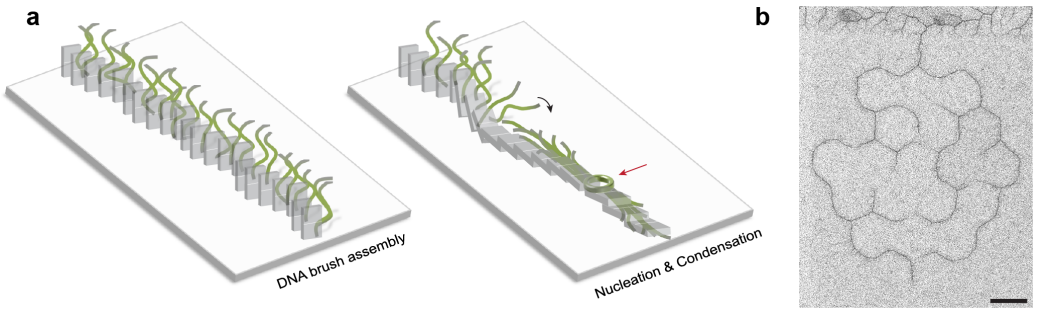

Figure 2: **DNA condensation on a biochip. a,** A linear DNA brush is assembled on an ebeam-patterned Daisy chip. Next, the addition of positively charged, trivalent spermidine induces the spontaneous compaction of several DNA strands into a toroidal nucleation site (red arrow). Similar to a macroscopic domino effect, neighbouring DNA strands subsequently join the condensate, thereby forming bundles of DNA, which grow away from the nucleation site, until all DNA in reach is condensed. **b,** Exemplary scanning electron microscopy image of a small, condensed network of brushes (dark lines) connected to a large area of dendritic condensates (top). Scale bar: 2 μm.

ation and growth [3]. Based on their work, we here applied our ebeam-patterning approach to create very thin DNA brushes and to condense them to linear bundles (section 5). We thereby gained the possibility to guide the bundle growth along arbitrary pathways and even through brush networks (figure 2).
After the characterisation of condensate structure and their formation dynamics, we explored the use of one-dimensional condensation in unconventional approaches to computational problems (section 6), *e.g.* in determining possible solutions for a maze. We therefore created DNA brushes representing the paths of a maze and let the brushes condense from the entrance to the exit. From the propagation of the condensation fronts we could then deduce the shortest path through the maze.
We further investigated the bridging of gaps in DNA brushes by condensation. Inspired by a computer model of stochastic switching circuits [15], we placed gaps in parallel and serial arrangements in order to create systems with predictable probabilities for condensation propagation. Eventually, we hope that such computational condensation schemes will allow for the spatiotemporal regulation and coordination of gene expression on a chip, in addition to conventionally used regulatory proteins or RNAs.

2 Fundamentals

2.1 DNA

In all living cells, DNA is the carrier of hereditary information. It stores the genome, sequences for non-coding RNAs or recognition sites for proteins. Discovered in 1870 by Friedrich Miescher as part of the nucleus [20], its iconic double-helical structure and its associated function as a carrier of information were unveiled in the 20th century (for details see figure 3) [21, 22].
Especially fruitful for the understanding and the study of living organisms as well as for technological applications was the insight into the flow of genetic information in the fabrication of proteins. Figure 4 schematically illustrates the transcription of DNA to ribonucleic acid (RNA) and how a ribosome reads RNA to assemble a protein. In a cellular environment, gene expression actually involves many more

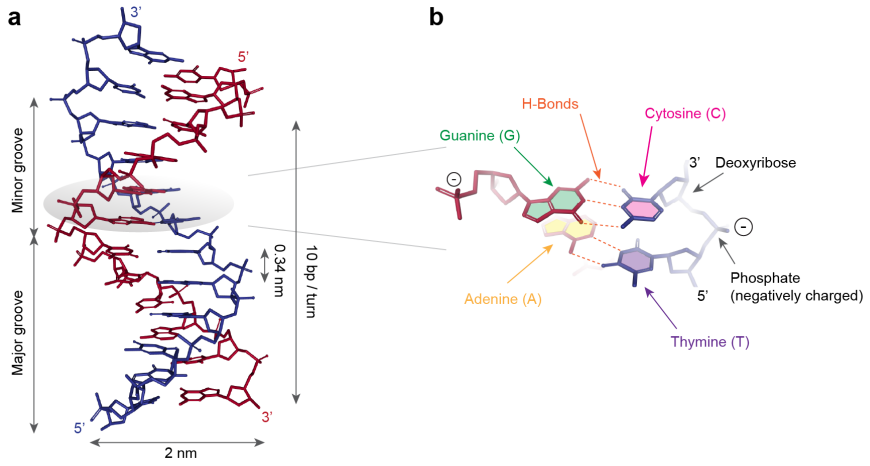

Figure 3: **DNA. a,** Structural details of a DNA double helix formed by two antiparallel strands with complementary base sequences. **b,** A DNA molecule is constituted by a negatively charged phosphate and sugar (deoxyribose) backbone, from which every 0.34 nm one of four bases (ATGC) protrudes towards the centre of the double helix. In regular double stranded DNA the bases are paired by hydrogen bonds as AT and GC (Watson-Crick base pairing). Their sequence contains the building plan for RNA or protein molecules or encodes recognition sites on the DNA itself. The double helix is further stabilised by base stacking interactions and forms a stable rod-like structure with a persistence length of approximately 50 nm and a high linear charge density of approximately $-6e/\text{nm}$.
a&b) Adaptations of: Crystal structure of a DNA sequence d(CGTGAATTCACG) at 130K [16], item 5JU4 from RCSB PDB (www.rcsb.org) [17], created with NGL viewer [18, 19].

components (*e.g.* transcription factors) and additional steps (*e.g.* RNA splicing). Also additional pathways like reverse transcription from RNA to DNA or RNA replication, are possible, yet less common. The understanding of these mechanisms and the emergence of tools to manipulate and synthesize DNA have wide-ranging implications for medical research, healthcare, biotechnology and our society as a whole.

Aside from the immediate application of DNA as a carrier of genetic information, research also focusses on the use of DNA as a building material for nanostructures [23] or as a fuel for DNA-based dynamic systems [24]. Taking advantage of the sequence-specificity of DNA hybridisation, nanostructures of unique geometry, function or optical properties could be generated *via* the self-assembly of oligonucleotides [25–27]. As an alternative to sequence-based nanostructure assembly, few special types of structures like rods or toroids were found to form *via* DNA condensation (section 2.3) [14], and were of special interest for investigations in the field of polyelectrolyte physics.

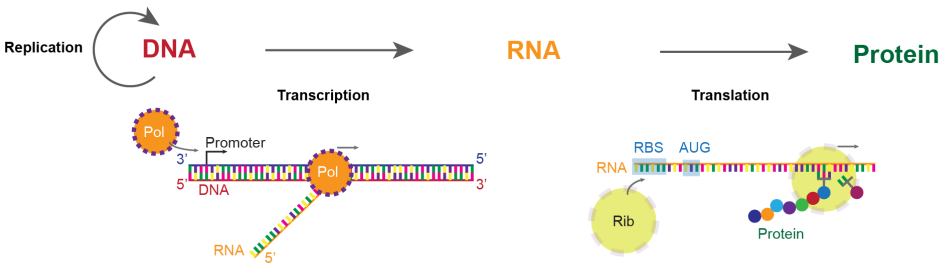

Figure 4: **DNA as a blueprint for protein fabrication.** The base sequence of a gene, *i.e.* a segment of double stranded DNA which starts at a promoter sequence and codes for a protein, is first copied ("transcribed") by an RNA polymerase (Pol) into a single strand of RNA (thymine replaced by uracil, ribose instead of deoxyribose). Next, a ribosome (Rib) binds to the RNA at the ribosome binding site (RBS) and moves along the RNA. At the start codon (AUG), the ribosome begins to assemble a chain of amino acids. Here, one triplet of RNA bases codes for one of the approximately 20 biologically occurring amino acids. Finally, the chain can fold to form a functional protein. In order to preserve the genetic information among dividing cells, DNA is replicated by a DNA polymerase.

2.2 Biochips

In a general sense, a "biochip" corresponds to a solid support (the "chip") carrying immobilised biomolecules which can interact with other molecules in a liquid. Biochips are mostly known for their applications in healthcare and biological research, enabling high-throughput diagnostics or analytics, *e.g.* in the form of DNA or protein microarrays [28, 29]. Such arrays typically consist of hundreds or thousands of sensor fields, each containing DNA, antibodies, receptors or ligands with target-specific base or amino acid sequences for the detection of multiple, fluorescently labelled targets, *e.g.* in gene expression profiling assays. The combination of biochips and microfluidics ("lab on a chip") shows promise as a candidate technology to provide inexpensive diagnostics tools to peripheral hospitals or to low- and middle-income countries.

Beyond the miniaturisation of analytical devices and the minimisation of required sample volumes, also the implantation of biochips into living organisms for *in vivo* diagnostics and/or treatment is extensively investigated [30]. Besides remote powering and privacy concerns, a major challenge in the development of subcutaneous biochips is the requirement for a high degree of biocompatibility. In living organisms, incompatible implants can lead to tissue necrosis or provoke immune responses in the form of inflammation, long term allergic reactions or the walling of the implant by formation of fibrous tissue. More generally, passivated, biocompatible chips display surfaces which prevent the unspecific attachment of biomolecules or cell adhesion. Biocompatibility is therefore essential for almost any biochip technology, especially to provide specificity and sensitivity in biomolecule sensing.

In the context of synthetic biology, biochips were used to investigate gene expression systems [4], to imitate biological processes in an artificial environment [3] or to determine viable routes towards the generation of synthetic, cell-like systems [6].

A special type of photolithographic biochip was developed by the group of Roy H. Bar-Ziv [1]. The biochip was fabricated by coating a silicon dioxide surface of a substrate (Si/SiO_2 chip or glass slide) with a monolayer of heterobifunctional "Daisy"-molecules (figure 5). Biocompatibility is provided by a polyethylene glycol backbone, which prevents the unspecific adhesion of biomolecules to the silicon dioxide. The lithographic capabilities originate in the 6-nitroveratroyloxycarbonyl (NVOC) headgroup of the Daisy molecule, which can be cleaved by photochemically induced isomerisation [31]. Subsequent spontaneous decarboxylation exposes a primary

amine for functionalisation, *e.g. via* the conjugation of a N-Hydroxysuccinimide (NHS) ester of biotin to the amine. Biotin-labelled DNA or proteins are then attached *via* streptavidin to UV-exposed and functionalised regions on the chip.
The immobilisation of dsDNA results in the formation of brushes with DNA densities comparable to *E. Coli* [13]. Depending on salt conditions and DNA grafting density, long DNA strands adopt different conformations. At very low salt concentrations (ionic strength $\lessapprox 5$ mM), 1 kbp DNA stretches out to almost its full length due to osmotic pressure of the ions. In contrast, a brush at high ionic strength ($\gtrapprox 50$ mM) adopts a "mushroom-like" state, in which its extension is well described by a worm-like chain model, unless the density is high enough that size exclusion effects play a significant role [13]. In the range between high and low salt concentrations, the competition of DNA entropy and osmotic pressure determine the amount of DNA stretching.
If DNA brushes carry genes, proteins can be expressed in *E. Coli* extract [1] or in reconstituted gene expression systems (*e.g.* PURExpress® [32]). In combination with microfluidics, gene brushes can be arranged to create dynamic, *e.g.* oscillating or bistable systems [6, 7], which can be considered primitive types of chip-based artificial cells.

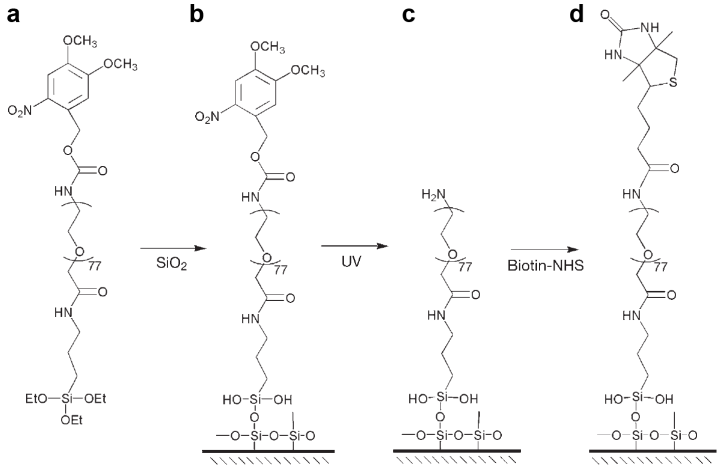

Figure 5: **The Daisy molecule. a,** Chemically synthesized heterobifuncitonal polyethylene glycol ("Daisy"). **b,** Immobilised on a SiO_2 substrate. **c,** UV light (365 nm) cleaves the headgroup, exposing a primary amine. **d,** Functionalisation of the amine with NHS-biotin. Adapted from Buxboim, A. *et al.* [1]. Copyright 2007 Wiley-VCH Verlag GmbH & Co. KGaA, Weinheim.

2.3 DNA Condensation

2.3.1 DNA Condensation in Biology

DNA carries information at a high density, yet the amount of information required to run a living system inflates the molecule to macroscopic dimensions. The 46 human chromosomes contain billions of basepairs of DNA [33], which guide the development of a human from a fertilised egg to an adult. Laid out as a linear thread, this DNA would stretch over more than a meter, and even as a random coil it would span hundreds of micrometers (worm-like chain model). Considering not only its length, but also its large persistence length of ≈ 50 nm and its high charge density (see also section 2.1), it is not surprising that cells employ a variety of proteins to compact and organise the DNA in the cell nucleus which spans only micrometers in diameter. In addition to the compaction, the cellular condensation machinery also influences the accessibility of DNA and is hence involved in the regulation of transcription and metabolism.

In most eukaryotic cell types, DNA is condensed mainly by proteins called histones which form an octameric protein core (figure 6). DNA interacts with the histones

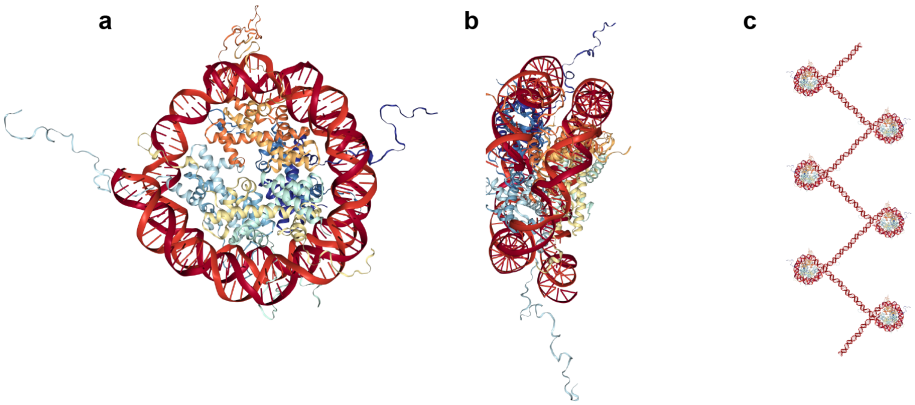

Figure 6: **Nucleosomes.** In order to densely pack DNA in the nuclei of eukaryotes, DNA (red double helix) is coiled around an octameric histone core (displayed as ribbons; **a,b**: viewed from different angles). Protein tails protrude from these so-called nucleosomes, adding potential functionalities to the complex. **c,** Many such nucleosomes are connected like "beads on a string". *In vivo*, nucleosomes are however not arranged in this conformation, but rather in a 5- to 24-nm-thick, flexible chromatin chain [34].
a&b) X-Ray Structure of the Nucleosome Core Particle [35], item 1KX5 from RCSB PDB (www.rcsb.org) [17], created with NGL viewer [18, 19]. c) Adaptation of a).

via approximately 140 hydrogen bonds and *via* electrostatic attraction between the negatively charged DNA backbone and positively charged amino acids (mainly lysine and arginine). Long DNA winds around many such protein cores, thereby forming a sequence of so-called nucleosomes separated by up to 200 bp, similar to "beads on a string" [36, p211]. Histones are highly conserved among species, but post-translational covalent modifications and protein variants with slightly altered amino acid sequences allow for a high degree of specialisation beyond the mere compaction of DNA. Only recently scientists found that the DNA and nucleosomes are further compacted to form a 5- to 24-nm-thick disordered, granular fibre, which constitutes the chromosome in a non-dividing cell (interphase) [34]. In a dividing (mitotic) cell, the complex of DNA and proteins (chromatin) is condensed further and organised in the well-known X-shaped chromosome structure. Aside from the different phases in a cell cycle, some parts of chromatin are generally only moderately condensed (euchromatin), allowing for gene expression from the contained DNA, while other regions (heterochromatin) are highly condensed. The effect of this strong condensation was experimentally demonstrated by the transfer of a gene from a euchromatin region to heterochromatin, after which the gene was effectively silenced [36, p220]. Interestingly, the chromatin structure is not identical among individuals of a species and is inherited by daughter cells. The structure of condensed chromatin hence represents another type of inheritable information [36, p231].

In prokaryotic cells, the DNA is organised in the so-called nucleoid, a region of dense chromatin which - in contrast to eukaryotes - is not separated from the cell plasma by a membrane. In bacteria, proteins structure the DNA at various length scales. At the nanometer-scale, bending, bridging, looping or aggregation are induced by proteins like the integration host factor (IHF), histone-like nucleoid structuring proteins (H-NS), histone-like protein HU or the curved DNA binding protein A (CbpA) [37]. At larger scales, chromatin is compacted for instance by DNA supercoiling or by complexes of non-coding RNAs and nucleoid-associated proteins, which bridge cruciform DNA structures [38]. At the cellular scale, a set of proteins interacts with both the DNA and the replication machinery in order to spatially organise the nucleoid in different phases of the cell cycle [37].

The processes discussed above for eukaryotes and prokaryotes create a dense form of DNA and protein, but the chromatin often neither displays spatial periodicity nor does it arrange DNA in its the densest possible form. Yet, DNA with periodic order was observed in a variety of viruses, prokaryotic and eukaryotic cells, where

condensed chromatin partially displayed cholesteric or even columnar hexagonal order.

In an ideal cholesteric arrangement (figure 7a), all strands lie in planes perpendicular to one direction (cholesteric axis), while the strands' orientation in the planes is different from plane to plane, yet repeats itself periodically along the cholesteric axis with the so-called helical pitch. In cells, a cholesteric structure typically consists of stratified, arced chromatin with a helical pitch of 50-400 nm [40, sec2.5], which was observed *via* polarised light microscopy or transmission electron microscopy (figure 7b). Similar to heterochromatin, also cholesteric chromatin does not allow for gene expression, which means that this structure is mainly found in DNA regions with intentionally suppressed gene expression or in cells in a "dormant" state, *e.g.* under harsh environmental conditions. Therefore it is not surprising that cholesteric order was observed in: some bacteria (*e.g.* *Escherichia coli* or *Rhizobium*) in an inactive, stationary phase; in mitochondria of encysted protozoa; in unicellular algae (dinoflagellates) with parts of their chromatin condensed throughout the cell cycle; and in sperm cells of many higher organisms, whose only task is the delivery of hereditary information, but not its read-out. In some of the examples, the cholesteric structure was only observed locally or under certain conditions, or as a periodic lamellar organisation without the arced pattern [40, sec2.1].

Columnar hexagonal packing was observed in some sperm cells and in several bac-

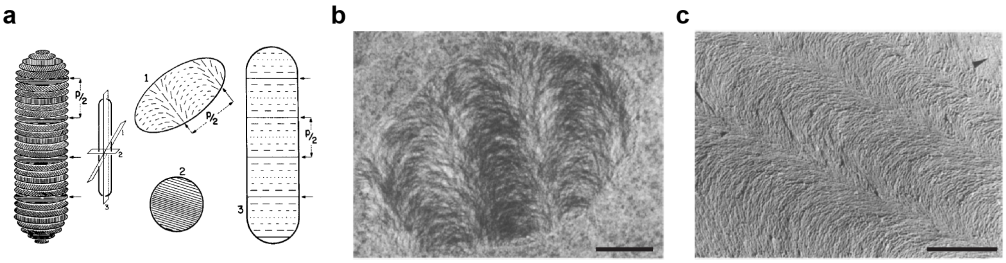

Figure 7: **Cholesteric phases of DNA. a,** Ideal cholesteric order: In each plane perpendicular to the cholesteric axis, strands are oriented in parallel (slice 2), but orientation of the strands varies from plane to plane (slice 1). Yet, along the cholesteric axis (slice 3), the orientation repeats with the helical pitch p or $p/2$, if the strands are invariant to a rotation of 180°. **b,** Chromosome of dinoflagellate *Prorocentrum micans* in transmission electron microscopy showing nested arcs. **c,** Cholesteric phase of DNA obtained *in vitro* from high concentrations of DNA. Both images b&c display a similar organisation of dense DNA. Scale bars: b, 200 nm; c, 1 μm.
Adapted from Rill, R. L. *et al.* [39] with permission of Springer.

teriophages (*e.g.* T4, T7, ϕ29) *via* X-ray diffraction or cryo-electron microscopy [40, sec2.2]. In all the examples mentioned above, which display cholesteric or hexagonal order, the chromatin does not contain the "classical", nucleosome-forming histones or at least not in high amounts. While histones are anyway not present in prokaryotes or bacteriophages, in mature sperm nuclei they are replaced by other proteins, especially by short and positively charged sequences of amino acids called protamines, which insert into the DNA's grooves [36, p1293, 40, sec2.5.1].
We have seen that - in one way or another - DNA condensation plays a role in most biological systems, from viruses to higher eukaryotic organisms. This process thereby intricately entangles the necessary compaction of the information-bearing molecule with the regulation of its read-out, and in some cases it even adds an additional layer of inheritable information. While the investigation of its biological effects typically requires studies *in vivo*, dense states of DNA are also accessible under controlled laboratory conditions *in vitro*, facilitating the description of the more physical aspects of condensation discussed in the following sections.

2.3.2 Condensates from Polyelectrolyte Solutions

In vitro condensates are formed from purified DNA and a condensing agent, *i.e.* typically a positively charged, multivalent molecule. The condensing agent not only screens the negative charges of a single DNA molecule, but also acts as a bridge between two adjacent DNA strands (see also section 2.3.4). So far, polyamines like spermidine (3+) [14] or spermine (4+) [41], metal ion complexes like hexaamminecobalt (3+) [42], cationic lipids [43] and polymers [44], or proteins like histones and protamines [45] have been applied for *in vitro* DNA condensation. Furthermore, polyethylene glycol or ethanol can induce aggregation and precipitation, or condensation of DNA [46, 47]. In contrast, a de-condensation process of dense phases of DNA can be induced by the addition of mono- or divalent positive ions like sodium or magnesium which displace the multivalent condensing agents.
Condensate structure strongly depends on the concentration of DNA. From highly concentrated solutions, DNA can condense to cholesteric (figure 7c) or - at even higher concentration - columnar hexagonal phases, which were observed by polarised light microscopy or electron microscopy [39, 48].
Structures of different morphologies were found to condense from dilute solutions, namely rod-shaped, spheroidal or toroidal nanostructures [14, 47, 49]. Major scien-

tific interest has since focussed on toroidal condensates. On the experimental side, toroids could be created in a range of sizes using a variety of condensing agents and were considered a potential candidate for gene delivery applications [43]. On the theoretical side, in contrast to rods or spheroids, the toroidal geometry with its distinct inner and outer diameters seemed extraordinarily suited for the validation of polyelectrolyte theory. More generally, condensate nanostructures were also considered as a model to explain the high-density packing of DNA into virus capsids [50] or even as hypothetical primordial chromosomes [51, 52].

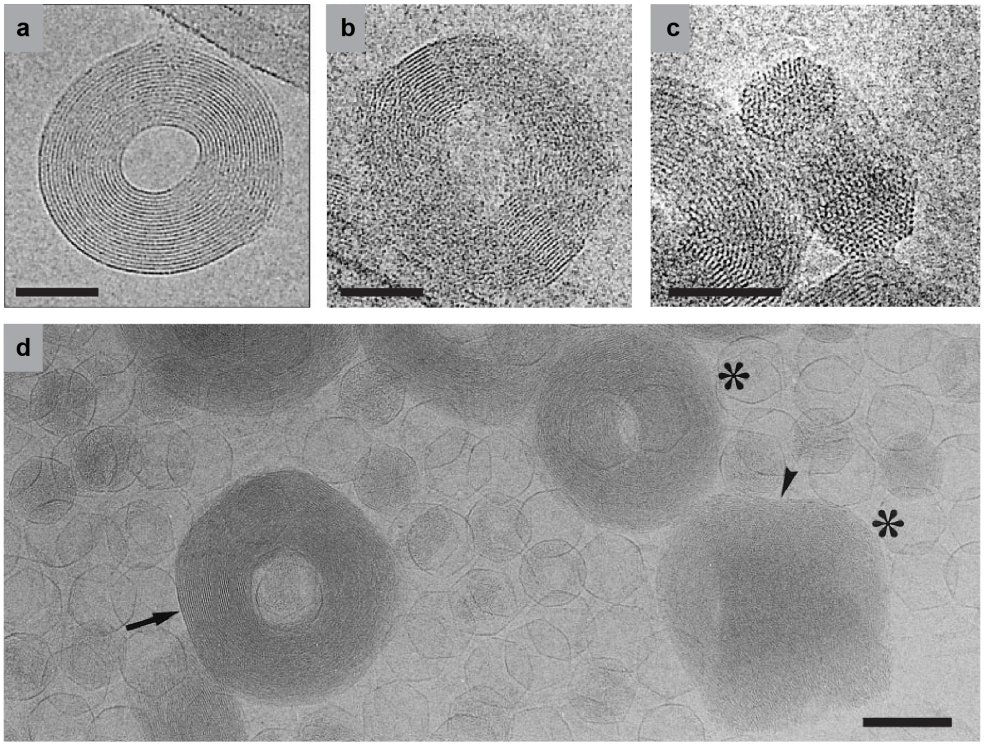

Figure 8: **Condensed DNA toroids. a-c,** DNA toroids condensed by hexaaminecobalt and observed in cryo-electron microscopy. Depending on the orientation of the toroids against the imaging plane, the hexagonal packing of DNA is more or less visible. **d,** Large DNA toroids formed by the spontaneous ejection of phage DNA from their capsids (visible as hexagons) into a solution containing spermine. Also in such large structures, regions with a high degree of order were observed (indicated by arrow and arrowhead). Toroids marked by an asterisk are tilted against the imaging plane. Scale bars: a-c, 50 nm; d, 100 nm.
a-c, Adapted from Hud, N. V. & Downing, K. H. [53]. d, Adapted from Lambert, O. *et al.* [54]. Copyright (a-c, 2001; d, 2000) National Academy of Sciences.

Toroid formation was observed in the presence of hexaaminecobalt, spermidine, spermine or also protamines [55]. Typical condensation experiments use double-stranded DNA of several hundred or thousand basepairs at a nanomolar concentration to be condensed in a solution containing hundreds of micromolar condensing agent and few millimolar monovalent salt [56]. The resulting toroids typically feature an inner diameter of $\approx$ 50 nm and an outside diameter of $\approx$ 100 nm (figure 8a-c). These dimensions, appearing under a variety of experimental conditions, led scientists to believe that the size of the condensates is probably limited by thermodynamics and electrostatics, *i.e.* by the build-up of a net positive or negative charge (over- or undercharging) or energetically unfavourable packing of DNA due to local defects [57]. While these energetic contributions might play a role under some conditions, more recent experiments revealed that also much larger toroids are possible (figure 8d) [54]. DNA released over time from the virus capsids of phages could slowly add to existing toroids, growing them to outside diameters of more than 200 nm. This observation hints at a kinetic limitation of toroid size [57]. Toroid growth is supposedly initiated by the spontaneous formation of a nucleation loop in a single DNA strand, which can subsequently grow by strengthening the loop with the rest of its own DNA and also *via* the adsorption of additional strands [58]. The non-synchronous release of DNA from phage capsids effectively decreases the number of nucleation events by allowing ejected DNA to join already existing toroids. In contrast, the growth of toroids in "normal" experiments without delayed DNA release is only governed by nucleation and accretion rate and therefore yields smaller condensates [57].

Also the inner diameter of $\approx$ 50 nm does not appear to be predetermined by mechanical or thermodynamic properties, but rather by the typical nucleation loop size and the toroid growth [59, 60]. Condensation of DNA with static loops of $\approx$ 25 nm diameter indeed yielded toroids with an average diameter of $\approx$ 25 nm (average of inner and outer diameter) and a thickness comparable to toroids formed without static loops.

The internal structure, *i.e.* the coil-like winding of DNA around the center of the toroid, was investigated early on *via* electron microscopy [61, 62] and X-ray diffraction [63], later especially *via* cryo-electron microscopy [53, 64], which revealed - at least locally - the hexagonal packing of DNA in toroids condensed by spermine or hexaaminecobalt (figure 8c). Models suggest that defects are likely to result from cross-overs necessary in the winding of a continuous strand around a center. Vari-

ations in the degree of order were observed in single structures and among toroids from the same experiment, yet all of them displayed local hexagonal order. Under different salt conditions, larger deviations from the hexagonal lattice might be possible.

2.3.3 Condensation of DNA Brushes on a Biochip

Similar to DNA in solution, also DNA brushes on a biochip (section 2.2) are condensed in the presence of trivalent spermidine. By fine-tuning the concentrations of monovalent salt (*e.g.* few millimolar NaCl) and condensing agent ($\approx$ 60 μM spermidine), Bracha, D. *et al.* could observe DNA of various lengths condense in a first order phase transition. Starting in a spontaneous nucleation event, dendritic DNA bundles grew until they either encountered another condensation domain or the edge of the DNA brush (figure 9) [3]. In contrast to DNA toroids or rods from solution, whose dimensions were on the order of 100 nm, domains of dendritic condensates stretched over tens of microns. Condensates were stable against some dilution of the condensing agent (figure 9c), but changing to a solution containing only monovalent salt dissolved the bundles and restored the brush. The work by Bracha, D. and Bar-Ziv, R. H. laid the ground for the DNA condensation project presented in this thesis.

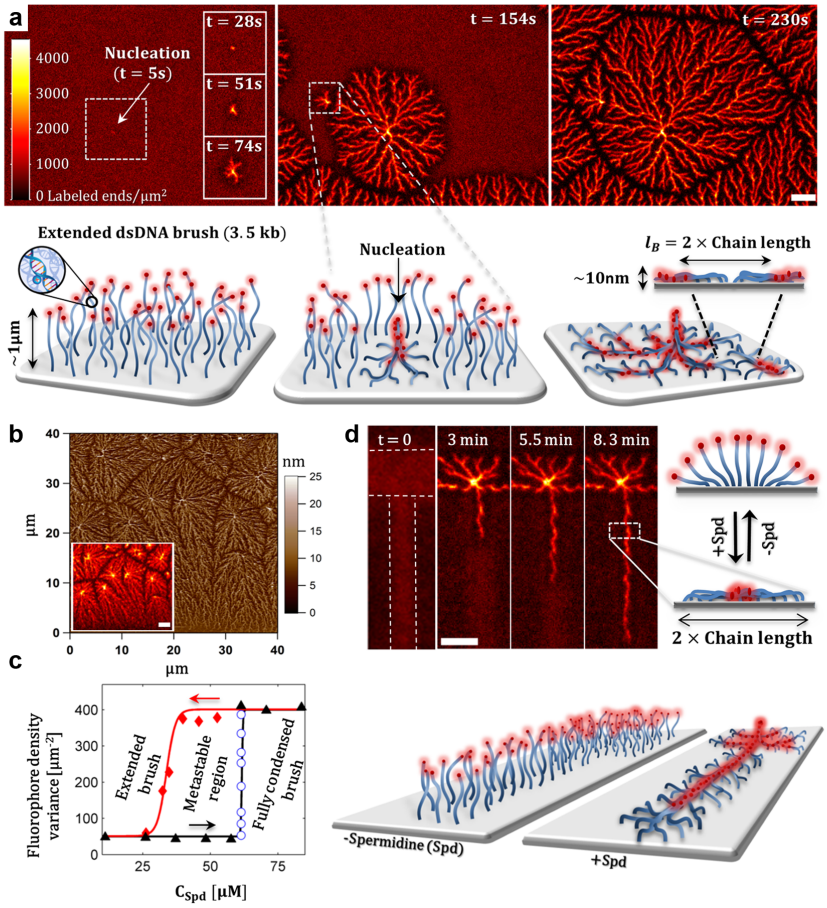

Figure 9: **Dendritic condensation of DNA brushes. a,** Condensation of immobilised and fluorescently end-labelled DNA by nucleation and dendritic growth. The schematic illustrations below the fluorescence microscopy images show the presumed mechanism of growth and domain wall formation (dark areas between condensed domains). **b,** Atomic force microscopy image revealing the topography of a condensed brush; inset: corresponding fluorescence image. **c,** After increasing the spermidine concentration above a critical concentration for condensation (black arrow), DNA bundles were stable against some dilution of the condensing agent (red arrow), revealing a hysteresis effect in condensation. **d,** Taking advantage of the photolithographic capabilities of Daisy, dendritic condensation was directed along a patterned path. Scale bars: 5 μm.
Adapted from Bracha, D. *et al.* [13], originally in [3]. Copyright (2014) American Chemical Society.

2.3.4 Physics of DNA Condensation

Polyelectrolyte condensation is a physical phenomenon which involves several types of charged molecules interacting at short distances in an aqueous environment. In this section, we will start from a traditional description of macro-ions, namely by sketching the Poisson-Boltzmann mean-field theory (based on [65, p98-100] & [66]), and proceed with a qualitative discussion of additional mechanisms involved in DNA condensation.

In water with dissolved salts like sodium or magnesium chloride, ions are evenly distributed by diffusion. The addition of a highly charged macro ion, for instance a charged nanoparticle or a long DNA strand, locally disrupts this even distribution of small, mobile ions and results in the formation of an "ion cloud", more commonly termed the "diffuse layer", around the macro ion. In this context, the Poisson-Boltzmann theory allows for the calculation of the electrostatic potential ψ in the vicinity of the macro-ion. This potential can then give a hint about the nature of the interaction, *i.e.* attraction or repulsion, among two macro ions. For simplification, the solvent (typically water) is treated as a continuous dielectric with the absolute permittivity ϵ (product of relative and vacuum permittivity). Hydration effects are neglected and ions are considered as point charges. A relation between charges and the electrostatic potential is given by the Poisson equation (1).

$$\nabla^2\psi = -\frac{\rho(\mathbf{r})}{\epsilon} \tag{1}$$

The density of free charges ρ (at spatial coordinates $\mathbf{r}$) accounts for the charge densities $n_i(\mathbf{r})$ of all (in total N) ionic species i with valence z_i (e is the elementary charge).

$$\rho(\mathbf{r}) = \sum_{i=1}^{N} e z_i n_i \tag{2}$$

Considering the chemical potential of the ions $\mu_{ic} = kT\ln(n_i/n_0)$ (temperature T, Boltzmann constant k and n_0 setting the zero of the potential), ions close to a macro ion experience the electrochemical potential μ_i.

$$\mu_i = kT\ln(n_i/n_0) + ez_i\psi \tag{3}$$

In equilibrium, the force acting on the ions, *i.e.* the gradient of μ_i, is zero.

$$\nabla\mu_i = kT\nabla\ln(n_i/n_0) + ez_i\nabla\psi = 0 \tag{4}$$

Solving equation (4) for n_i yields the (Boltzmann-) distribution of ions close to a macro ion.

$$n_i = n_0 \exp\left(-\frac{ez_i\psi}{kT}\right) \tag{5}$$

Inserting equation (2) into (1) and replacing n_i by formula (5), one gets the Poisson-Boltzmann equation (6).

$$\nabla^2\psi = -\frac{e}{\epsilon}\sum_{i=1}^{N} z_i n_0 \exp\left(-\frac{ez_i\psi}{kT}\right) \tag{6}$$

The Poisson-Boltzmann equation and slight variations of it are a useful tool to describe the potential close to a macro ion in the presence of small, mobile ions. Eventually however, the solution of the equation always yields repulsive forces among like-charged macro-ions, indicating that this mean field approach does not account for some mechanisms involved in DNA condensation. Several theoretical models have been proposed to explain the counter-intuitive phenomenon [66, 67], but experimental insight into the process at the molecular level is rather scarce.

Instead, a recent publication by Yoo, J. and Aksimentiev, A. tackled some of the most urgent questions [68]. They applied an atomistic molecular dynamics simulation of an array of DNA double-helices in explicit water to investigate forces among DNA strands and molecule distributions under various conditions. Specifically, they simulated DNA in the presence of different ions (chloride ions were always present): a mixture of sodium ions and the condensing agent spermine^{4+}; only sodium; a mixture of sodium and magnesium. The simulation agreed with the available quantitative, experimental data, *i.e.* DNA assembled in a columnar hexagonal lattice with a 28 Å spacing and the internal pressure agreed with measurements of hydration forces [53, 69, 70].

The analysis of their simulation found that condensation is primarily governed by electrostatics. In the presence of spermine ($<$ 1 mM) and sodium (200 mM), the negative charge of DNA is almost entirely neutralised by spermine attaching to the DNA grooves and loosely to the phosphates. The attractive interaction among DNA strands appears to be mediated by non-contact bridging by ions of a valence $\geqslant 3$. This mechanism agrees roughly with previously proposed charge density wave (CDW) models, while a Wigner-crystal-like arrangement of ions was not observed [71]. Pairwise DNA-DNA forces (figure 10) were attractive within a range of 28 - 40 Å with a small free energy change on the order of 0.1 kT per basepair.

Interestingly, changes in entropy by an increase in temperature favour condensation

due to the release of sodium ions. Furthermore, water does not appear to contribute to attractive forces in condensation.

In contrast to such a regular model system consisting of two or more parallel and infinitely long DNA strands, the morphology of actual DNA condensates, *e.g.* toroids, also depends on the formation process. This process involves additional considerations regarding the condensation kinetics, mechanical stiffness, bending and distortions of DNA [67].

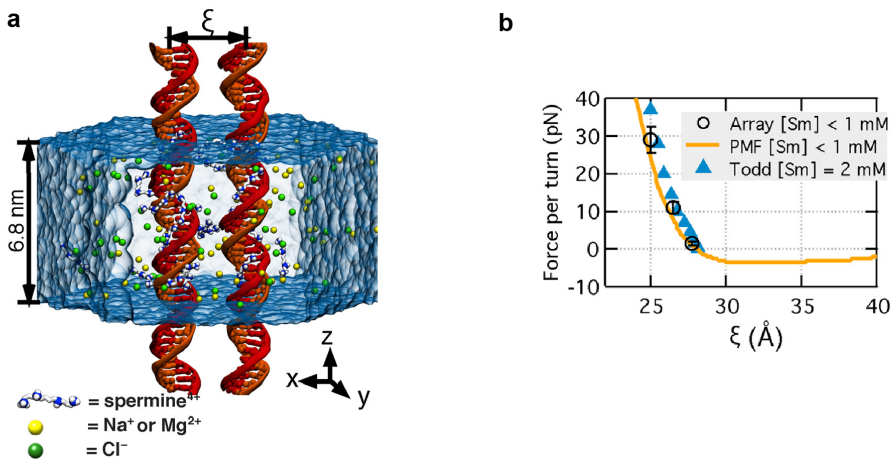

Figure 10: **Molecular dynamics simulation of DNA condensation [68]. a,** Two parallel DNA strands with periodic boundary conditions are simulated at a distance ξ in explicit water containing spermine^{4+}, sodium (Na^+), magnesium (Mg^{2+}) and chloride (Cl^-) ions. **b,** The force per DNA turn is repulsive (positive) at distances $\xi < 28$ Å and attractive (negative) at larger distances. The simulated forces (at spermine concentration [Sm]) for an array of 64 helices and for 2 helices (calculated from the pairwise potential of mean force "PMF") agree well with experimental data ("Todd") [70].
Adapted from Yoo, J. and Aksimentiev, A. [68] by permission of Oxford University Press (2016).

3 Methods and Experimental Procedure

The following sections describe techniques and procedures involved in the fabrication of Daisy and Bephore chips, their patterning *via* electron beam and UV lithography, and the preparation and imaging of experiments. Both types of chips were prepared from oxidised silicon wafers, which were passivated with a layer of Silane-PEG. We here used semiconducting chips, because they are especially suited for patterning by EBL and imaging by reflected light, scanning electron and atomic force microscopy. However, the fabrication procedures should work analogously on glass slides or other silicon oxide surfaces.

3.1 Photo- and Ebeam-Lithography

Lithography was first developed by Alois Senefelder in the late 18th century as a printing technique to produce large amounts of copies of images and illustrations from a stone-based template [72]. Similarly, in the modern production of microelectronics, lithographic methods are applied to transfer a pre-designed pattern onto suitable substrates. Specifically, photo- and electron beam lithography aim at the creation of a relief structure on a polymer-coated substrate (figure 11) by scanning an electron beam over the surface or by masked UV illumination. Thereby, high-

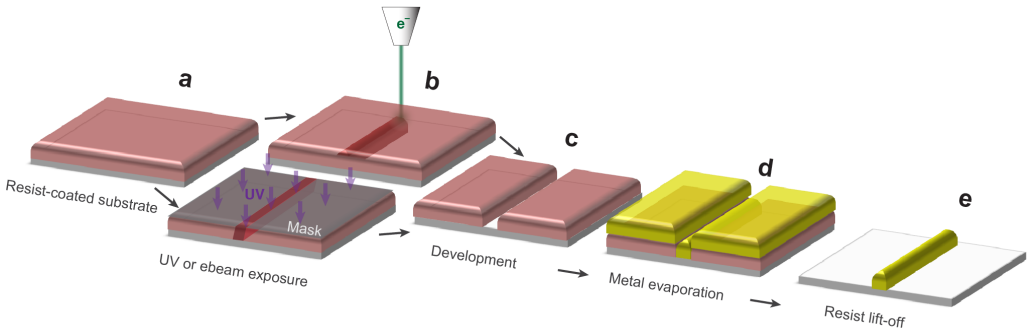

Figure 11: **Typical lithographic process. a,** A semiconducting substrate (*e.g.* a silicon chip) is coated with a positive resist. **b,** Exposure: An electron beam draws a line into the resist (top); a similar line can be generated by masked UV illumination (bottom). **c,** Exposed resist is removed by a solvent ("developer"). **d,** In order to create a nanowire, metal is evaporated on top of the entire substrate. **e,** The removal of the residual resist leaves only the nanowire on the substrate.

energy electrons or photons locally either cleave or crosslink the polymer-coating (also called "resist") and hence change its solubility. In the subsequent development, *i.e.* the immersion of the chip into a suitable solvent ("developer"), resist with a higher solubility is removed, leaving the designed pattern in relief. If the resist is rendered more soluble by the ebeam or UV exposure (positive resist), now the patterned areas display the bare substrate, while the rest of the surface is still covered by resist. For negative resists, only the patterned regions remain covered by resist. After the development, the substrates can be modified for a specific application, *e.g.* by the evaporation of metals, by etching or by chemical functionalisation. The removal of the remaining resist by an additional, stronger solvent ("remover"), yields a substrate, which is modified only in the developed regions.

3.1.1 Electron Beam Lithography

Figure 12 shows an EBL system for the fabrication of nano- and microstructures on suitable substrates [73]. The core of this device is formed by the so-called "column", which contains the electron source and several elements which accelerate, filter, deflect and focus the electron beam. The electron source is formed by a conducting material which emits electrons at high temperatures or in strong electric fields. Schottky field emitters combine heating (thermionic emitter) and field-assisted tunnelling (field emitter) to provide sources with high brightness ($\sim 10^5$-10^9 A/cm^2/sr), small (virtual) source size ($\sim$ 10-25 μm) and low energy spread ($\sim$ 0.2-3 eV). Acceleration voltages of typically 0.1-50 kV, electromagnetic lenses and apertures yield electrons with desired energy, shape the beam and stop stray electrons. The blanking system, which blocks the beam, consists of an electrostatic deflector to allow for fast response times during ebeam exposures. Further components in the column include multipole lenses for the correction of astigmatism, lenses for focussing the beam to a spot of few nanometers in diameter, and the deflectors which direct the beam to a certain position on the substrate or scan it over the surface to perform Scanning Electron Microscopy (SEM).
The stage chamber contains a stage holding the substrates, one or more electron detectors which are required for microscopy and beam alignment, an amperemeter for the measurement of the beam current and possibly other devices for sample manipulation or characterisation during ebeam exposures. Since the deflectors in the column only have a limited range of deflection, the beam can be directed to write

only a certain area ("writefield"). For structures larger than a writefield, several of them need to be stitched by precise, interferometer-controlled stage movement. Arbitrary designs can be created on a computer, which translates the two-dimensional shapes into a path of the ebeam on the substrate. The computer then transfers the required data to the pattern generator, whose high-speed electronics control the lenses and deflectors in order to pattern the substrate according to the design.
The resolution of a typical EBL process is on the order of ≈ 20 nm. When electrons from the incident beam (primary electrons) hit the surface and enter the substrate, they experience (small angle) forward- and/or (large angle) backscattering. In this process the electrons lose energy, which is mainly transferred to secondary electrons with energies of 2-50 eV. These electrons typically travel up to ≈ 10 nm before reacting with resist molecules and are responsible for the bigger part of resist exposure and therefore also for the maximum resolution of EBL.

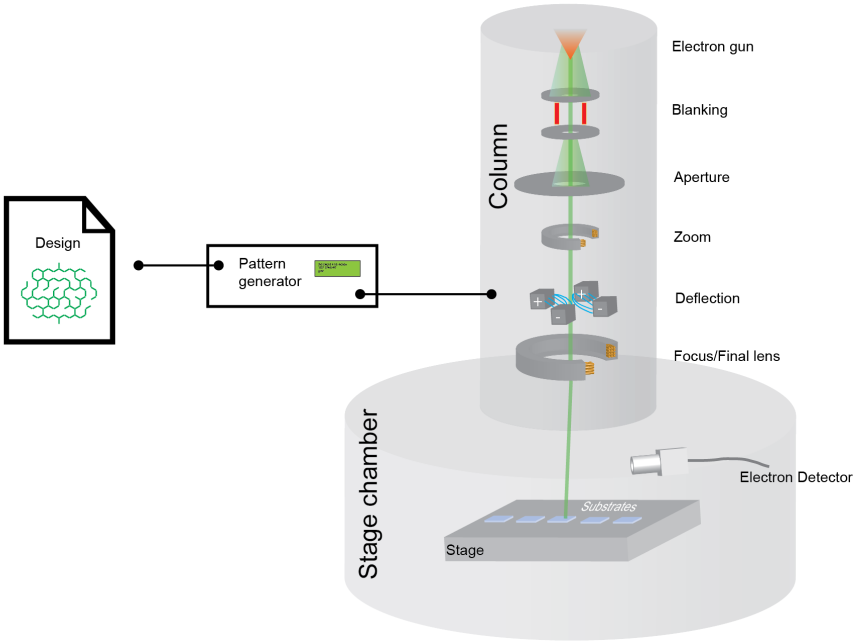

Figure 12: **Electron beam lithography system.** The electron beam is generated in the "column" which consists of the electron gun (source and acceleration) and a system of electromagnetic lenses, apertures and deflectors for shaping and steering the beam. The stage chamber contains the stage with the substrates, an electron detector for SEM and components for the positioning and characterisation of the substrates. The device is controlled *via* a computer and driven by high-speed electronics.

Backscattered primary electrons and few high-energy (≈keV-range) secondaries are responsible for the "proximity effect", *i.e.* the undesired exposure of resist in proximity to the incident beam. While it cannot be totally avoided, modern EBL systems adjust electron doses, when writing adjacent lines, in order to minimise the impact of the effect.
In comparison with other lithographic techniques, *e.g.* masked photolithography, EBL has advantages not only regarding the resolution, but also regarding its versatility, since arbitrary patterns are readily designed and written. However, the serial exposure of patterns - line by line - is rather slow, especially if it comes to large structures. Furthermore, EBL devices are expensive in their acquisition and maintenance, which is why they are mainly used in science and research, for prototyping or in the fabrication of photolithographic masks. Alternative techniques for the fabrication of nano-scale structures include photolithographic systems with illumination sources in the deep UV or even X-ray spectrum, but also nanoimprint, dip-pen or ion lithography.

3.2 Scanning Electron Microscopy

In conventional light or fluorescence microscopy, the resolution in imaging small objects is limited by the wavelengths in the visible spectrum and the numerical aperture of the objective [74, 75]. One way to overcome this limitation is the use of electrons, which can be accelerated in electric fields to much smaller wavelengths (well below 1 Å) than those of visible light.
In Scanning Electron Microscopy (SEM), an electron beam is generated in the same way as in EBL (see section 3.1), which itself requires SEM to align and focus the electron beam for lithography. SEM imaging is performed by scanning the electron beam over the sample surface following a raster pattern, very much like in old cathode ray tube (CRT) displays. As described in section 3.1, primary electrons from the incident beam hit the substrate, get scattered and cause the emission of secondary electrons. While scanning, the currents resulting from these electrons are continuously registered by an electron detector in the stage chamber or in the final lens (inlens detector). Local differences in sample material and topography cause changes in the detected electron currents, which yield the contrast in imaging.
SEM allows for the imaging of samples across several orders of magnitude in size, from millimeter-sized insects over micron-scale cells to nanoparticles of few nanome-

ters in diameter (figure 13). In order to enhance contrast and to avoid the accumulation of charge in insulating substrates, samples can be sputtered with a thin layer of metal, *e.g.* gold or chromium. Alternative techniques, which also achieve resolutions below 100 nm, include Transmission Electron Microscopy (TEM), atomic force microscopy or optical super-resolution techniques.
In the context of this project, SEM imaging was performed without staining or metal coating, using the system's inlens detector and the same parameters as for lithography (acceleration voltage: 5 kV, aperture: 10-20 μm).

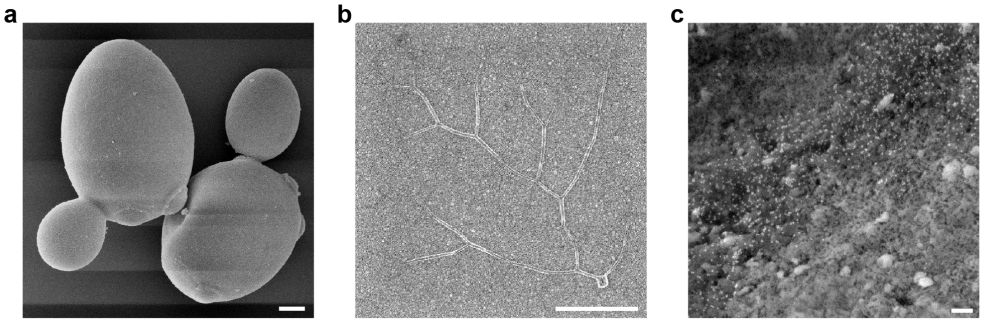

Figure 13: **Scanning electron microscopy (examples).** SEM at different length scales: from micron-sized yeast cells to gold nanoparticles. **a,** Yeast cells dried and imaged shortly before budding (cell division). Round features on their cell walls correspond to bud scars from previous budding events. In order to avoid the accumulation of electrons in insulating materials like these cells, samples need to be sputtered with a layer of metal (here: 20 nm of gold-palladium). Still, stripes and shades indicate some charging. **b,** DNA bundles and a toroidal nucleation site from DNA condensation (see also section 5.1) are observed without additional staining. **c,** Gold nanoparticles (bright dots, 10 nm in diameter) with DNA origami (single sheets, not visible) on a silica particle ($\approx$ 50 μm in diameter). Scale bars: a&b, 1 μm; c, 100 nm.
a, prepared for imaging by Kaian Hoi (Lehrstuhl für Brau- und Getränketechnologie, TU München); c, prepared by Kilian Vogele, as in [76].

3.3 Atomic and Electrostatic Force Microscopy

Atomic Force Microscopy (AFM) is a scanning probe technique, which maps the topography of a sample surface [78]. Figure 14 illustrates the working principle of AFM. The technique is especially suited for the visualisation of small elevations or cavities on an otherwise flat surface, *e.g.* DNA molecules on mica surfaces, but in principle also larger objects like cells can be imaged.
Another scanning probe technique is Electrostatic Force Microscopy (EFM) [79, 80], which probes the electrostatic interaction between a conductive tip and a surface,

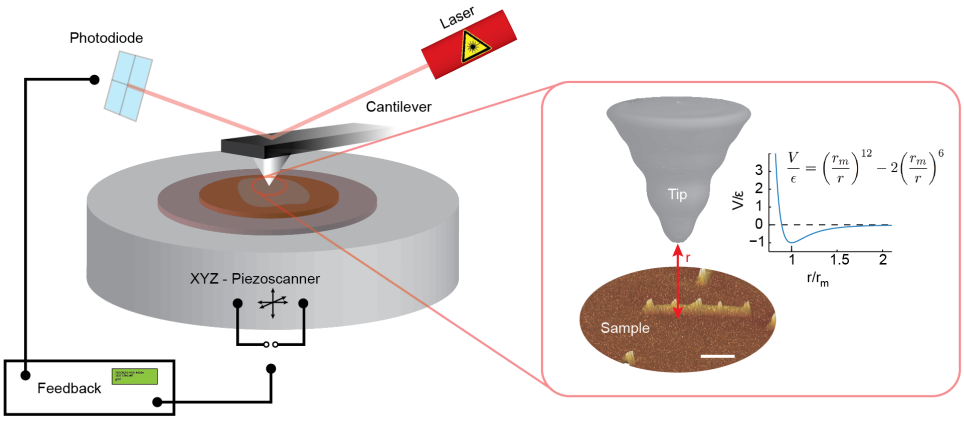

Figure 14: **Atomic Force Microscopy (AFM).** An AFM system typically consists of a piezoscanner, which can position a sample with high precision; a holder, which carries exchangeable cantilevers and, if necessary, uses a "piezo-shaker" to excite a cantilever to oscillate; and a laser which is pointed at the back of the cantilever and whose reflection is monitored by a photodetector. In intermittent contact mode, the oscillating cantilever is brought close to the surface, so the sharp tip at the bottom side of the cantilever taps the surface. Thereby, the oscillation of the cantilever changes with the forces acting between surface and tip. These changes are monitored by the detection system (laser and photodetector). While the piezoscanner moves the sample line by line below the tip (X-Y axes), a feedback system adjusts the height (Z-axis) in order to maintain the force between tip and surface constant. The graph (inset) shows the Lennard-Jones potential V as a function of the distance r (divided by the minimum potential $-\epsilon$ at distance r_m), which describes the typical interaction between two uncharged atoms as a combination of long-distance attraction (van-der-Waals interaction) and short-range, hard repulsion (based on Pauli exclusion principle) [77]. The imaging of atomic or molecular features is possible, since the bulk of the interaction is caused by forces between the atoms at the very bottom of the tip and their closest neighbours on the surface. Here, the sample corresponds to gold nanoparticles on a DNA nanostructure adhered on a mica surface. Scale bar: 100 nm.

while a voltage is applied between them. The working principle of EFM is explained in figure 15. The interaction between a tip and a sample object on an uncharged surface depends on the electrostatic properties of the sample and on the applied voltage. For charged structures on a surface, a change in the sign of the applied voltage typically flips the sign of the interaction, from attractive to repulsive or *vice versa*. On the contrary, polarisable materials always induce an attractive interaction [81]. Hence, EFM allows for the determination of basic electrostatic properties of the surface and for the correlation of topographic and electrostatic information. In principle also a quantitative analysis of EFM measurements is possible [82, 83], but was beyond the scope of this project.
AFM and EFM (Cypher, Asylum Research) images were acquired in air using a conductive cantilever (Olympus AC240TM).

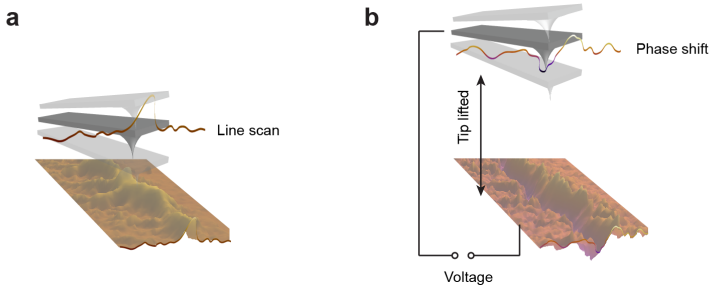

Figure 15: **Electrostatic Force Microscopy (EFM).** EFM imaging is performed in a two-step procedure. **a,** Each line is first scanned in intermittent contact mode (see figure 14 for details) to acquire the topography profile. **b,** Then, the tip is lifted (*e.g.* 50 nm) above the surface and a voltage is applied between the sample substrate (*e.g.* a silicon chip) and the tip. While still oscillating, the tip again scans the line at a constant height above the surface. Thereby, electrostatic interactions between sample and tip influence the cantilever's oscillation. Changes in the phase shift between driving and tip oscillation hint at charged or polarisable surface features.

3.4 Daisy Chips

3.4.1 Fabrication

Silicon wafers (5", 0.525 mm thickness, test grade, <100>, p-type, University Wafers, Boston, MA) were used as biochip substrate. A grid of alignment marks, which were necessary for subsequent alignment of electron beam lithography patterns and the area to be exposed to DNA-containing droplets, was formed by UV laser-writing (μPG101, Heidelberg instruments) on S1805 photoresist (MicroChem, Newton, MA), followed by 2 μm deep etching using ICP- RIE in a similar protocol to previous work [6]. The wafer was divided into a large number of smaller chips. Each chip was coated with a layer of $\approx$50 nm SiO_2 using plasma enhanced chemical vapor deposition (PECVD) with the following parameters: pressure of 1200 mTorr, 5% SiH_4 in He, flow rate of 750 sccm, N_2O flow rate of 1250 sccm, N_2 flow rate of 400 sccm, RF power of 110 W, upper electrode temperature of 200 °C and lower electrode temperature of 300 °C on a Versaline PECVD machine (Plasma-Therm, Saint Petersburg, Florida, USA) for 21 seconds. A biocompatible photosensitive monolayer was then formed by coating the silicon substrates with a trifunctional molecule composed of a polyethylene glycol (PEG) backbone with a protected amine at one end and a triethoxysilyl group at the other end. Coating was performed in toluene (0.5 mg/ml) for 30 min, followed by washing and drying [1].

3.4.2 Electron Beam Patterning

Immediately before ebeam lithography, defective Daisy molecules with unprotected amines were passivated *via* a reaction with Methyl-$(PEG)_8$-NHS Ester (Thermo Fisher Scientific, 6 mg/ml in 200 mM borate buffer, pH adjusted to pH 8.6 using HCl). The difference between passivated and unpassivated chips is displayed in figure 63 in the appendix. After 15 min, the chip was washed thoroughly with DI water and transferred to the ebeam lithography system (eline, Raith). Typically, ebeam patterns were written at an acceleration voltage of 5 kV, a current of approximately 15 pA and a dose of 5 $\mu As/cm^2$ or 30 $\mu As/cm^2$ (mazes). Deprotected amines were then biotinylated using Sulfo-NHS-Biotin (Thermo Fisher Scientific, 0.5 mg/ml in 200 mM borate buffer, pH 8.6). After 15 min, the chips were washed with DI water and stored in dark until use.

3.4.3 Photolithography

Photoactivation of Daisy was performed using an inverted microscope (Zeiss Axiovert 200, Bar-Ziv lab) and a UV light source (EXFO X-Cite 120Q). Alternatively, masked photolithography on dried chips could be carried out in a mask aligner or a similar device. After lithography, exposed regions were functionalised with biotin (see previous section 3.4.2).

3.4.4 DNA Brush Assembly and Fluorescence Imaging

Linear double-stranded DNA with a length of 3130 bp was produced from pIVEX 2.5d template plasmid by a standard PCR procedure using KAPA HiFi™ DNA Polymerase (KAPA Biosystems) and a pair of 5' modified primers, one conjugated to biotin and the other to a fluorescent marker (Alexa Fluor®647 , IDT). DNA was purified *via* a PCR clean-up system (Promega) and was mixed with streptavidin (ThermoFisher Scientific) at a ratio of 1:1.4 respectively, yielding streptavidin-conjugated DNA. Fluorescently labelled (Alexa Fluor®647) streptavidin used in figure 19 was purchased from ThermoFisher Scientific. DNA brushes were assembled by placing a few microliters of DNA solution (80 nM in water, 1 M NaCl) onto the patterned area. From that point onward we carefully avoided drying of the chip. After an incubation time of one hour the chip was washed with a solution of 3 mM NaCl by repeated careful exchange of solution *via* pipetting to ensure the removal of residual DNA and excess NaCl. Finally, the 3 mM NaCl solution was replaced with a solution of 3 mM NaCl and 56 μM spermidine (from spermidine trihydrochloride, Sigma-Aldrich). Nucleation and condensation started a few minutes later and were monitored in an Olympus BX51 upright fluorescence microscope (60× water immersion objective, CoolSnap HQ CCD camera).

3.4.5 Drying Procedures and SEM Imaging

After the completion of condensation, chips were washed thoroughly with ethanol and were either dried in air (mild procedure) or under a nitrogen stream for imaging in Scanning Electron Microscopy (SEM) or Atomic Force Microscopy (AFM). Drying in air by placing the sample under a cover (*e.g.* the top cover of a pipette tip box) preserved the bundles and nucleation sites, but required high magnification

(>10k×, low scan speed) SEM imaging (*e.g.* figures 32b, 33, 46, 66). By contrast, drying in air without cover or under a gentle nitrogen stream, probably due to a faster receding ethanol meniscus, led to some degradation of the bundles, thereby enabling low magnification scanning of large areas (*e.g.* figures 32a, 42, 48, 50, 51, 52, 55, 58, 59).

3.5 Bephore Chips

3.5.1 Fabrication

Silicon wafers (100 mm diameter, 0.525 mm thickness, prime grade; Siegert Wafer, Aachen, Germany) with a 50 nm layer of dry thermal oxide were first cleaned *via* an RCA procedure (water, ammonia solution NH_3(aq) 30% and hydrogen peroxide H_2O_2 30%, at a ratio 5:1:1), followed by thorough rinsing with DI water and drying under a nitrogen stream. The wafer was then covered with a solution of 5 mg/ml heterobifunctional PEG (Biotin-PEG-Silane, MW 5,000, Laysan Bio, AL, USA; chemical structure in figure 65a in the appendix) in toluene, which resulted in the formation of a biocompatible, biotinylated PEG layer on the wafer surface. The wafer was rinsed with isopropanol and water, dried under a nitrogen stream and stored in the dark until use.
Only few hours before lithography, chips of desired size were cut from the wafer and covered for 1 h with the photo- and electron-sensitive mix of DNA and streptavidin (1 μM streptavidin, 1.5 μM PC strands, 7.5 μM PH, in 1×PBS buffer; for details see section 4.2; DNA sequences in the appendix, page 134). The photocleavable DNA was handled only under yellow light. After washing the chip with 1×PBS, the chip was passivated once more with BSA and unlabelled DIS strands (1 mg/ml BSA, 10 μM DIS, in 1×PBS). This step strongly reduced the unspecific attachment of DNA to unpatterned regions.

3.5.2 Electron Beam Patterning

For EBL, Bephore chips with immobilised photo- and electron-sensitive DNA-streptavidin mix had to be dried. Therefore, the chip was first washed with 1×PBS (by pipetting) in order to remove any unbound DNA and streptavidin, followed by thorough rinsing with ethanol using a wash bottle. It was left to dry under a cover, *e.g.* in a closed pipette box, and was then transferred to the ebeam system (eline, Raith). After lithography, a droplet of DIS strands in 1×PBS was placed onto the patterned chip for at least one hour.

3.5.3 Photolithography

Photolithography on Bephore chips was performed using an upright microscope (Olympus BX51, Simmel lab) and a UV light source (EXFO X-Cite 120Q). Thereby, masks could be inserted at the position of the field iris diaphragm and projected onto the chip. In contrast to the ebeam process, UV lithography with a water immersion objective was performed in liquid, *i.e.* without drying the biochips. Especially for Bephore chips, a procedure without drying led to significantly better results regarding the signal-to-noise ratio.

After the UV exposure, DIS strands were added onto the chip for several hours or overnight (depending on their concentration). For the "Tiger" (figure 24), consecutive lithography steps, incubations with DIS strands (10 μM, 3 h) and washing steps were carried out without moving the chip nor the objective.

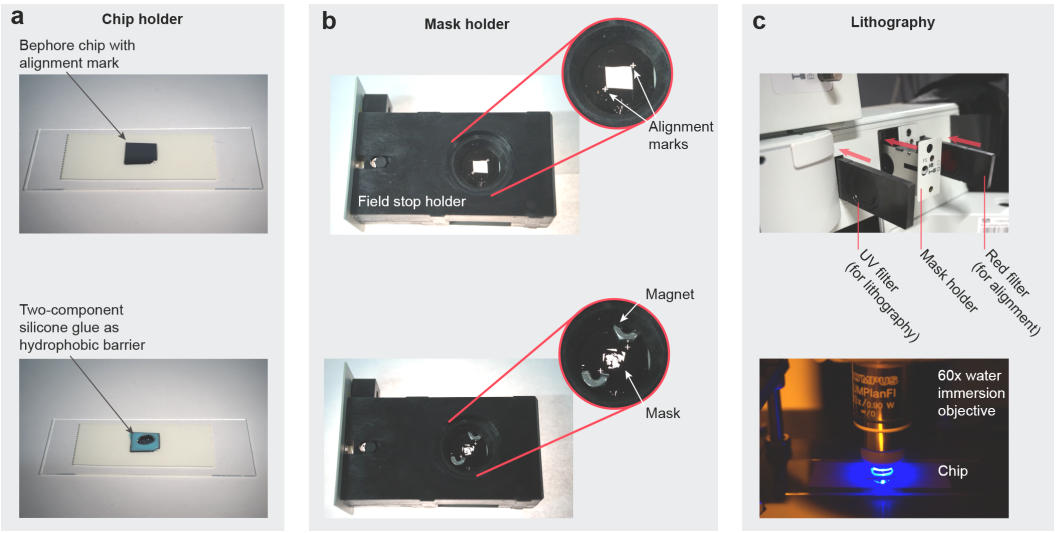

Figure 16: **Mask-projection lithography. a,** A chip is glued to a glass object holder using double-sided adhesive tape. As an alignment mark for lithography we simply created a scratch on the chip using a diamond cutter. Additionally, silicone glue (Picodent Twinsil®) was applied to the edges of the chip in order to prevent droplets from spreading out. This procedure significantly reduced the required amount of DNA and facilitated washing steps. **b,** For masked lithography, *e.g.* the "Tiger" (figure 24), we inserted masks into the field stop holder. For multi-step lithography, marks (crosses) on the holder and on the masks ensured the angular alignment. **c,** The mask holder was then inserted into the light path. A red filter was used to align the projected mask with the alignment marks on the Bephore chip. Eventually, we removed the red filter, slid in the UV filter and exposed the chip.

3.5.4 Compartmentalised Gene Expression

Linear DNA fragments carrying the gene for a fluorescent protein were generated by PCR from plasmid DNA. We used one primer with a fluorescent label, the other primer with an additional DIS-strand sequence. The DIS sequence was separated from the primer by a spacer, which prevented the DNA polymerase in the PCR from extension into the DIS sequence (sequences on page 134 in the appendix). After PCR, the DNA was purified using a kit (Wizard® SV Gel and PCR Clean-Up System, Promega) and diluted to a concentration of ≈ 100 nM in a solution containing 1 M NaCl. The gene was then immobilised close to an alignment mark on a chip following the procedure outlined in the previous section 3.5.3. Thereby, the chip was already placed on a special holder (figure 17b).
Compartments were fabricated in polydimethylsiloxane (PDMS) following standard procedures. Briefly, a master for PDMS moulding was created on silicon wafers (100 mm diameter, 0.525 mm thickness, prime grade; Siegert Wafer, Aachen, Germany) with a ≈30 μm thick layer of negative resist (Epocore20; micro resist technology GmbH, Berlin, Germany) by masked photolithography in a maskaligner (MJB3, Karl Suss). PDMS and curing agent were mixed at a ratio of 10:1 (Sylgard 184 Silicone Elastomer Kit, Dow Corning Corporation) and degassed in a vacuum desiccator. Next, the master was spincoated with PDMS at 100 rpm and transferred to an oven, where the PDMS was baked at 70°C for at least 1 h. Afterwards, the PDMS was separated from the master and cut into smaller pieces containing the compartments. The flat side of such a PDMS chip was then cleaned with isopropanol and by oxygen plasma (42 s, 100 W; Femto, Diener), and bonded to a clean glass slide in an oven (70°C, 1 h). Shortly before an experiment, the PDMS chip on the glass slide was rendered hydrophilic by oxygen plasma (42 s).
The Bephore chip carrying the immobilised genes was then covered with ≈100 μl of transcription/translation mix (PURExpress® [32], New England Biolabs; or *E. Coli* extract [84] with 5 µM GamS protein [85], kindly provided by Ludwig Bauer). Next, the compartments in the PDMS chip were aligned with the alignment mark on the Bephore chip and pressed onto it with gentle force as shown in figure 17. Eventually, the chip holder was transferred to a temperature-controlled microscope for imaging (Nikon Ti2-E inverted microscope; light source: SOLA SM II, Lumencor; camera: Neo5.5, Andor; temperature control: bold line, Okolab).

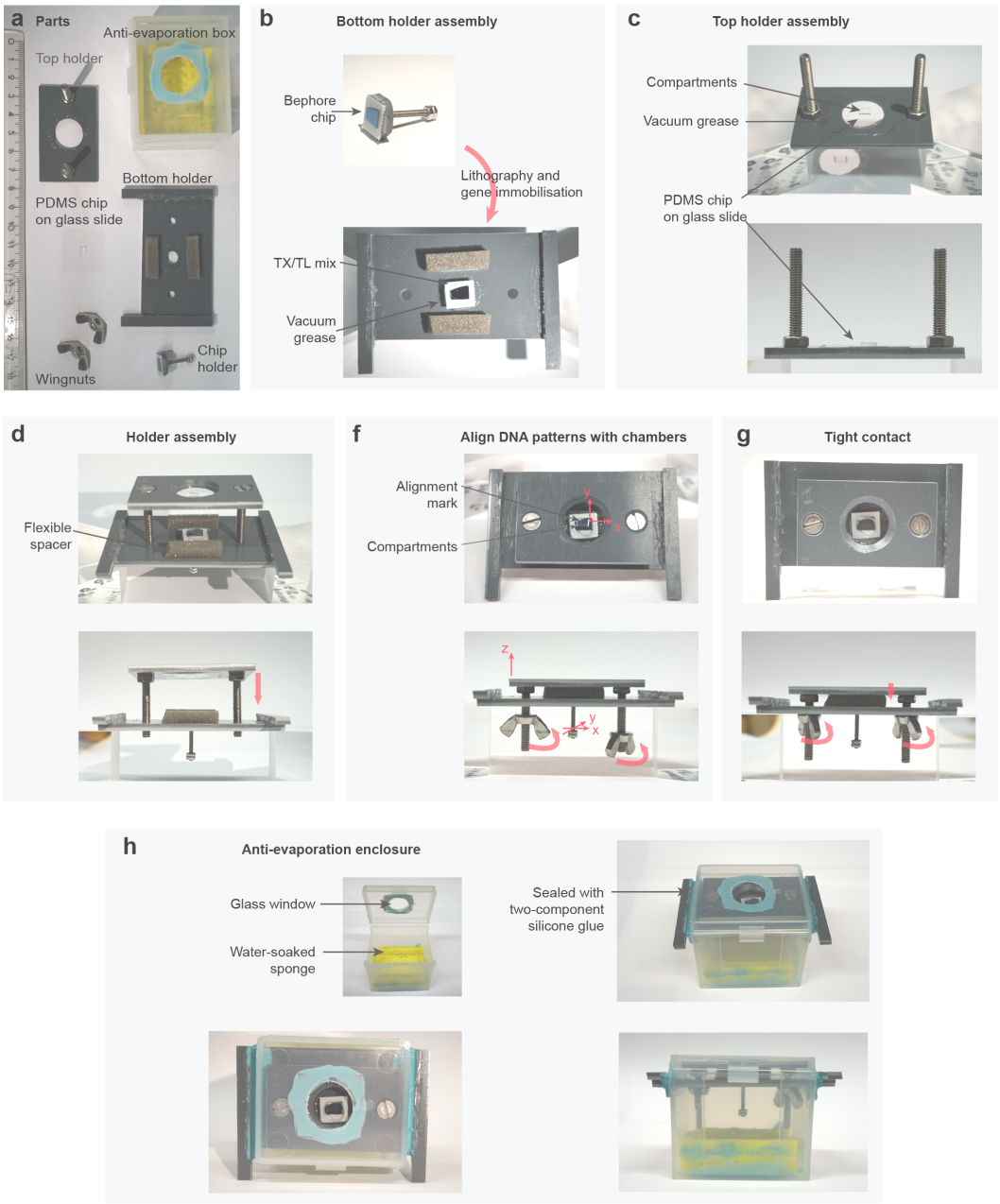

Figure 17: **Sample preparation for compartmentalised gene expression. a,** Parts used in the assembly of the sample holder (ruler unit: cm). **b,** After lithography and DNA brush assembly close to an alignment mark, a Bephore chip is placed onto the bottom part of the holder and covered with a TX/TL mix. Vacuum grease is here used as a weak adhesive between the chip holder and the bottom plate. **c,** The PDMS chip is immobilised on the top part of the holder. **d-g,** Chip and PDMS are brought into close proximity, so the chip can be aligned with the PDMS chambers in the x-y-plane using the handle at the bottom of the holder. Once aligned, the wingnuts are carefully turned to bring chip and PDMS in tight contact. **h,** Finally, the holder is additionally enclosed in a box in order to reduce the evaporation of the TX/TL mix.

4 Biochips: Daisy and Bephore

Biochips served as platforms for most of the experiments performed within this project. Especially the Daisy chips, which were provided by the group of R. H. Bar-Ziv, proved to be a versatile and robust system which we employed in our investigations of DNA condensation on a chip (section 5).
Here, on the one hand we expanded the patterning capabilities of the Daisy system towards higher precision using electron beam lithography (EBL). Other groups have demonstrated various PEG-based EBL patterning strategies, however mainly based on electron-induced crosslinking of surface-bound PEG with a second layer of modified, loose (*e.g.* biotinylated) PEG [86–89]. In contrast to the Daisy patterning discussed in the following, such PEG patterns swell in water and therefore heavily change the topography of the chip surface, making them unsuitable for the characterisation of DNA structures formed by DNA condensation (section 5).
On the other hand we also considered alternatives to Daisy and developed a novel type of resist which we termed "Biocompatible Electron and PHOtosensitive RESist" ("Bephore") and which allowed for multi-step photolithography.

4.1 Daisy Patterning by Electron Beam Lithography

The patterning of the Daisy resist by UV lithography, *i.e.* the specific cleavage of the protecting headgroup at the secondary amine (see section 2.2 for details), is comprehensible at the molecular level considering the ultraviolet excitation of the photolabile NVOC headgroup [31]. Surprisingly, also electron beam writing could strip the headgroup and therefore enable the patterned functionalisation of the biochip surface (figure 18). Even though we did not thoroughly investigate the mechanism of cleavage at the molecular level, secondary electrons (section 3.1) are candidates for providing the required energy [90]. Compared to the energy of ultraviolet photons (3.4 eV at $\lambda = 365$ nm), secondary electrons (by definition 2-50 eV) have similar kinetic energies with their mean below 10 eV and a full width at half maximum also < 10 eV. These secondary electrons are also responsible for the local chemical modification in many other EBL resists, *e.g.* PMMA [73].
In order to characterise electron beam writing on Daisy, we carried out dose tests for various acceleration voltages. For each voltage a matrix of squares was written, each square with a distinct electron dose (charge per area). The patterns were

then functionalised with biotin and visualised *via* fluorescently labelled streptavidin. Two exemplary dose tests for acceleration voltages of 5 kV and 30 kV are shown in figure 19a. The fluorescence data is quantified in figure 19c, including data sets for additional acceleration voltages (fluorescence images of all dose tests are shown in figure 64 in the appendix).

Apparently, at low doses the density of binding sites on the surface increases with the dose. After reaching a peak value, the fluorescence intensity again drops until a final level above the background intensity. This final level of intensity at high doses is reached even without biotinylation and therefore hints at non-specific adsorption of streptavidin in regions, where the Daisy resist was destroyed.

Further evidence for the destruction of the resist at high doses is shown in figure 20. Several stripes were written with different electron doses and then scanned by AFM. The topography indicates that molecules in the exposed regions were cleaved and removed from the surface. While the effect is barely visible for low doses, at

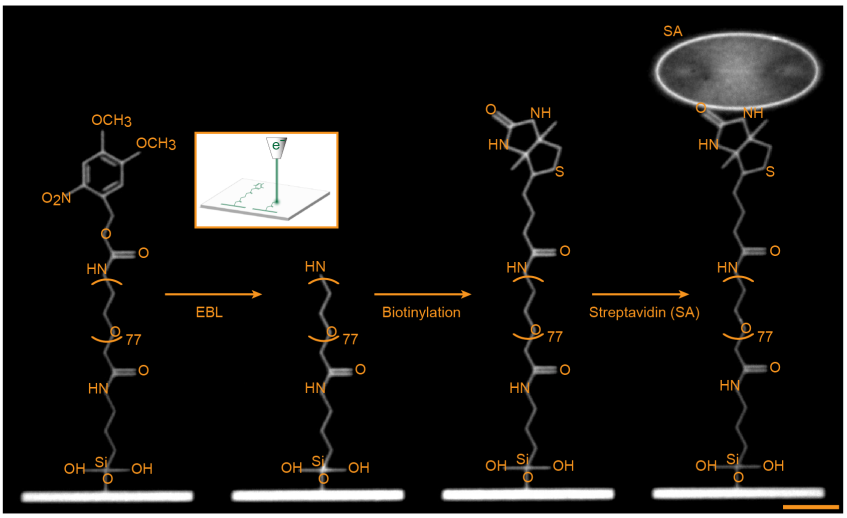

Figure 18: **Electron beam lithography (EBL) on Daisy substrates.** Daisy molecules are immobilised on a surface, forming a photo- and ebeam-cleavable monolayer. By exposure to UV light or an electron beam, the protective headgroup is cleaved, revealing a primary amine for functionalisation with biotin. Streptavidin (SA, here represented by an elliptic shape) can bind up to four biotin molecules and can therefore be used to attach additional biotinylated molecules, *e.g.* biotinylated DNA. The chemical structure shown in this image was written by EBL and visualised *via* fluorescently labelled streptavidin in fluorescence microscopy. The illustration of EBL (inset) and orange labels were added afterwards. Scale bar (orange): 10 μm.

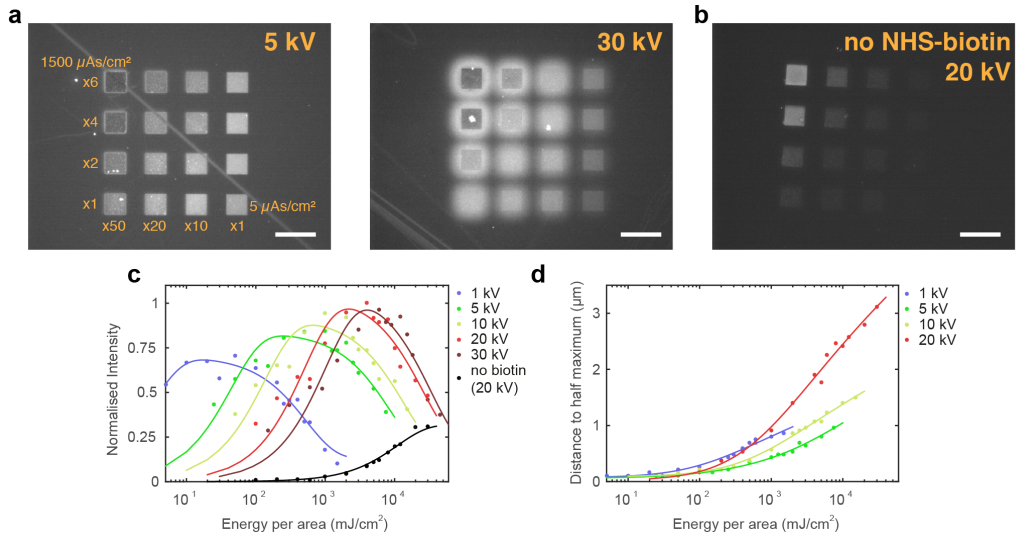

Figure 19: **Electron beam lithography dose tests. a,** Fluorescence images of two exemplary matrices of squares, each square written at a different electron dose (charge per area), after functionalisation with biotin and fluorescently labelled streptavidin. The left matrix was written at an acceleration voltage of 5 kV, the right one at 30 kV. Apparently the proximity effect is much more pronounced at the higher acceleration voltage. **b,** Dose test written at 20 kV after the addition of streptavidin, but without a preceding biotinylation. The adsorption of streptavidin to areas exposed to high electron doses hints at the destruction of the PEG layer and therefore at the loss of surface passivation. **c,** Quantification of the fluorescence intensities from dose tests written at various acceleration voltages. Fluorescence intensities were first converted to signal to noise ratios (SNR) for each dose test individually and then normalised to the maximum SNR measured in all of the dose tests for comparison among them. The energy per area (x-axis) is calculated by dose $\times$ acceleration voltage. The solid lines represent a fitted model which accounts for a specific cleavage of the Daisy headgroup and a non-specific degradation of the resist molecules (page 56). **d,** Proximity effect for various acceleration voltages characterised by the distance of half the maximum fluorescence intensity from the edge of a square. Scale bars: 20 μm.

very high exposures the monolayer of a thickness of $\approx 1.5 - 2$ nm was completely removed (figure 20b).

Put together, the experiments suggest that the fluorescence intensities observed in figure 19a are the product of two processes: 1) the specific cleavage of the Daisy headgroup, enabling the functionalisation with biotin and streptavidin; 2) the degradation of the Daisy molecule, *i.e.* the cleavage of molecular bonds between amine and substrate, reducing the density of potential binding sites and allowing for non-specific adsorption of streptavidin to the bare substrate. In order to check the plausibility of this hypothesis, we created a simple model for the Daisy patterning and examined whether it can fit the fluorescence data from the dose tests. The model is based on the assumption that the intact molecules decay under electron exposure with first order kinetics at rates k_1 (specific cleavage of the headgroup) and k_2 (cleavage of any other bond along the Daisy backbone). Accounting for only three species, *i.e.* the native Daisy molecules with surface density N, the deprotected molecules A displaying primary amines, and the species of degraded molecules D, we set up a system of first order reactions. In contrast to common

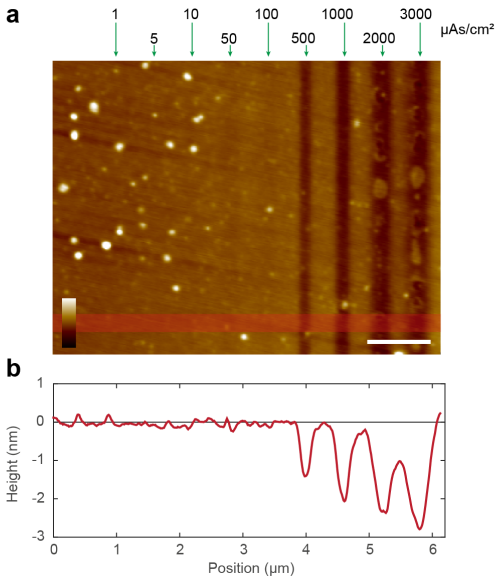

Figure 20: **Degradation of the Daisy layer by EBL. a,** AFM scan in air of a Daisy surface after the patterning of several 200 nm wide stripes at various doses (indicated at the top) and after washing the surface with water in order to remove possible debris. Both the image and **b,** a section along the image indicate that at high doses the resist of a thickness of typically $\approx 1.5 - 2$ nm was damaged and removed. Scale bar: 1 μm, height bar: 10 nm.

time-dependent kinetics, the surface densities $N(\sigma)$, $A(\sigma)$, $D(\sigma)$ are functions of the electron dose σ.

$$N \xrightarrow{k_1} A$$
$$N \xrightarrow{k_2} D$$
$$A \xrightarrow{k_2} D$$

These reaction equations yield a system of linear differential equations:

$$\begin{aligned} \frac{dN}{d\sigma} &= -(k_1 + k_2) \cdot N \\ \frac{dA}{d\sigma} &= k_1 \cdot N - k_2 \cdot A \\ \frac{dD}{d\sigma} &= k_2 \cdot (N + A) \end{aligned}$$

with boundary conditions:

$$\begin{aligned} N(\sigma = 0) &= 1 \\ A(\sigma = 0) &= 0 \\ D(\sigma = 0) &= 0 \end{aligned}$$

and the analytical solution:

$$\begin{aligned} N(\sigma) &= e^{-(k_1+k_2)\sigma} \\ A(\sigma) &= e^{-k_2\sigma} - e^{-(k_1+k_2)\sigma} \\ D(\sigma) &= 1 - e^{-k_2\sigma} \end{aligned}$$

The solution was then used to fit the fluorescence Signal-to-Noise Ratio (SNR) graphs in figure 19c for each acceleration voltage individually. Part of the signal thereby results from fluorescent streptavidin specifically bound to biotinylated amines (hence $\propto A$), another part from non-specific adsorption to degraded areas ($\propto D$).

$$SNR(\sigma) = \alpha \cdot A + \beta \cdot D + 1$$

Here, α and β are proportionality factors, the addition of $+1$ results from the calculation of the SNR. Since β is determined by the SNR at high doses, only the three parameters α, k_1 and k_2 were used to fit the experimental data. While the

parameter α mainly influences the amplitude of the peak, the two rate constants k_1 (specific cleavage yielding an amine) and k_2 (disintegration of the Daisy molecule) can hint at the specificity of the headgroup cleavage. The ratio k_1/k_2 depends on the acceleration voltage and drops from > 150 at 1 kV and 5 kV to ≈ 30 at 30 kV. Considering the number of possible bonds to be broken along the $(PEG)_{77}$ chain, such high specificities for cleaving exactly the bond at the amine are also required in order to achieve detectable surface patterning.
In spite of several simplifications and weaknesses of the model - for instance it ignores the possibility of electron-induced cross-linking of the PEG - it qualitatively agrees with the experimental data and therefore strengthens our basic hypothesis on the patterning mechanism.
We further analysed the dose tests in figure 19a to characterise the impact of the acceleration voltage on the proximity effect (see also section 3.1). While the first matrix in figure 19a was written at 5 kV and displayed sharp edges, the array written at 30kV appeared blurry with indistinguishable edges. In figure 19d the effect is characterised for several acceleration voltages by displaying the distance from the edge of a square to half of the maximum fluorescence intensity. As a compromise in the requirements of high SNR and weak proximity effect, an acceleration voltage of 5 kV and doses of $5 - 30$ μAs/cm^2 were utilised in the experiments shown in the following sections 5 & 6.

4.1.1 Daisy Patterning for DNA Immobilisation

The lithographic approach was mainly intended for the patterned immobilisation of DNA and not of streptavidin alone. Therefore, we performed another dose test for the 3.1 kbp DNA-streptavidin compound which we later used in our DNA condensation experiments. Figure 21a displays a matrix of squares patterned at an acceleration voltage of 5 kV, revealing that despite the size of the compound, the doses established for streptavidin alone ($5 - 30$ μAs/cm^2) also worked well for the patterning of DNA. In later experiments, we thereby preferred low over high doses even at the expense of a non-maximum DNA density in order to avoid degradation of the Daisy coating.
Furthermore, we compared DNA patterning by EBL and UV light (figure 21b). A quantification of fluorescence intensities from labelled DNA in both UV and ebeam (5 kV) dose tests is shown in figure 21c. The maximum intensities achieved *via*

ebeam lithography were ≈25% lower than with UV, which can be attributed to the degradation of the resist by the highly reactive electrons. While the cleavage of the headgroup by UV is more specific compared to ebeam lithography, very high UV doses eventually also degrade the resist (not shown in the graph). The requirement of more energy for the UV lithography appears reasonable considering the amount of light reflected by the silicon surface without any interaction with the resist.

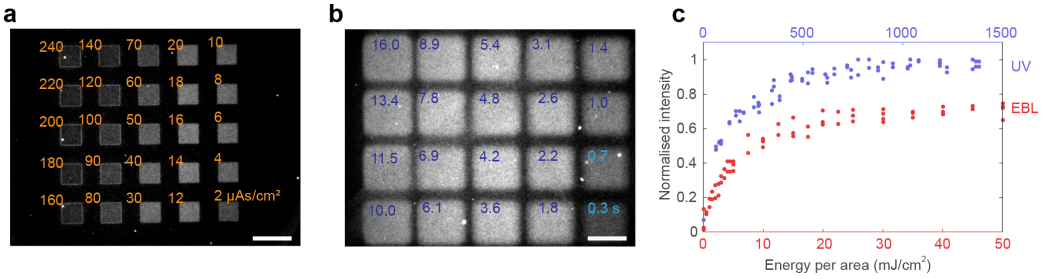

Figure 21: **Dose test for DNA patterning by ebeam and UV lithography. a,** EBL dose test written at 5 kV and subsequently functionalised with biotin and a DNA-streptavidin complex (fluorescently labelled 3.1 kbp DNA). **b,** Matrix of squares exposed to UV light for different periods of time (blue numbers) at a power density of 167 mW/cm^2. **c,** Quantification of fluorescence intensities of several dose tests like **a**&**b** for both ebeam and UV lithography (separate x-axes). All values were normalised to the overall maximum intensity. Scale bars: 20 μm.

4.2 Biocompatible Electron- and Photosensitive Resist: Bephore

While Daisy indeed represents a useful tool for the patterned immobilisation of biomolecules, its capabilities are limited especially with respect to multi-step lithography, since the reactive NHS-biotin must be added after each step in high concentration. Furthermore, Daisy is not commercially available and is not easily synthesised without proper equipment and training. We therefore also investigated an alternative to the Daisy system.
Here, we used DNA with a photocleavable, internal modification (based on a nitrophenyl moiety [91]; chemical structure in figure 65b in the appendix) as an integral part of the resist. At UV exposure, this modification of the DNA backbone breaks, thereby cutting single-stranded DNA in two pieces. Huang *et al.* already demonstrated negative-tone photolithography on gold surfaces, with fluorescent DNA hybridising only to non-illuminated, surface-bound photocleavable DNA [92]. Two major disadvantages of this system are the UV cleavage efficiency, which reaches only ≈90% even at long exposures and therefore results in a rather strong background fluorescence, and the non-biocompatible gold surface. Also Chirieleison *et al.* applied photocleavable DNA modifications to create patterns in a gel matrix by masked UV illumination [93].
In contrast to their work, we here specifically aimed at creating a positive-tone resist on a PEG-based, biocompatible substrate.

4.2.1 Design

The working principle of the DNA component of our resist is illustrated in figure 22a. The goal was to allow hybridisation of a photocleavable strand ("PC strand") with another strand ("DIS strand") only upon UV illumination. The core element of the system is the PC hairpin, which consists of a "stem" region, the photocleavable modification, a "loop", and a short region which is complementary to a toehold sequence on the stem. The photocleavable modification is placed at the beginning of the loop in order to avoid the distortion of double stranded DNA regions. The PC strand further carries a biotin for immobilising the strand on a surface.
In its initial state, the stem region is hybridised to another strand, the "placeholder" ("PH strand"). PH and the hairpin configuration of iPC ensure that the stem is protected from toehold mediated strand displacement. Even though the double-

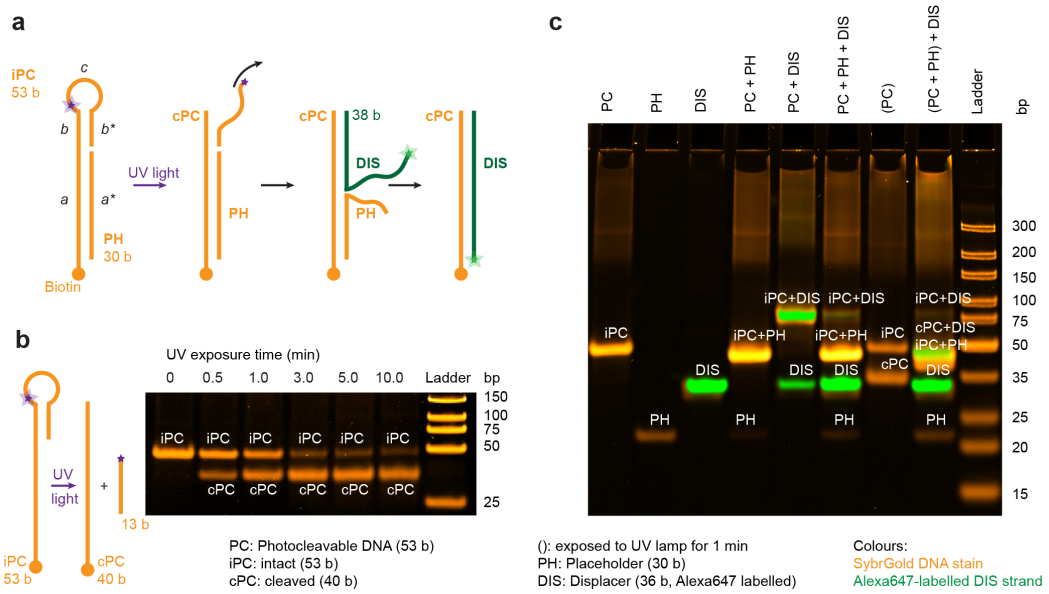

Figure 22: **Bephore: concept and characterisation in bulk. a,** Concept of Bephore patterning. Initially, the system is formed by two DNA strands: 1) the intact photocleavable hairpin (iPC, sequence domains $abcb^*$) consisting of a 40 nt long stem region (ab), a 5 nt loop (c) and an 8 nt self-complementary region (b^*), and 2) a 30 b long strand ("placeholder", PH, sequence domain (a^*) which prevents hybridisation of other strands to the stem, as long as the hairpin is intact. UV light cleaves the PC strand, causing the dissociation of the shorter fragment (cb^*) and leaving only the stem (cPC, ab) attached to the surface. Now, another strand (DIS, b^*a^*) can displace the PH strand *via* toehold mediated strand displacement and stably hybridise to the stem (for the DNA sequences see page 134 in the appendix). **b,** In order to verify the cleavage, PC strands were illuminated with a UV handlamp (6 W electrical power, wavelengths: 254 nm, 365 nm) and analysed by gel electrophoresis. **c,** Combinations of strands show that hybridisation of strands occurs as designed (lanes: PC+PH, PC+DIS), and that strand displacement by DIS is blocked for pre-mixed PC and PH (lane: PC+PH+DIS), unless PC and PH are exposed to UV (lane: (PC+PH)+DIS). Gels: 15% native PAGE, TAE buffer, 100 V, b: 2.5 h, c: 3 h.

stranded toehold region of 8 bp is thermodynamically unstable, the hybridised state is highly favoured, since the sequences are linked *via* the loop and therefore present at very high local concentrations. UV illumination removes the link (figure 22b), releasing the shorter fragment of PC to solution, and leaving the toehold region of the stem single stranded. Next, a "displacer strand" (DIS) is added, potentially carrying *e.g.* additional chemical modifications or a gene. The DIS strand hybridises with the stem by toehold mediated displacement of the PH strand. We verified by gel electrophoresis that the system actually worked as intended (figure 22c) and then moved on to immobilise it on a chip.

4.2.2 Single- and Multi-Step Photolithography

In order to obtain a chip which provides biocompatibility and the possibility to immobilise the photocleavable DNA, we coated our silicon/silicon dioxide chips with a layer of heterobifunctional PEG (5,000 Da, chemical structure in figure 65a in the appendix). On one side the PEG carried a silane for the attachment to the SiO_2 surface, on the other side a biotin. Next, we mixed streptavidin with the biotinylated PC strand and the PH strand at a ratio of 1:1.5:7.5. A lower ratio than 1:1.5 of streptavidin to PC strand can result in a low surface density of PC DNA, while a higher ratio can saturate the streptavidin molecules with biotin and therefore prevent their attachment to the surface. The PH strand was simply added in large excess to ensure hybridisation with the PC strand. After washing, we illuminated the surface through the objective of a microscope with a UV filter in the beam path and an almost entirely closed field iris diaphragm, and then added a fluorescently labelled DIS strand (figure 23a). Fluorescence images (inset in figure 23b) for several exposure times were used as a UV dose test (figure 23b). Furthermore, we repeated the lithography step and incubated the chip each time with a differently labelled DIS strand. Depending on the UV exposure times, exposed regions were filled either exclusively by a single type (red, green or blue) of DIS strand (figure 23c) or by combinations of them (figure 23d). The overlay of the fluorescence images using the RGB colour model then yielded an image with primary and secondary RGB colours, black and white.

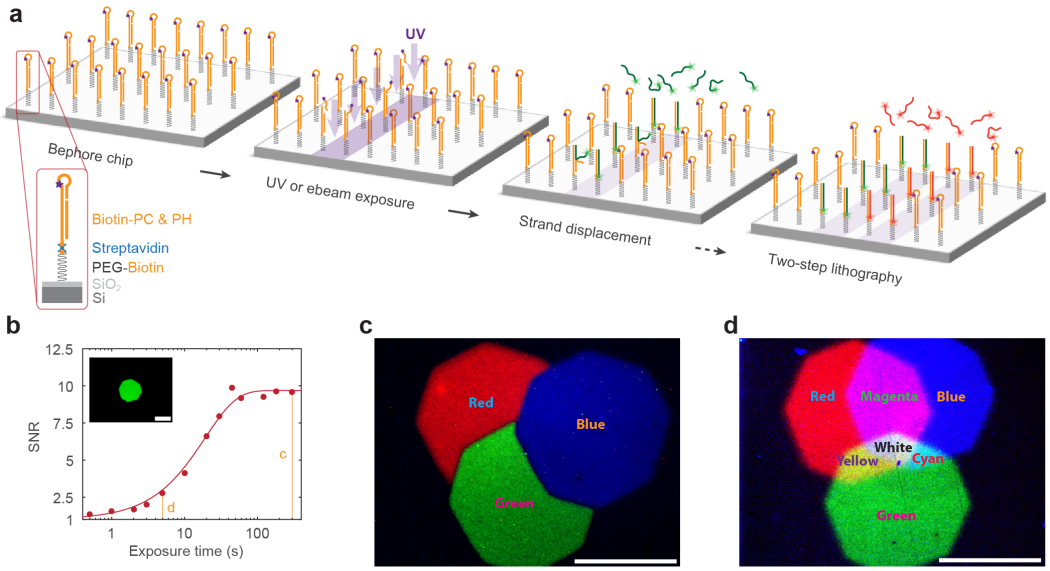

Figure 23: **Photolithography on a Bephore chip.** **a,** Illustration of the patterning process. A silicon dioxide surface is first coated with biotinylated PEG and then incubated with pre-mixed streptavidin and photosensitive DNA. Next, masked photolithography is performed and DIS strands (green) are added onto the chip, so they can bind to the UV-exposed areas. If necessary, the lithography step can be repeated in order to attach a different type of DIS strand (red) to another region on the chip. **b,** Quantification of fluorescence signal to noise ratio (SNR) from ATTO 532 labelled DIS strands bound to patterned regions. The vertical lines indicate the exposure times used in images c&d. The solid line represents the same fitted model as for EBL on Daisy (page 56), but without degradation. Inset: fluorescence image of DIS strands bound to an area previously illuminated with UV light through the field iris diaphragm of a microscope (120 s exposure, 60× water immersion objective). **c,** Overlay of fluorescence images after a three-step lithography (120 s UV exposures) with DIS strands labelled with ATTO 425 (blue), ATTO 532 (green) and Alexa Fluor 647 (red). The coloured regions do not overlap, because the long exposure times activated all binding sites and left none for subsequent lithography steps (blue first, then green and eventually red). **d,** In contrast, short exposure times of only 5 s allowed for the attachment of different DIS strands in the same region. Applying the RGB colour model to the overlay of the fluorescence images, overlapping regions appear in additional colours (yellow, cyan, magenta) and in white. Scale bars: b-d, 50 μm.

We further explored the capabilities of our multi-step lithography technique by reproducing a famous painting - the "Tiger" by Franz Marc[1] - in a miniaturised fluorescent replica. Figure 24 shows the original picture, the design of the photolithography masks and the final RGB fluorescence image. The image not only demonstrates our ability to create regions filled with different types of DNA strands, but also their precise alignment on the micrometer scale.

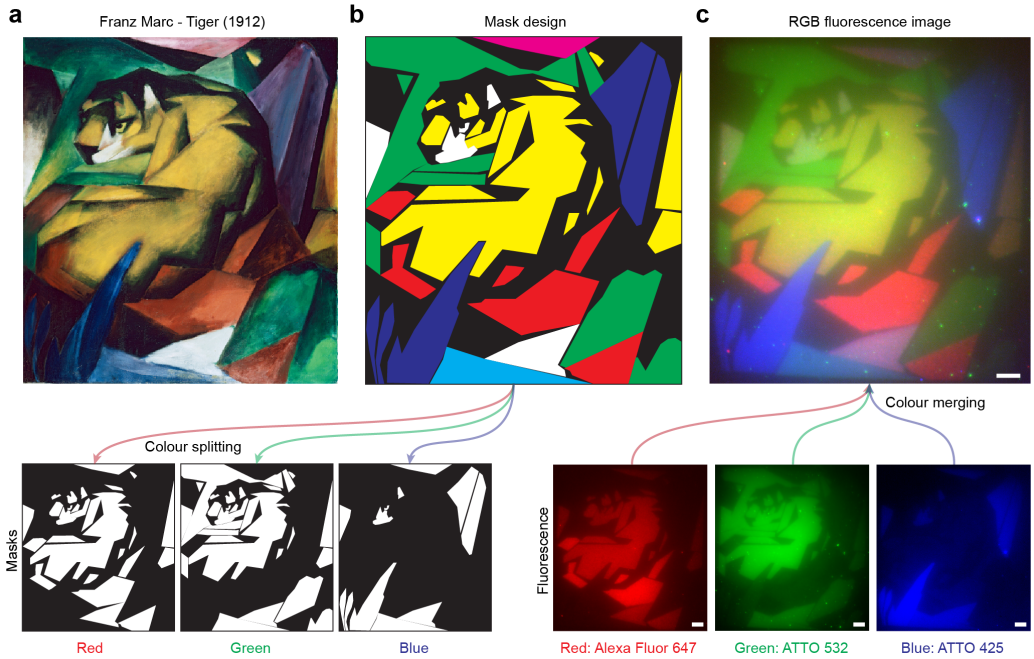

Figure 24: **RGB lithography - The Tiger.** **a,** Oil painting "Tiger" (1912, size: 109×99 cm^2) by the artist Franz Marc. **b,** In order to reproduce the "Tiger" using our RGB three-step lithography, we first simplified the picture and reduced the colours to primary and secondary colours, black and white. From the resulting image we obtained three masks (bottom left), one for each lithography step. **c,** Placed at the position of the field iris diaphragm, the UV projection of the masks onto a Bephore chip defined the areas for red, green and blue DIS strands (bottom right). Merging the three fluorescence images yielded an RGB fluorescence image of the "Tiger" (top). With a side length of ≈ 250 μm, this DNA-based replica represents a $4,000\times$ miniaturisation of the original painting. Scale bars: c, 20 μm.

[1]Born in Munich in 1880, Franz Marc became a member of an expressionistic art movement called "Der Blaue Reiter". The painting "Tiger" (figure 24a) displays mainly primary and secondary RGB colours and clearly shows a cubistic influence, especially in its well-defined edges. These elements made it an excellent template for a demonstration of our multi-step lithography technique. The painting is part of the collection of the Lenbachhaus art gallery in Munich. Franz Marc died in 1916 in World War I.

4.2.3 Electron Beam Patterning of a Bephore Chip

After the successful demonstration of ebeam patterning on Daisy, we also investigated potential EBL capabilities of Bephore. The photocleavable chemical groups in Bephore and Daisy are very similar and an EBL dose test indeed revealed that similar electron doses enable the patterning of both types of resist. Also here, the maximum fluorescence intensities achieved *via* EBL were $\approx 30\%$ lower than *via* photolithography. The results from an area dose (electrons per area) test in figure 25 are well described by the simple model we applied to fit the Daisy dose test (page 56). In contrast to Daisy however, already much lower electron doses considerably decreased the binding of DIS strands, probably since the DNA strands and the longer PEG chain (MW 5,000) of Bephore are more susceptible to electron-induced molecular damage than the smaller Daisy molecule (MW 3,400). The stronger rate of degradation (k_2) explains the lower specificity ($k_1/k_2 \approx 10$) of Bephore patterning by EBL compared to Daisy ($k_1/k_2 \approx 100$).

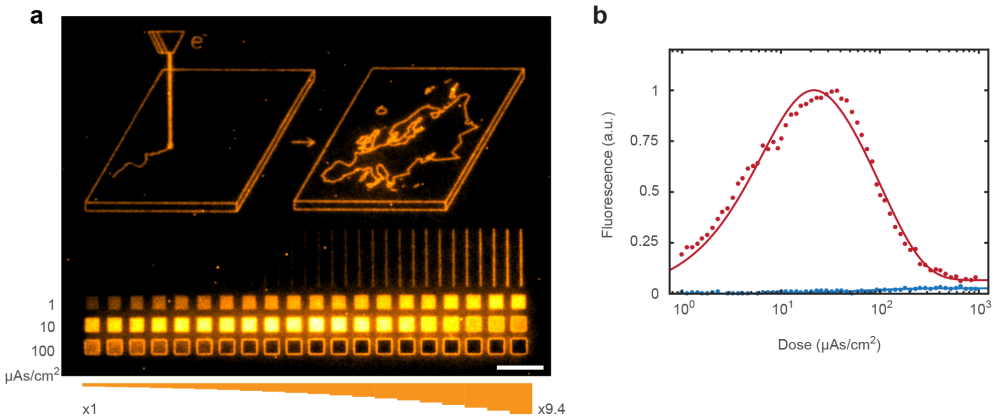

Figure 25: **Electron beam lithography on a Bephore chip. a,** Fluorescence image of an ebeam-patterned chip after incubation with DIS strands (ATTO 532 labelled). Top: illustration of an electron beam writing an arbitrary pattern (map of geographical Europe) onto a chip surface. Bottom: line (see also figure 26) and area dose tests. Numbers on the left give the dose used to write the first square in a row, the bars at the bottom indicate the dose factors along a row. **b,** Quantification of fluorescence intensities from area dose tests on a Bephore chip (red) and a similar chip without the photocleavable DNA (blue). Solid lines represent a fitted model which we also used to fit the Daisy dose tests (page 56). Scale bar: 10 μm.

Additionally, on Bephore we performed a dose test for single pixel lines (electrons per length, figure 26). In contrast to the area dose test, here the fluorescence intensity steadily increased even at high doses. We hypothesise that this observation is mainly owed to the proximity effect and the limited resolution in optical microscopy (for details see figure 26c).

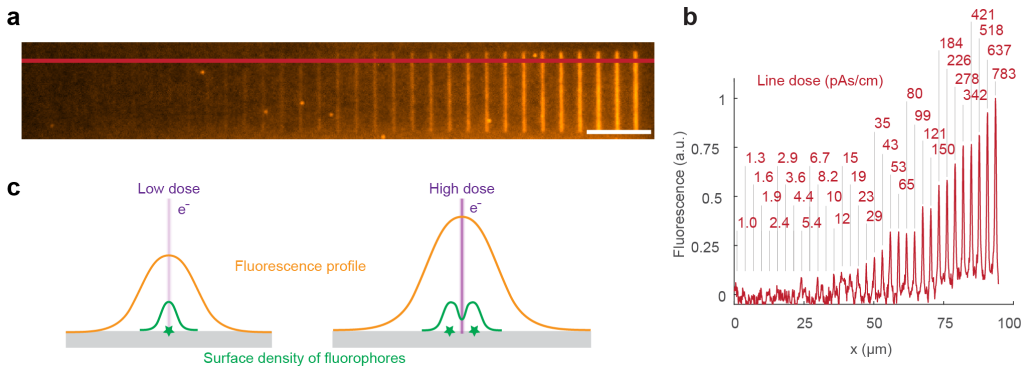

Figure 26: **Single pixel line dose test.** **a,** Fluorescence image of a line dose test. **b,** Fluorescence intensities along the red line in **a**. Red numbers indicate the doses used to write the corresponding lines. **c,** While the area dose test in figure 25 clearly indicates degradation at high doses, here fluorescence intensities continue to increase even at high doses. We assume that the high electron doses degrade Bephore molecules along the beam path, but that at the same time areas to both sides of the path are activated due to the proximity effect, similar to the contours of the degraded squares in figure 25. In fluorescence microscopy, the two resulting bright lines however cannot be distinguished because of the optical resolution limit (for the microscopy setup used here: $\approx$ 400 nm, Rayleigh criterion [74]). Scale bar: 10 μm.

4.2.4 Gene Expression

Finally, we also demonstrated the biocompatibility of Bephore, *i.e.* gene expression from an immobilised DNA brush. Therefore, we first amplified a 1.4 kbp DNA fragment coding for a fluorescent protein (YPet) by PCR with modified primers (figure 27) and then attached it to a lithographically patterned, triangular region on a chip, as illustrated in figure 28a. Next, a droplet of a transcription/translation mix was placed onto the chip which immediately afterwards was covered with chambers fabricated in polydimethylsiloxane (PDMS). Thereby, one chamber enclosed the triangular DNA pattern and developed a strong fluorescence signal from protein expression (figure 28b-d). Unfortunately, unspecific binding of the DNA to the surface could not be entirely prevented. Therefore, low-level gene expression was also observed in control chambers without DNA pattern. Repeated protein expression from the same DNA brush proved that the DNA was not removed from the chip.

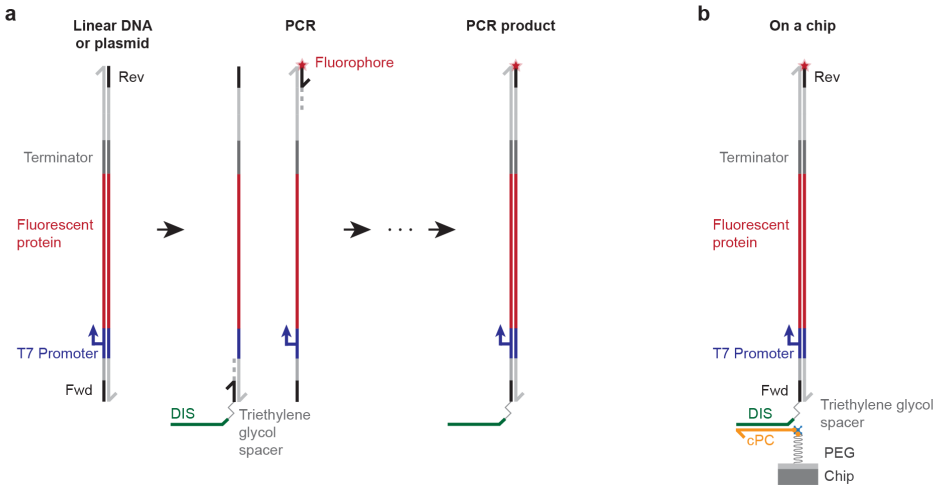

Figure 27: **Immobilisation of a gene on Bephore. a,** Amplification of a DNA sequence coding for a fluorescent protein by PCR. One primer (Rev) was labelled with a fluorophore. The second primer (Fwd) was modified with a triethylene glycol spacer which blocked DNA polymerases during PCR, and a DIS sequence to allow for the attachment of the gene to a cleaved PC strand on a chip surface (**b**). The DNA sequences are shown in the appendix on page 134.

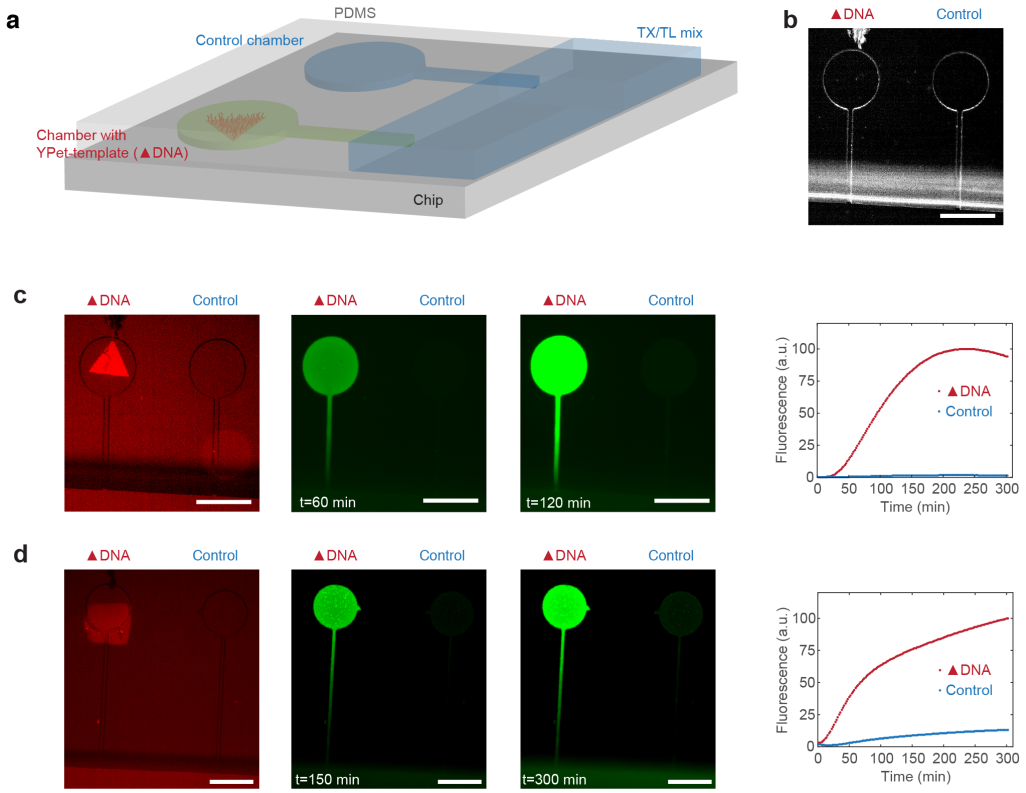

Figure 28: **Gene expression on Bephore. a,** Illustration of a Bephore chip with PDMS chambers (300 μm in diameter) and a transcription/translation (TX/TL) mix. One chamber contains a triangular region with immobilised DNA coding for the fluorescent protein "YPet", while the other chamber acts as a control. Channels (20 μm in width) connect the chambers to a large reservoir of TX/TL mix in order to allow for a sustained expression of YPet. **b,** Brightfield image of two such chambers, where the left chamber contains the triangular DNA field. **c,** The fluorescently labelled (Alexa Fluor 647), triangular DNA field is located in the left chamber (red-coloured image). Both chambers were filled with a reconstituted TX/TL mix (PURExpress®), but only the left chamber shows a strong increase in YPet fluorescence (green-coloured images and graph). After $\approx$ 240 min at 37°C, the PURE system typically stops producing proteins. **d,** A similar experiment demonstrated that gene brushes are also expressed in *E. Coli* extract [84] at 29°C, if the linear DNA is protected from degradation by the protein GamS. Here, the stronger fluorescence in the control chamber is probably a result of a less thorough passivation (compared to **c**: without BSA, see also section 3.5.1) and the development of autofluorescence in the extract over time. Scale bars: b-d, 300 μm.

To demonstrate the potential of the system towards the realisation of genetic circuits on a chip, we applied our multi-step lithography approach to immobilise genes coding for three different fluorescent proteins in separate compartments on a chip (figure 29a, DNA sequences on page 135). Figure 29b shows gradients of the expressed, freely diffusing proteins in the channels between the compartments.
In summary, Bephore allows for photo- and ebeam-patterning of DNA molecules and can be assembled entirely from commercially available materials. Furthermore, we demonstrated its biocompatibility *via* the expression of immobilised genes. It therefore represents an option for future, chip-based investigations of gene expression systems or processes like DNA condensation.

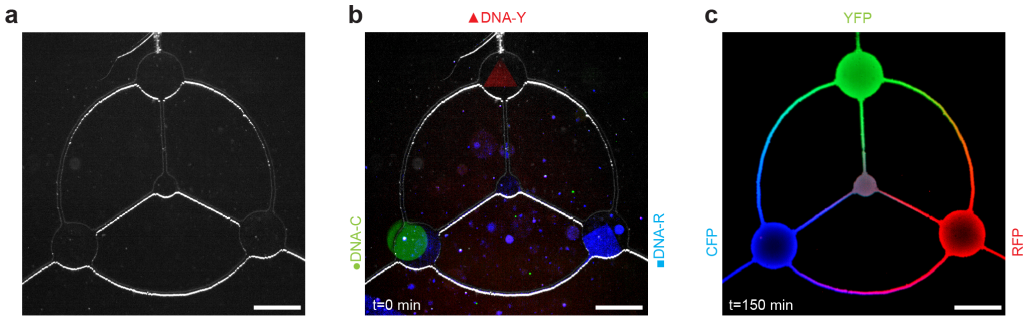

Figure 29: **Multi-colour gene expression. a,** Brightfield image of three chambers connected by channels, in which **b,** DNA brushes coding for cyan (DNA-C, ATTO 532), yellow (DNA-Y, Alexa Fluor 647) and red (DNA-R, ATTO 425) fluorescent proteins were immobilised. The figure shows a coloured overlay of the brightfield image and the fluorescence images of the DNA brushes at the beginning of gene expression (t=0 min). **c,** Overlay image of cyan (mTurquoise), yellow (YPet) and red (mScarlet I) fluorescent proteins after 150 min of expression. Scale bars: 300 μm.

5 DNA Condensation on a Biochip

So far, DNA condensates were limited to few morphologies, namely to spheres, rods or toroids condensed from solution, or to dendritic structures formed by condensation of extended DNA brushes on surfaces (see also sections 2.3.2 & 2.3.3). In the high resolution of ebeam lithography we found the means to create condensates of *arbitrary* shape on a surface by forcing the condensation to proceed along thin lines (figure 30) without the uncontrolled splitting of dendritic bundles. The characterisation of DNA bundle morphology and condensation dynamics will be discussed in the following sections based on results from fluorescence, electron and force microscopy.

5.1 One-Dimensional DNA Condensates

Dimensionality defines the properties of various physical systems. For instance, a defect in a linear (1D) chain always disrupts the whole chain, while (2D) chain mail can still hold, even if a single ring is missing. Examples from physics include nanowires, often also called 1D wires, whose discrete conductance values are defined by the quantum confinement of electrons [94]. Also the predictions of the Ising model for phase transitions in ferromagnetic materials depend on the dimensionality of a system of spins [95].

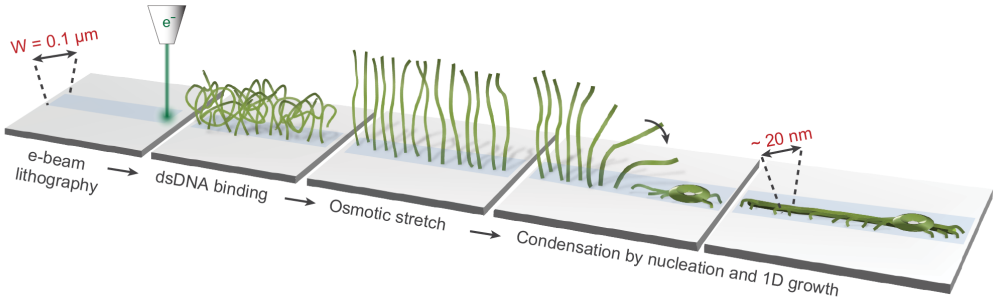

Figure 30: **One-dimensional DNA condensation.** Electron beam lithography allows for the generation of very fine patterns (here: lines of width $W = 100$ nm), along which DNA strands can be immobilised at high salt concentrations. The DNA is then stretched by a change to a low salt concentration ("osmotic stretch") and condensed by the addition of spermidine^{3+}. Condensation starts at a nucleation site and proceeds similar to a domino effect, as additional DNA strands join the DNA bundle (≈ 20 nm in width) at the condensation front.

Here, we investigated the effect of confining the size of a DNA brush with length l and width w from an extended 2D brush to a quasi-1D line with $l \gg w$ and especially to a width much smaller than the contour length of the DNA used in our experiments ($\approx$1 μm for 3.1 kbp). Since the required resolution of $\approx$100 nm cannot be achieved by (conventional) photolithography, we applied the EBL patterning approach demonstrated in section 4.1. We created DNA brushes of various widths and added spermidine at a critical concentration to initiate condensation (figure 31). After few minutes nucleation sites emerged, from which condensates grew. After the completion of the process, the chips were dried and imaged in SEM (figure 32). In wide brushes ($\gtrapprox$ 2 μm) we observed dendritic bundles which split in order to collect all of the available DNA. At brush widths below twice the contour length of the DNA ($\lessapprox$ 2 μm), all DNA strands could, in principle, reach one central condensate. For intermediate widths (*e.g.* 1.5 and 1.0 μm) the main bundle meanders within the boundaries of the brush pattern, presumably due to the stochasticity of growth speed and direction. It occasionally splits into two equivalent bundles, before one of them again establishes itself as the main bundle by gathering all the DNA in a cross section of the brush. At even smaller widths ($\lessapprox$ 1 μm) a single bundle easily attracts all the surrounding DNA, therefore forming a single main bundle without

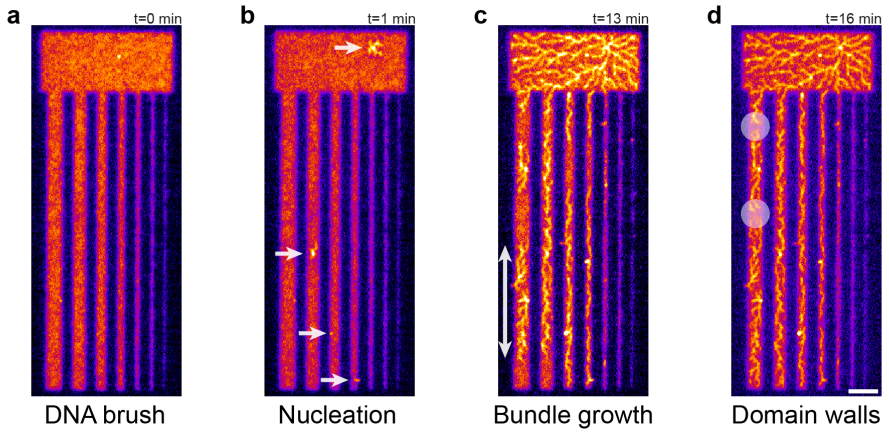

Figure 31: **Condensation of DNA brush stripes. a,** Fluorescence image of a DNA brush patterned *via* ebeam lithography. **b,** Upon addition of spermidine, nucleation sites appeared (bright spots highlighted by white arrows). **c,** DNA bundles grew along the brush stripes away from the nucleation site until **d,** they encountered another condensation domain or the edge of the brush. Two domain walls (see also section 5.4) are highlighted by white circles. Scale bar: 5 μm.

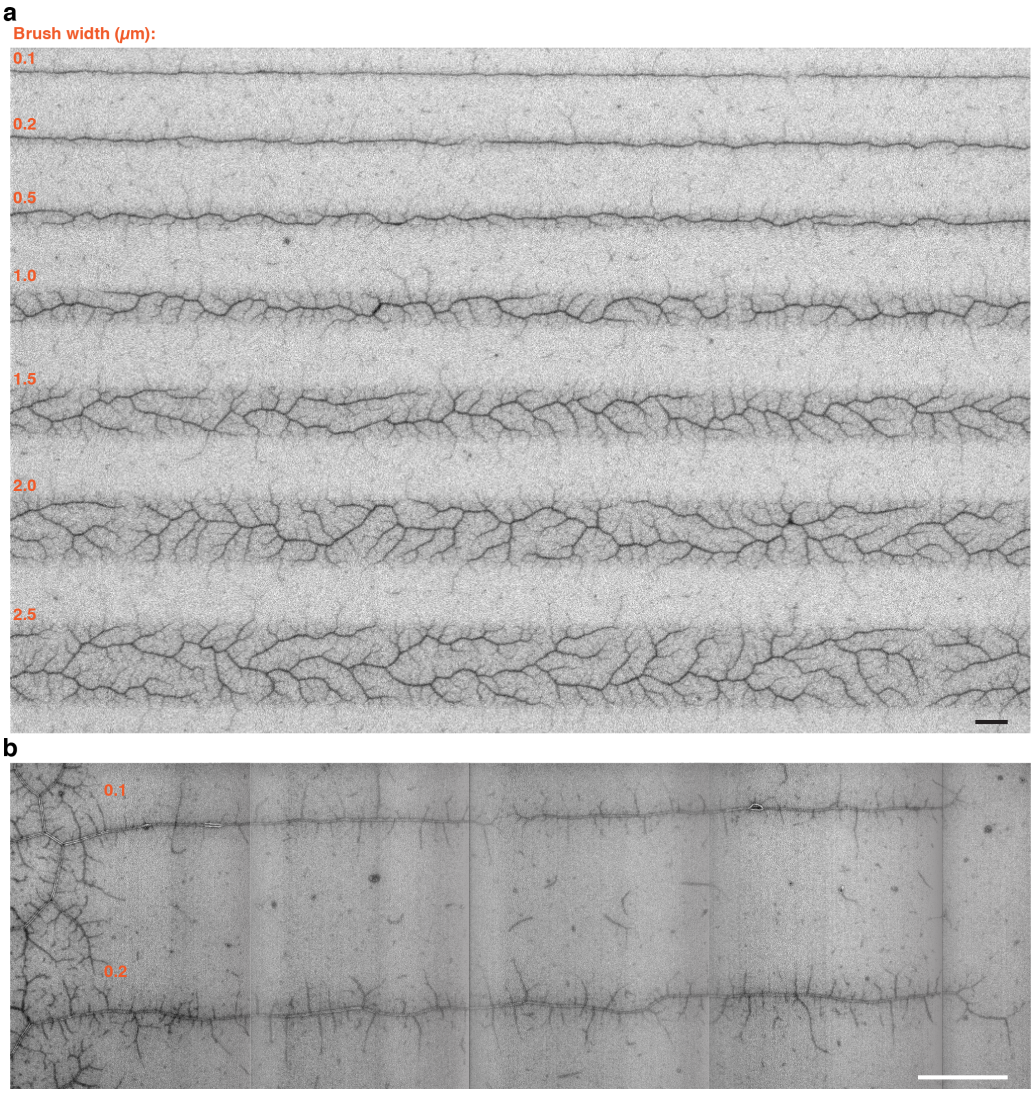

Figure 32: **Morphological transition from dendritic to 1D condensates. a,** SEM image of DNA brushes of various widths defined by EBL and condensed with spermidine. The confinement of the stripes in width suppressed the dendritic growth, resulting in a bundle which meandered within the boundaries of the stripe, and - at very small widths - in a one-dimensional condensate. **b,** Montage of several SEM images showing two thin condensed brushes connected to dendritic bundles on the left. The image illustrates the "straightening" of DNA bundles at small widths. While the lower condensate (0.2 μm brush) is bending within its constraints, the upper bundles (0.1 μm brush) appear very straight. The sample imaged for **a** was dried using the "fast" procedure, **b** more gently (see section 3.2). In the montage **b** linear grey filters were applied to compensate for charging effects in SEM. Scale bars: 1 μm.

major protrusions. Eventually, at a width of ≈ 100 nm a straight, one-dimensional condensate forms.

The confinement of brush width not only influenced the micron-scale morphology, but also the dimensions of DNA bundles at the nano-scale (figure 33a). Measurements of the diameters of DNA bundles following a "gentle" drying procedure (see section 3.2) are displayed in figure 33b.

We further analysed AFM scans to estimate the number of DNA strands in these bundles (figure 34a). We assumed that the DNA strands are aligned in parallel and in cylindrical close packing with a lattice constant of 29 Å [63]. Then, the number of DNA strands is proportional to the cross-sectional area of a bundle, *i.e.* the area under a topographic profile perpendicular to the orientation of a bundle (see figure 34b&c). We hence estimated the number of strands to ≈ 35 in bundles from 100 nm wide brushes and to over 100 in bundles from more extended 2D brushes (figure 34d). In AFM we also noticed a flattening of the bundles due to the tapping of the AFM tip (figure 66 in the appendix). This flattening however does not affect the cross-sectional area of a bundle and hence also not our estimation.

Finally, we deduced the density of DNA anchoring sites on a patterned Daisy surface from the number of strands in the bundles. In order to contribute to the cross-sectional area of a bundle at a certain position, DNA strands must be anchored in a region from which they can physically reach said position (figure 34e). For thin brushes, this region is restricted by the patterned width w of the brush and a radius r from which a bundle typically gathers DNA. Additionally, the region is bisected, since DNA strands usually bundle only towards the nucleation center. This region can therefore be written as the area $A(w, r)$ which is proportional to

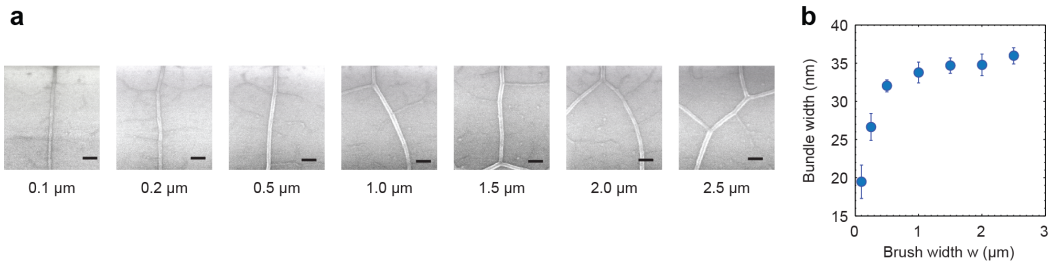

Figure 33: **DNA bundle widths in SEM. a,** DNA bundles (bright) condensed from brushes of various widths (0.1−2.5 μm). **b,** Quantification of bundle widths versus patterned brush width. Error bars show the standard error of the mean. Scale bars: 100 nm.

the number of strands $N(w, r)$ in a cross-section. The proportionality factor is the anchoring density σ. Fitting this simple model (with fitting parameters r and σ) to the data in figure 34d yields the anchoring density $\sigma = 350/\mu\text{m}^2$. This anchoring density is roughly in agreement with a previous estimation for UV-patterned Daisy ($1100/\mu\text{m}^2$ for 2 kbp DNA, from UV absorption [1]), considering the generally lower anchoring site density with EBL ($\approx 60\%$ at 5 μAs/cm^2, see figure 21c) and the different lengths of immobilised DNA (3.1 kbp here versus 2 kbp in reference [1]).

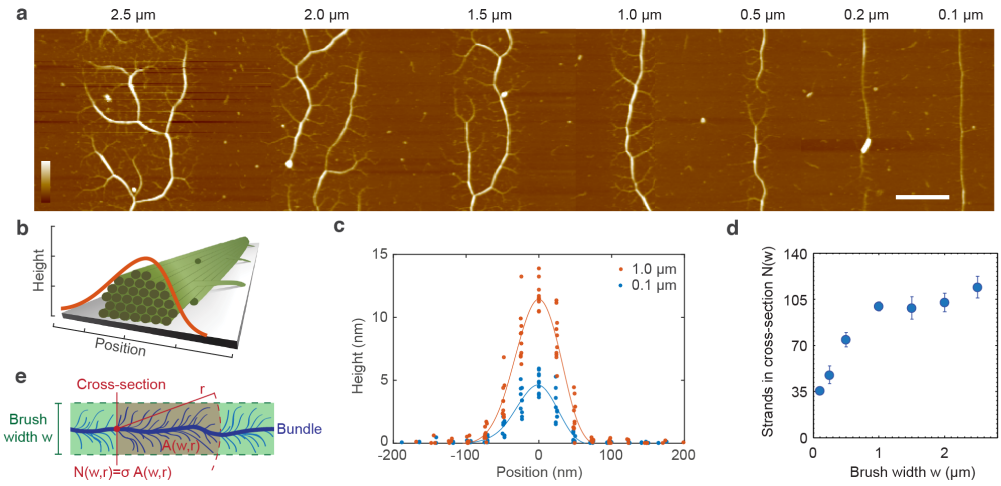

Figure 34: **Number of strands in DNA bundles. a,** Montage of several AFM scans of condensed DNA brushes of various widths. **b,** Schematic illustration of DNA (green rods) bundled to a 1D condensate. The red curve indicates a topographic AFM profile of a DNA bundle used to estimate the number of DNA strands constituting the bundle. **c,** Ten AFM profiles (dots) for DNA bundles from 1.0 μm (orange) and 0.1 μm (blue) wide brushes. The (approximately) average profiles are given by spline fits (solid curves). **d,** Estimation of the number $N(w)$ of DNA strands in a bundle cross-section (error bars indicate the standard error of the mean). **e,** Estimation of the DNA anchoring density σ. Only strands (blue lines) anchored in the red region $A(w, r)$ can contribute to the bundle cross-section (red line). Scale bars: 1 μm, height bar: 20 nm.

5.2 Condensation Dynamics

Aside from the morphology, the reduction of brush width also affected the condensate growth. We tracked the propagation of condensation fronts *via* fluorescence microscopy in brushes of various widths (figure 35a) and found a deceleration of growth with reduced brush width (figure 35b).
Additionally, 1D growth displayed a greater variation compared to 2D condensation (figure 36). This stochasticity of the condensation process emphasises the low dimensionality of the the thin brushes, which makes bypassing defects, *e.g.* areas with a lower DNA grafting density, more difficult.
Without insight into the condensation process at a single-molecule level, for now we can only speculate about the mechanisms responsible for the width-dependency of bundle growth. We hypothesise that the condensation of a DNA strand, whose negative charge has been mostly neutralised, occurs in two steps: first, the diffusive motion of the strand *until* it finds a nearby bundle and establishes a stable connection to it; second, the alignment of the strand with the bundle, stabilising the adhesion and promoting the accretion of additional strands. Both processes might simply speed up with the amount of nearby, condensed DNA, which is obviously higher for wider patterns. As we will show in the following section, a model

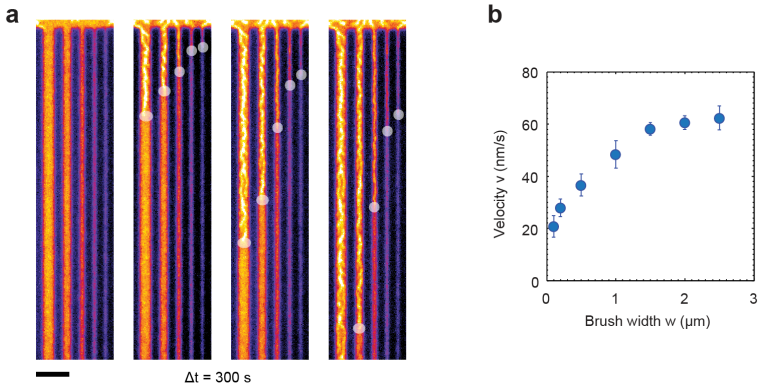

Figure 35: **Width-dependent condensation speed. a,** Fluorescence images of stripe-shaped DNA brushes (1.5, 1.0, 0.5, 0.2 and 0.1 μm in width) connected to a large, nucleation-prone region (top). After nucleation, the condensates (bright) grow along the stripes at different speeds (time intervals $\Delta t = 300$ s). The condensation fronts are highlighted by white ellipses. **b,** At brush widths below twice the contour length of the DNA ($\approx$2 μm), the condensation front velocity decreases. Scale bar: a, 5 μm.

based on the hypothesised mechanism is in principle able to reproduce dynamics and structures shown so far.

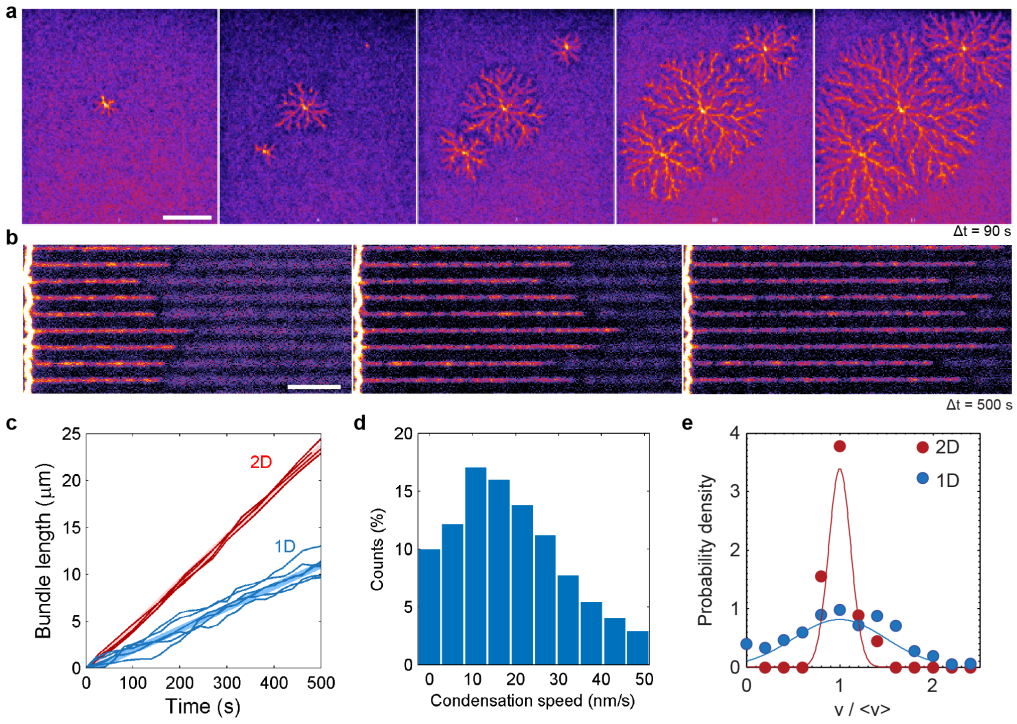

Figure 36: **Growth speed variation in 1D and 2D DNA condensation. a,** Fluorescence images of a condensing, extended 2D DNA brush at time intervals $\Delta t = 90$ s. **b,** Growth of 1D bundles displaying variation in speed, clearly observable *e.g.* in the two stripes at the bottom (time intervals $\Delta t = 500$ s). **c,** Front propagation in time for several 1D and 2D bundles (data from fluorescence videos like **a**&**b**) revealing a rather continuous growth in 2D in contrast to varying speeds in 1D. The light red and blue lines indicate the mean growth. **d,** Histogram of front propagation speeds for 1D bundles for time intervals of 60 s. **e,** 1D growth shows a higher relative variation in speed (2D and 1D growth speeds normalised to their average). Fits to the data are Gaussians. Scale bars: a, 10 μm; b, 5 μm.

5.3 Simulation

In order to check the plausibility of the assumptions made above (at the end of section 5.2), we simulated the condensation of a lattice of DNA strands in a simplistic model. Specifically, the scope of the simulation was not to model diffusion and electrostatic interactions of DNA, but rather to test whether the width-dependent dynamics and structures can be reproduced without detailed molecular considerations. The simulation consists of two main parts, the modelling of the condensation dynamics based on a Gillespie-like algorithm, and the simulation of dendritic and 1D bundle formation.

Simulation of Dynamics

We simulated the time evolution of condensation using elements of a "Gillespie algorithm" [96], which represents a standard procedure for stochastic simulations of chemical reactions. We based our method on an idealised, hypothetical condensation process:

- DNA strands in a brush are anchored on a square lattice. This simplification is mainly owed to the technical handiness of matrix calculations, even though random anchoring sites would probably yield a more accurate representation of the reality.
- After nucleation, condensation proceeds by adsorption of strands at the condensation front, *i.e.* only strands with at least one condensed neighbour can join a bundle.
- The probability of a strand for condensation depends on the amount of nearby, condensed DNA and therefore on the width of the DNA brush and on the position of the strand within the brush. For instance, a strand at the edge of a wide brush has less neighbouring strands and is hence generally less likely to "encounter" a nearby condensate than a strand in the center of the same brush.
- Once a strand is condensed, it does not revert back to the brush (no backreactions). Due to the stability of DNA bundles, in condensation experiments we

did not observe any significant de-condensation processes (without changing the salt conditions).

The implementation of this model is illustrated in figure 37a and is realised in several steps:

1. Setup: A binary matrix is generated which saves the state - condensed or non-condensed - for each strand. Except for the position of nucleation, at the start of the simulation (time $t = 0$) all strands are set to "non-condensed". The dimensions of this "state matrix" are set to agree with the estimated DNA surface density (section 5.1) and the desired width and length of the simulated brush. Another matrix of the same dimensions ("time matrix") saves the time of condensation of each strand.

2. Condensation front: The algorithm looks for all non-condensed strands at the condensation front, which in figure 37a correspond to all red strands with a green neighbour. Not only the four horizontal or vertical, but also diagonal neighbours are considered (8-connected neighbourhood).

3. Condensation probabilities: Depending on its position in the cross-section of a brush, *e.g.* at the center or an edge, each candidate strand is attributed a condensation probability, which determines the "type" of a strand. Here, we assumed that this probability depends on the amount of nearby accessible, condensed DNA. The amount of nearby DNA increases with the patterned area A which overlaps with the exploration range of the strand (red areas in figure 37b). However, much of that DNA may be concealed inside a DNA bundle and may therefore not contribute to increasing the condensation probability. We therefore set the probability proportional to the surface of the bundle, which is formed by DNA strands anchored in the region A. The bundle's surface is roughly proportional to the square root of the number of constituting strands, which in turn is proportional to the area A in which they are anchored (hence probability $\propto \sqrt{A}$). Due to the square lattice there is only a finite number of vertical positions and therefore only a finite set of probabilities.
   In the context of a standard Gillespie simulation, the "types" of strands would correspond to chemical species with different reaction probabilities. Here,

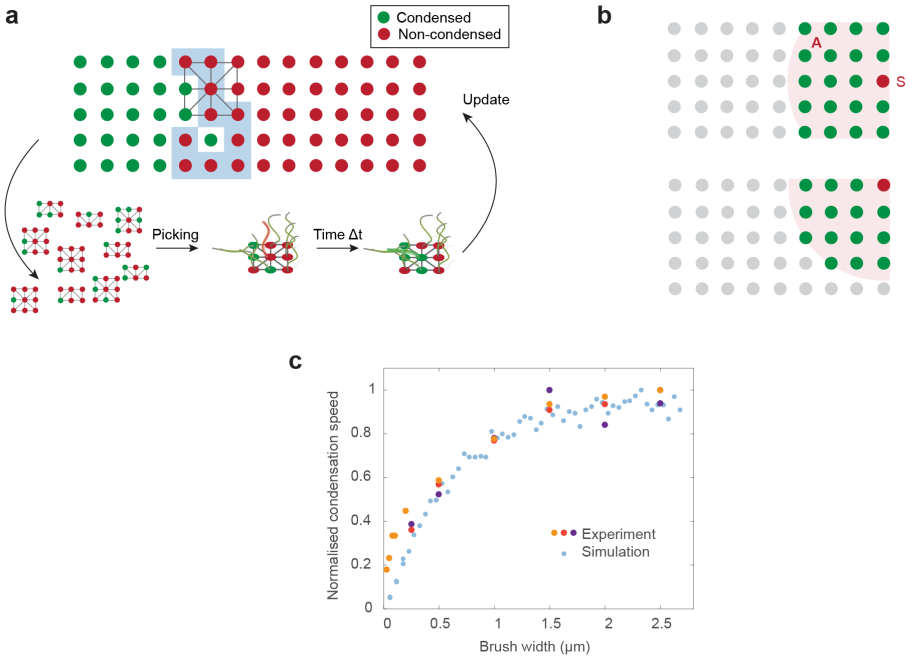

Figure 37: **Simulation of condensation dynamics. a,** A matrix contains the states (condensed or non-condensed) of all strands in a simulated brush. The algorithm looks for all non-condensed strands (red) with a condensed neighbour (green) at the condensation front (blue), assigns those candidate strands a probability of condensation and picks one of them according to the Gillespie algorithm. Furthermore, the algorithm determines a time interval Δt, during which the chosen strand will condense. Now the algorithm updates the time and the strands' states, and proceeds to the next iteration. **b,** Illustration of the concept which determines the condensation probability of a strand based on its vertical position in a brush. For instance, a strand S in the center (red dot) on average has more potential attachment sites (condensed DNA) in reach (red area A) than a strand at the edge of the brush. **c,** Comparison of experimental and simulated data sets of condensation speeds depending on brush widths. Simulated brushes had a length of 10 μm. All data sets were normalised to their maximum.

strands S of types μ "react" with probability c_μ to form the reaction product, *i.e.* a condensed strand S_c:

$$S_\mu \xrightarrow{c_\mu} S_c$$

4. Picking (Gillespie): First, one type of strand is selected for condensation according to the Gillespie algorithm. Thereby, the algorithm takes into account the numbers of strands associated with the various types of strands. Second, one distinct strand associated with the selected type is picked at random to condense.

5. Timing (Gillespie): Again accounting for the numbers of candidate strands and their condensation probabilities, a time interval Δt is calculated, during which the picked strand will condense.

6. Update: Finally, state and time matrices are updated. The simulation, now at time $t + \Delta t$, proceeds to the next iteration (step 2). It is noteworthy that in each iteration of the procedure we always execute only the first step of a typical Gillespie simulation.

7. Termination: The simulation terminates as soon as all strands are condensed and returns the time matrix.

The condensation times can then be used to calculate an average condensation speed depending on the simulated brush width. Figure 37c compares simulated speeds with experimental data sets. The shapes of the normalised graphs agree for a wide range of brush widths, except for deviations mainly at very small widths. Apart from the simplifications in the model, these deviations may be caused by the proximity effect, which can significantly widen very thin brushes ($\leqslant$ 100 nm) compared to their originally designed widths (x-coordinates in the graph).

Simulation of Structure

The simulation of bundle formation relies on the time matrix and on a set of rules which are outlined in the following:

1. A matrix of the same size as the time matrix is generated, which represents the patterned stripe (figure 38a, top) and serves to count the number of strands condensed in a certain region.
2. The strands condense one by one in the order given by the time matrix.
3. A condensing strand (red circle in figure 38a, center) establishes a stable adhesion to a nearby bundle (orange circle) and from there it aligns with the largest bundle (figure 38a, bottom) towards the nucleation site. The radius of the exploration range was limited to ≈ 600 nm, since several experiments (section 6.2.1) indicated that even at low salt concentrations the fully stretched configuration of DNA is rather unlikely. To account for the directionality of the bundling observed in SEM and AFM, we excluded circular growth and alignment against the direction of growth.

Figure 38b compares the structure of real condensates (top) to simulated DNA bundles (bottom). While there clearly are differences, the simulation still reproduces some main features of the DNA condensates, for instance the dendritic growth in wide patterns, the maximum number of "parallel" bundles per width or the competition of two "parallel" bundles for additional DNA at the transition from 2D to 1D.

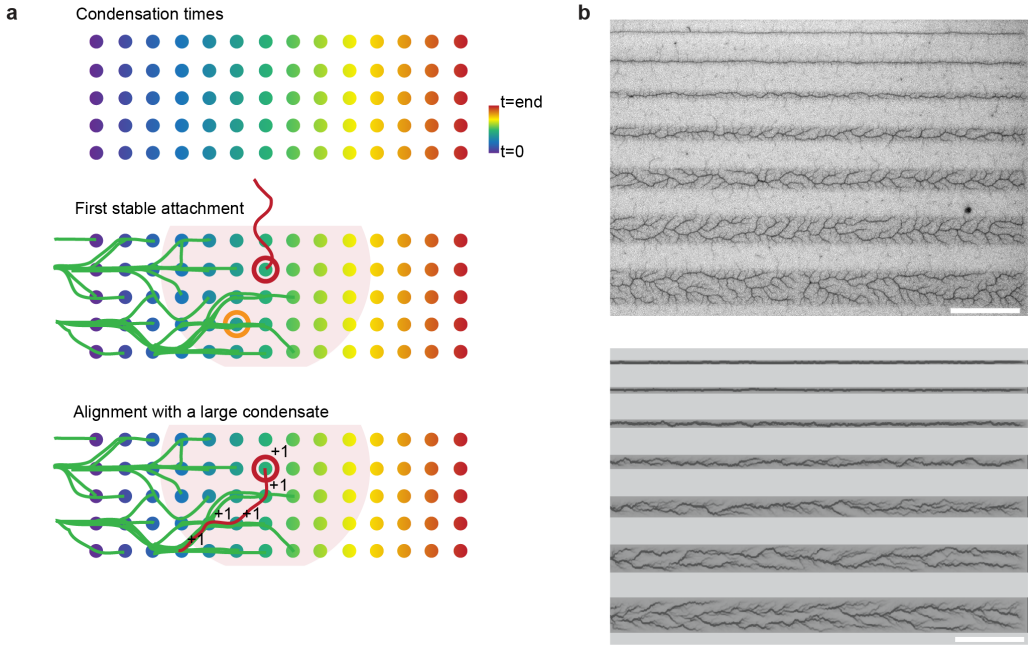

Figure 38: **Simulation of condensate structure. a,** Based on the matrix of condensation times (top), the structure of condensates is constructed strand by strand following a set of rules. A matrix of the same size is used to store the number of strands condensed in a certain region. Each strand (*e.g.* the red strand in the central schematic) attaches to a bundle (orange circle) in its proximity (red area, radius corresponding to ≈ 600 nm). From this point of first stable attachment the rest of the strand aligns with the largest nearby bundle. All matrix elements (positions) connecting the anchoring site and the point of first stable attachment, and all positions of the subsequent alignment are added +1 before the condensation of the next strand. **b,** DNA bundles imaged in SEM (top) are compared to simulated DNA condensates (bottom). Similarities include the dendritic structure, the number of "parallel" bundles per stripe width and the competition between "parallel" bundles at intermediate widths, *i.e.* the alternation of regions with a single main bundle or with multiple bundles. Scale bars: 5 μm.

Discussion of the Model

The simulation involves several assumptions and simplifications, some of which are substantiated by experimental data, while for some others we can only provide plausible motivations. Specifically, we here ignore possible cooperative effects and the condensation of DNA strands which are not located immediately at the condensation front. Also, we disentangled the simulation of dynamics from the structure formation process, thereby disregarding possible effects of actual bundle morphology on condensation kinetics. Furthermore, this coarse-grained method obviously cannot shed light on the internal structure of the DNA bundles, which might allow for a prediction of additional material properties.
However, the main objectives of the simulation were to provide a possible explanation for the width-dependent behaviour, and to investigate whether this explanation necessarily requires an electrostatically and thermodynamically precise description or if a kinetic model would suffice to roughly reproduce our experimental observations. Similar to the reasoning of Hud & Vilfan [57] (see also section 2.3), we also found that it is indeed in principle possible to model dynamics and structures formed by DNA condensation mainly based on stochastic kinetics and additionally on a positive feedback mechanism in bundle formation (strands align with the largest bundle nearby). In general, fundamental mechanisms such as diffusion-limited aggregation, are also responsible for the recurrence of some dendritic patterns in nature, for example in electric discharges ("Lichtenberg figures") or crystal growth.

5.4 Domain Wall Formation and Length of 1D Condensates

The extension of 1D bundles or dendritic condensates is typically restricted either by the size of the patterned DNA brush or by the emergence of additional condensates. Nucleation is a stochastic process and can therefore occur at any position along a non-condensed brush. In order to steer condensation along a brush in a certain direction and to minimise the number of nucleations, in many experiments we connected thin brushes to "nucleation-prone" regions which were simply large brushes with a high number of DNA strands and therefore with a high probability for early nucleation. Especially in very long 1D brushes however, additional nucleation sites could not be avoided, which resulted in counterpropagating condensation fronts (figure 39a). Wherever the two fronts met, the DNA strands joined one of the two possible condensation domains, similar to hair at a part. Such regions, in the following called "domain walls", are detectable in fluorescence microscopy, since the fluorescent labels at the end of the DNA strands are stretched in either one of the two possible directions, leaving a dark area of approximately twice the DNA contour length between fluorescent bundles. Also, these regions display a lower

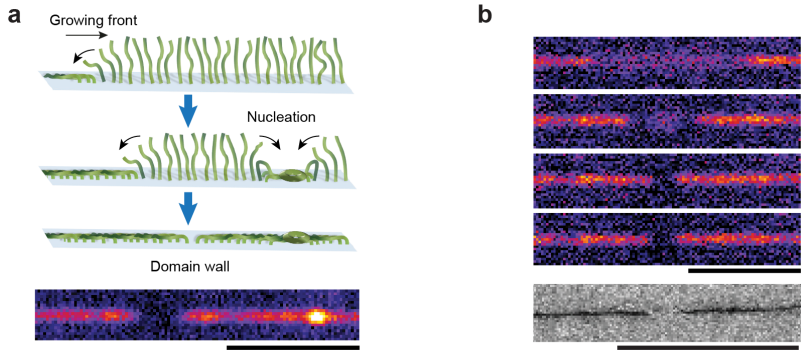

Figure 39: **Domain wall formation.** **a,** Illustration of DNA condensation from two nucleation sites, one on the left (not shown) and another one spontaneously emerging on the right. The counterpropagating growth fronts lead to the formation of a "domain wall", a region which separates two condensate domains. Since all DNA strands in a domain are stretched towards their nucleation site, the domain wall results devoid of fluorescent labels. The fluorescence image at the bottom shows a configuration similar to the last step in the schematic, with a nucleation site on the right and a dark domain wall in the middle. **b,** Time lapse fluorescence images showing the formation of a domain wall. Domain walls can furthermore be visualised by SEM (image at the bottom), since they are regions of lower DNA density. Scale bars: 5 μm.

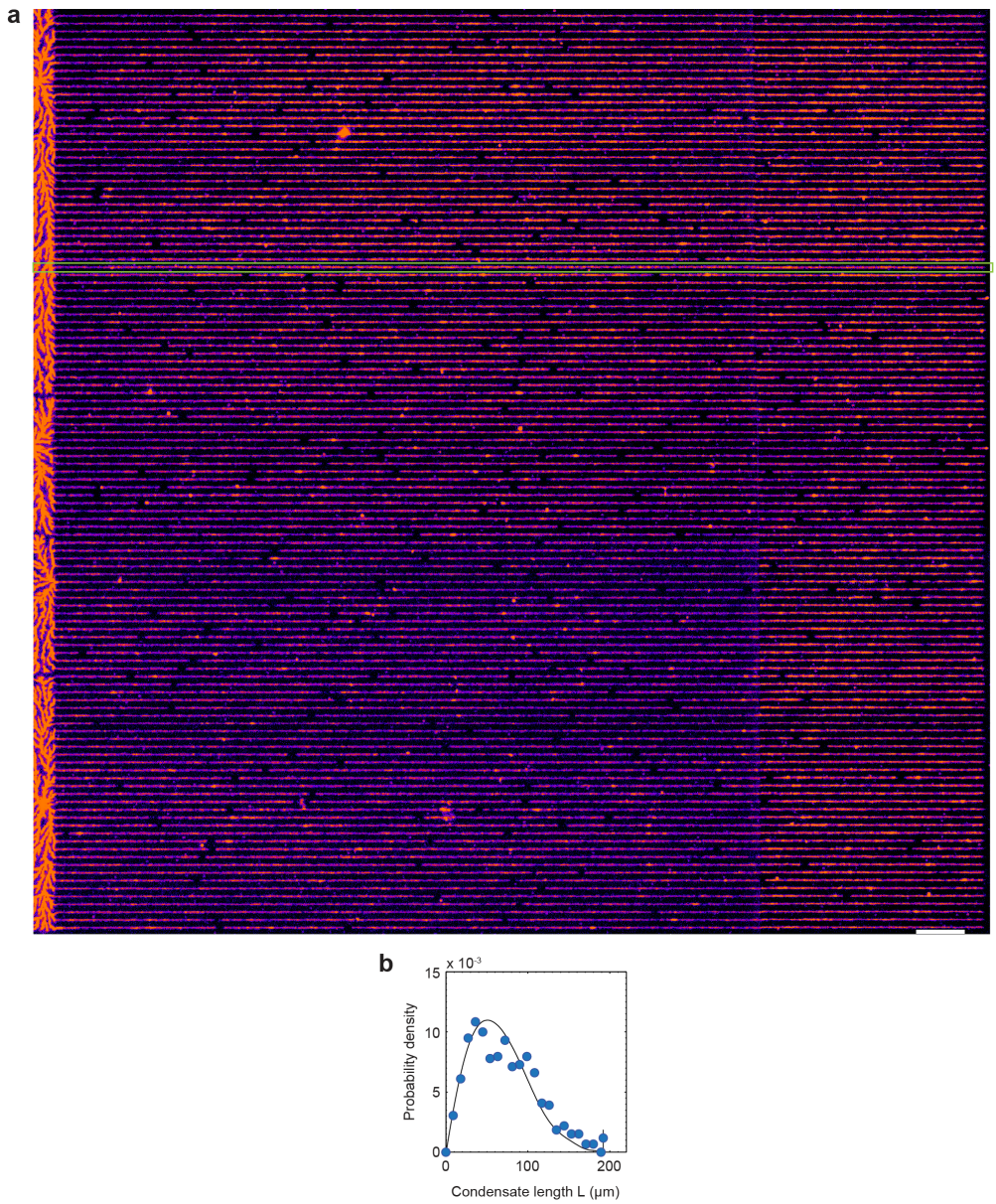

Figure 40: **Length of 1D condensates. a,** Fluorescence image (stitched from four individual images) of condensed DNA brushes of 100 nm width and 190 μm length, connected to a nucleation-prone region on the left. Condensation domains are clearly separated by dark domain walls, allowing for a measurement of bundle lengths. The green rectangle highlights a bundle which grew from the nucleation-prone region all the way to the end of the brush on the right side. **b,** Histogram of condensate lengths (blue circles, $n = 656$) with a mean length of 68 μm. The elevation of the last data point is related to the finite length of the DNA brushes. The solid line results from a simulation (see figure 41). Scale bar: 10 μm.

DNA density compared to the condensed bundles around them, which is why they are observable in SEM (figure 39b).

In order to determine the distribution of 1D condensate lengths, we created 100 nm wide and 190 μm long brushes connected to a nucleation-prone region. After nucleation and condensation, the lengths of bundle domains, reaching from one domain wall to another or to an end of a line, were measured in fluorescence microscopy images (figure 40a). The distribution of lengths from several images is shown in figure 40b. The mean length of the bundles was 68 μm, while approximately 1% of the bundles spanned the whole patterned length of 190 μm. Interestingly, the length distribution of bundles connected to the nucleation-prone region was found to agree with the unconnected condensates. Here, the benefit from an early nucleation seemed just to make up for the disadvantage of monodirectional growth. It should be noted that the measured lengths are strongly associated with the experimental conditions. For instance, the concentration of condensing agent affects nucleation and condensation rates. If a change in concentration favours nucleation, smaller bundles will be observed. Otherwise, bundles can grow longer without interference from other domains.

The observed length distribution was reproduced *in silico* by a simple simulation of 1D condensation based on random nucleation and constant bundle growth. Using an experimentally measured growth rate of 20.5 nm/s and a nucleation rate of 15 nucleation sites per hour and millimetre of uncondensed brush, we generated a length distribution (solid line in figure 40b) which agrees with the experimental data.

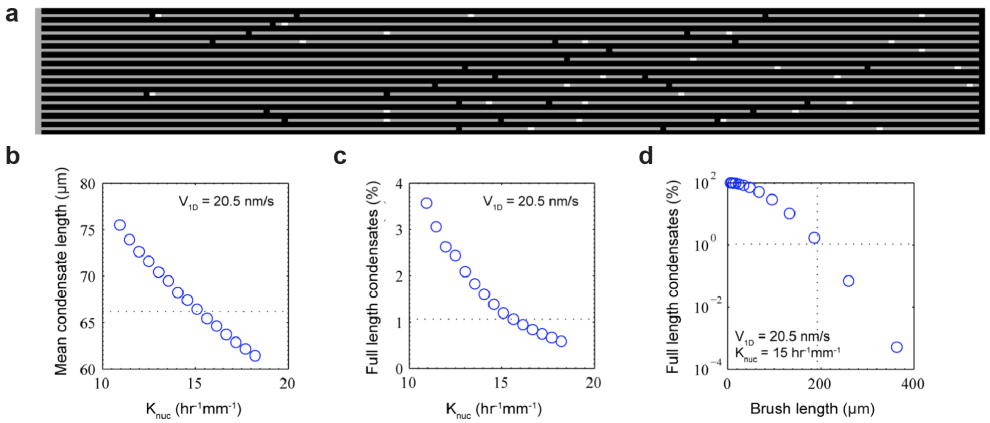

Figure 41: **Simulation of condensate lengths. a,** Visualisation of a simulation result (compare with the corresponding experiment in figure 40a). Several lines were "condensed" at a constant rate $v_{1D} = 20.5$ nm/s from a stripe on the left, representing a nucleation-prone region. Additionally, nucleation sites (bright spots) emerged at random locations along the lines at a rate $K_{nuc} = 15\,\mathrm{hr}^{-1}\mathrm{mm}^{-1}$. The resulting distribution of bundle lengths is depicted as solid line in figure 40b. **b-d,** Variation of nucleation rate and DNA brush length leads to changes in mean condensate length and the percentage of bundles grown over the full brush length. The graphs show that the simple model of random nucleation and constant growth reproduces all experimental observations (dotted lines) fairly well.

5.5 Resolution of DNA Brush Condensation

In science and technology the term "resolution" typically refers to the precision of a measurement technique, *e.g.* the minimum distance at which two point-like objects can be distinguished in optical microscopy [74, 75], or it can also indicate precision in fabrication, for instance the minimum distance between two droplets of ink ("printing resolution") or two lines created by ebeam lithography. The resolution of 1D condensation discussed in this section is related to the latter case, raising the question of how close two DNA brushes can be created and still yield two separate bundles. Since the answer is not easily found in a single value, we here refrain from a strict definition of resolution and instead look at two examples and their impact on the design of DNA brush networks.

Figure 42 shows SEM images of DNA brush lines condensed in parallel from a nucleation-prone region. At distances larger than 0.7 μm, two separate bundles form. At slightly smaller distances ($\approx$0.7 μm) bundles appear, which occasionally bridge the distance between the lines. At even smaller separation ($<$0.6 μm), the

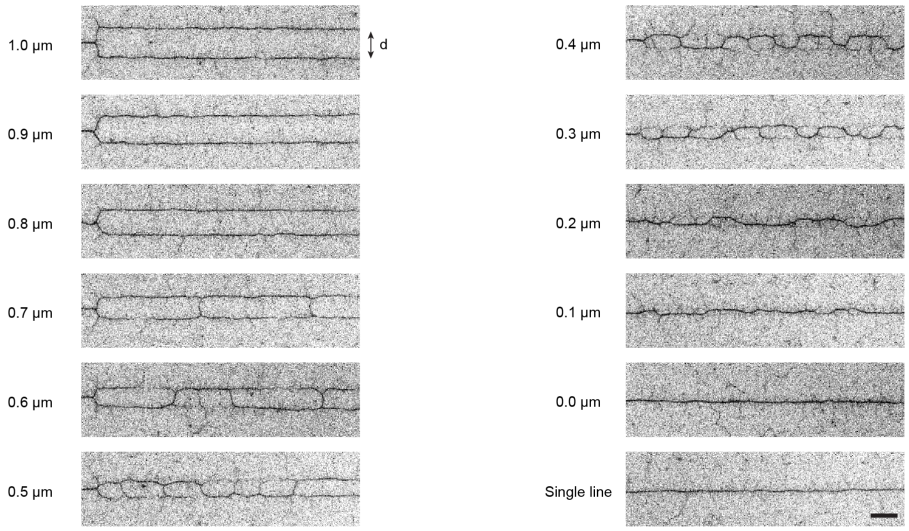

Figure 42: **Resolution of DNA condensation.** Parallel DNA brush lines (100 nm width) were written at a distance d and connected to a nucleation-prone region on the left side (not shown) in order to ensure that condensation would occur simultaneously on both lines. At large distances two separate condensates formed, while bridging bundles were observed below a distance of 0.8 μm. Bridging increased with the overlap of DNA strands from the two brush lines. Scale bar: 1 μm.

brushes constituted by DNA of 1 μm length can overlap constantly, thereby frequently forming bridges and eventually even preventing the emergence of two parallel condensates. These observations gave indications on the minimum distances in DNA brush designs, where parallel brushes should condense simultaneously without bridging, *e.g.* in the parallel arrangement of stochastic switches in section 6.2.2. If however brushes are not condensed at the same time, also larger distances up to one DNA contour length can be bridged (see section 6.2.1 for details).
A conceptually similar experiment is shown in figure 43, where ring-shaped brushes of various diameters were placed in contact to a nucleation-prone region. Again, the images show that at large diameters a bifurcation forms with two separate bundles, while the brush collapses into a single condensate at small diameters ($\leqslant$0.6 μm). These results helped to set the lattice constant for the honeycomb-shaped brushes of our DNA mazes (section 6.1).
Finally, both experiments also show that the resolution of condensation is mainly affected by the interaction range of the DNA brush, which depends on the DNA length, grafting density and salt concentrations. Compared to the resulting resolution ($>$ 500 nm), in our experiments the precision of ebeam lithography ($<$ 100 nm) played only a subordinate role.

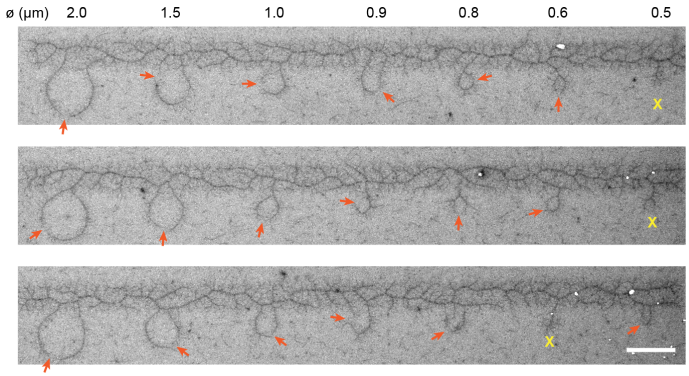

Figure 43: **Condensation of ring-shaped brushes.** Ring-shaped brushes of diameter ∅ were connected to nucleation-prone regions in order to determine whether condensates bifurcate (gaps highlighted by orange arrow) or collapse into a single bundle (yellow X). Scale bar: 2 μm.

5.6 Electrostatic Force Microscopy of DNA Bundles

Condensed DNA bundles consist of only few types of molecules: DNA as a negatively charged polyelectrolyte, trivalent spermidine, monovalent ions (sodium and chloride ions) and uncharged, but polar water molecules. The condensates are therefore structures with very high positive and negative charge densities. As described in section 3.3, Electrostatic Force Microscopy (EFM) probes basic electrostatic properties of a surface (figure 44a), revealing structures which display net charges or polarisability. Figure 44b shows EFM scans of two DNA brushes. Both were patterned, assembled and dried the same way, one however was condensed before drying. The compaction of the DNA by spermidine yielded a strong EFM phase shift for the vertical and the thin horizontal brush. Thicker bundles, *e.g.* from dendritic condensation of a large square brush (figure 45a&b), yielded an even higher contrast.

Without spermidine (figure 44b), DNA strands from the thin, horizontal brush lay scattered around their anchoring area and did not yield any EFM phase signal [97]. The thick, vertical brush gave only a weak signal, presumably due to aggregation of DNA in the drying process.

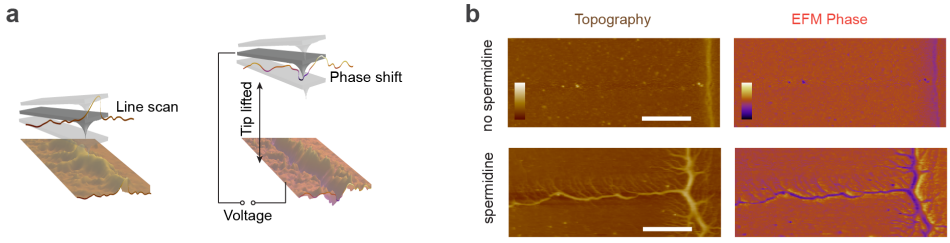

Figure 44: **Electrostatic Force Microscopy (EFM) of DNA Bundles. a**, Schematic illustration of EFM. First, a conductive tip performs a line scan of the surface in intermittent contact mode. Next, a voltage is applied between sample and tip, the oscillating tip is lifted (here: 50 nm) up from the surface and scans the same line again, but this time at constant height above the surface without touching it. Electrostatic interactions between tip and surface induce changes in the phase shift between the tip oscillation and its drive. These changes in phase shift give the EFM signal. **b**, Topographic and EFM scans (voltage: 10 V) of dried DNA brushes, both consisting of a thick, vertical brush and a thin, horizontal brush. Images at the top ("no spermidine") show a brush which was not condensed before drying and therefore only the thick brush gives some contrast in EFM. In contrast, the high charge densities in the condensed brush (bottom, "spermidine") show clear signs of polarisability. Scale bars: 1 μm; height bar: 20 nm; phase bar: 8°.

Swapping the sign of the voltage did not affect the sign of the phase contrast, indicating that the contrast is caused by the polarisability of the DNA bundles and not by a net over- or undercharge of the condensate. Together with results from literature [43], the polarisability suggests that the condensates are not entirely static, but that the retained water layer around the DNA allows for the rearrangement of ions and polar molecules in response to an external field.

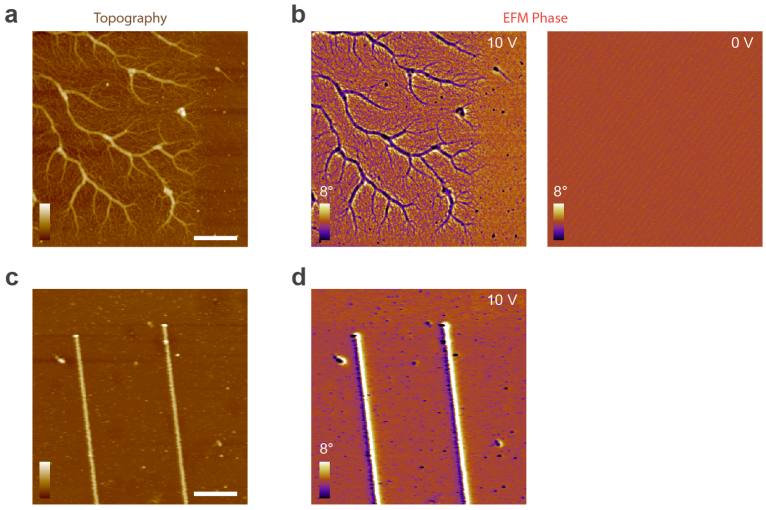

Figure 45: **Electrostatic Force Microscopy of Dendritic Condensates.** **a**, Topography and **b**, EFM scans of a part of a 10×10 μm^2 condensed brush. At a voltage of 10 V the thick bundles gave a strong EFM signal, while the control measurement at 0 V did not reveal any structure. **c**, As a reference sample we created lines of gold (by ebeam lithography and evaporation of titanium and gold), which **d**, gave a very strong EFM contrast due to the generally high polarisability of metals. Scale bars: 1 μm; height bars: 20 nm.

5.7 Nucleation Sites

High resolution imaging of DNA condensates using SEM and AFM allowed us to investigate not only the structure of DNA bundles, but also the morphology of nucleation sites. Similar to condensates formed in solution [14, 47], we found toroidal and rod-shaped nucleations. If only few DNA strands were involved in the formation of a condensate, *e.g.* few strands in an unpatterned region, we observed isolated toroids and rods (figure 46a). Thereby, the rods' length of only 100-200 nm and their rounded shape suggest that they are not formed by strands aligned in parallel, but also by wound or coiled DNA. Eickbush & Moudrianakis observed very similar rods, when dilute DNA (in 0.5 M ammonium acetate, 1 mM Tris, pH 7.5) was collapsed by 95% ethanol [47]. Therefore, some isolated rods might not originate in the condensation by spermidine, but instead they might be a byproduct of the drying process.

Other rod-like structures acted as nucleation sites for large dendritic or 1D condensates (figure 46b) and are therefore clearly spermidine-induced. The appearance of both toroidal and rod-shaped condensates indicates that the energy cost for continuous bending of DNA in a torus is similar to kinking the DNA at the end of a rod [98]. The toroidal nucleation sites displayed in figure 46b are deformed due to protruding DNA bundles. Depending on the number of connected bundles, the toroids were distorted to shapes resembling the eye of a needle, triangles or rectangles.

In order to verify that the structures observed in SEM are actually toroidal, *i.e.* that the apparent hole is not a mere imaging artefact, we also scanned them in AFM (figure 46c). Furthermore, from this data we could roughly determine the amount of DNA in a toroidal nucleation site. The section of a toroid shown in figure 46d allows for the estimation of toroid dimensions, *i.e.* the mean radius of the donut $R = 37$ nm (mean of inner and outer radius) and the radius of the two circular, cross-sectional areas $r = 27$ nm. Dividing the volume of the torus ($V_T = 2\pi r^2 R$) by the volume of a basepair, thereby considering a lattice constant of 2.8 nm ($V_{bp} = 1.4^2\pi \cdot 0.34$ nm^3) and hexagonal packing in the cross section, we calculated that the toroid contained roughly 75,000 bp. The size therefore approximately agrees with toroids condensed from solution under various conditions (≈60,000 bp, [98]), even though the mechanisms limiting the growth are presumably different for toroids condensed from solution and from a brush.

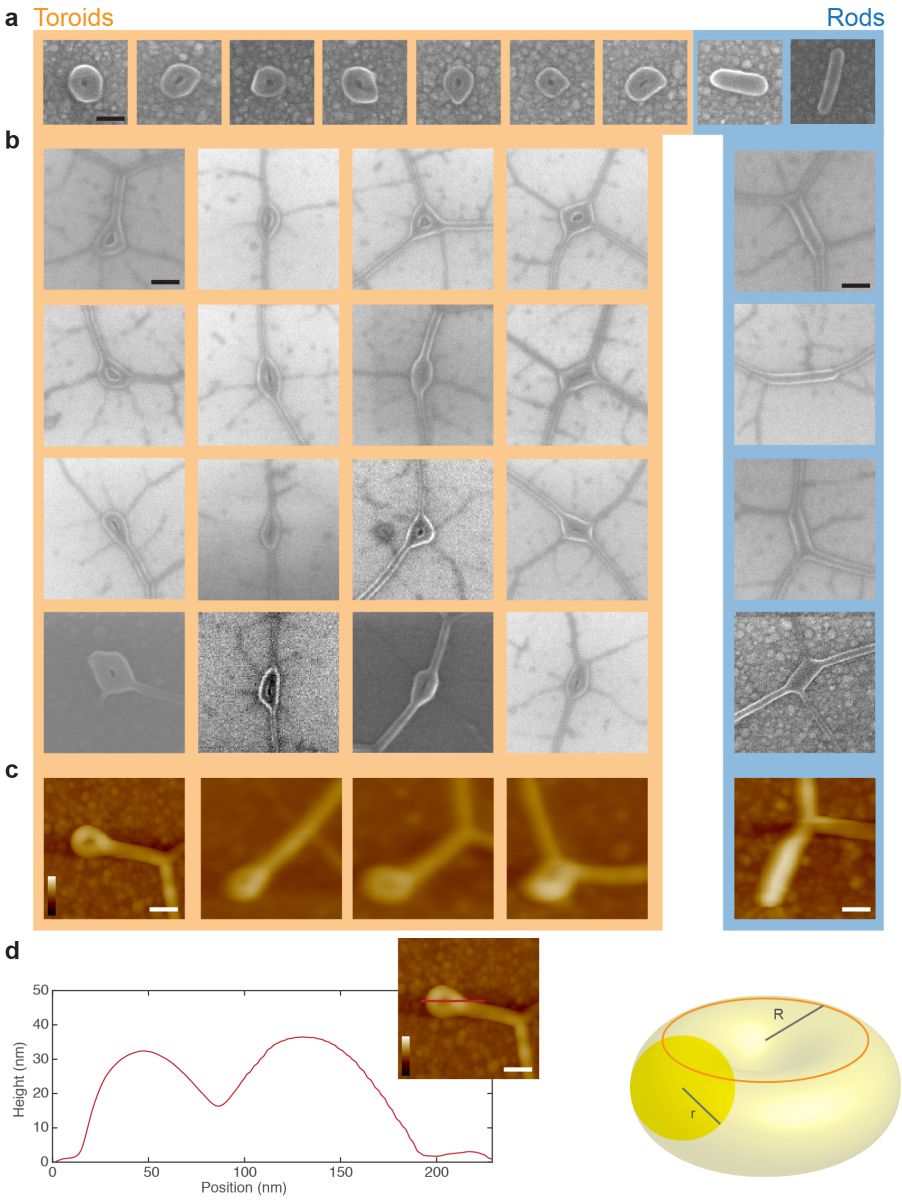

Figure 46: **Nucleation sites.** **a**, Toroidal (left) and rod-shaped (right) condensates formed by few DNA strands outside large brushes. **b**, Nucleation sites deformed by the growth of bundles. The first line of images shows this effect for 1, 2, 3 and 4 major bundles protruding from a single toroid. **c**, AFM images revealing that many nucleation sites are indeed of toroidal shape, *i.e.* with a hole in the center. **d**, Section along the red line in the inset image. From the section we estimated the dimensions of an ideal torus of comparable size (right) with the two radii $r = 27$ nm and $R = 37$ nm. Such a torus can contain approximately 75,000 bp of DNA. Scale bars: a-d, 100 nm; height bars: c&d, 100 nm.

Eventually, we also measured the frequency of toroidal and rod-shaped nucleation sites in arrays of condensed, small DNA brushes. By imaging several lines of the arrays in SEM, we found that under our experimental conditions both types of nucleation sites occur with only a slight preference towards toroids (figure 47). In contrast, spermidine-induced condensation of DNA in solution was found to yield mainly toroids, with only less than 10% rods [56]. In solution, higher amounts of rods were only achieved with methylated spermidine. From the present data we can only speculate that rod formation might be promoted by the high DNA density in a brush.

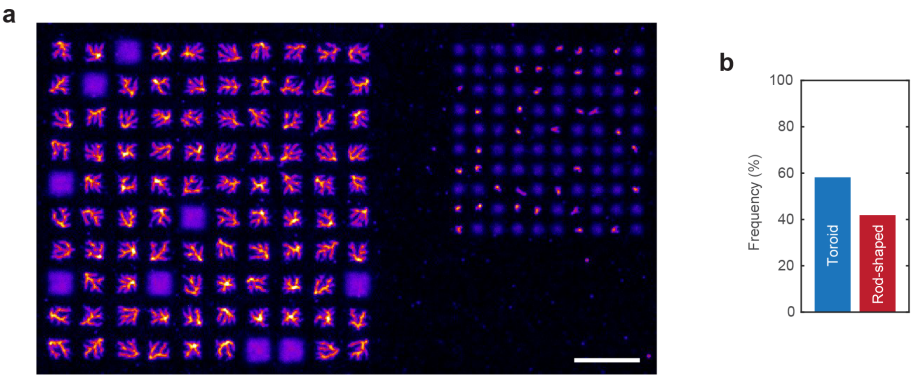

Figure 47: **Frequency of toroids and rods.** **a**, Fluorescence image of arrays of condensed DNA brushes (squares of 3×3 μm^2 (left) and 1×1 μm^2 (right)). Several lines of the arrays were scanned in SEM (images in figure 46b) to determine the type of nucleation site for each brush. **b**, Frequency of toroidal and rod-shaped nucleations ($n = 43$), showing that both types occur. Furthermore, we did not find a significant influence of brush size on the type of nucleation. Scale bar: 10 μm.

6 Condensation of DNA Brush Networks

The characterisation of 1D condensation now allowed for the design of more interesting patterns and networks like the two examples shown in figure 48a&b. One compares dendritic bundles to the condensation of a grid-like brush, the other shows the coastline of parts of Europe with some major cities connected by condensed lines. Such patterns of interconnected lines resemble mathematical structures called "graphs" (figure 48c). Graphs are collections of "vertices" and their connections ("edges"), which in the context of our DNA brushes will correspond to node positions and brush lines connecting them. In a weighted graph, edges additionally have a weight, which in the following will correspond to the length of a brush line. The origins of graph theory lie in Leonhard Euler's resolution of a mathematical

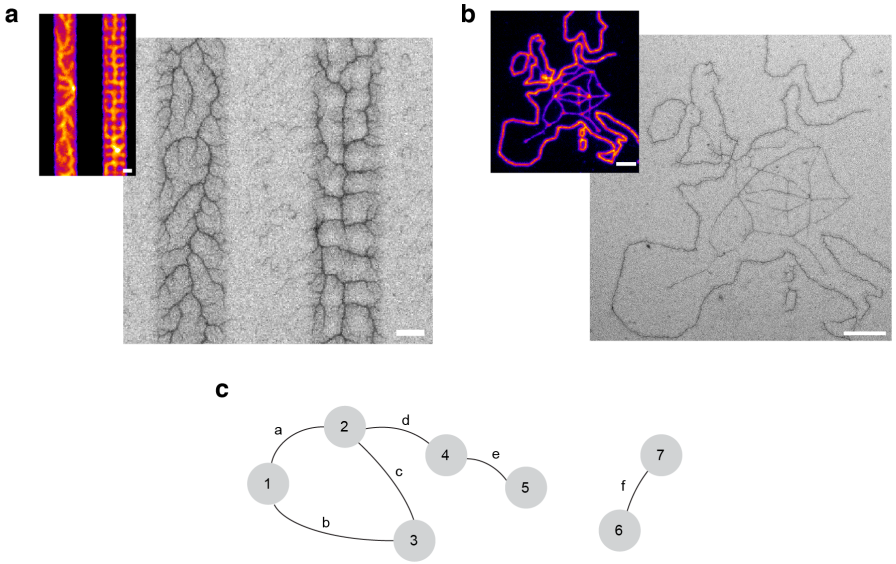

Figure 48: **DNA brush networks.** SEM (large, greyscale) and fluorescence (top left, coloured) images of interconnected, condensed brush lines. **a**, The condensation of two brushes of similar width, one continuous (left), the other one patterned like a grid (right, 500 nm wide stripes), reveals the impact of internal brush structure on the condensate morphology. While the continuous brush yields dendritic bundles, condensates from the brush on the right follow the lines and branch only at node positions. **b**, Condensed brush representing parts of the European coastline and some major cities connected by DNA bundles. **c**, Visual representation of a graph consisting of vertices (numbered circles) and edges (lines with letters). This example shows an undirected (edges have no direction) and disconnected (vertices 6 & 7 are isolated from the rest) graph. Scale bars: a, 1 μm; b, 5 μm.

problem called "Seven Bridges of Königsberg" [99], which involves path routing and topological questions. Since then, mathematicians and computer scientists have investigated efficient algorithms to solve problems in graph theory - with widespread applications, for instance in the determination of shortest paths by navigation systems (*e.g.* *via* Dijkstra's algorithm), in the optimisation of complex production workflows (*e.g.* by topological sorting based on depth-first search), or in the routing of wires on an electronic circuit board (minimum spanning tree) [100].
In the following sections we apply DNA condensation in unconventional approaches to computational problems. First (section 6.1), we use condensation to determine the shortest path through a graph representation of a maze, and discuss the procedure's relation to common path-finding and maze-solving algorithms. Second (section 6.2), we regulate condensation propagation based on a computer science model of so-called "stochastic circuits".

6.1 Mazes

The task of finding a way or even better - the fastest way - through a maze has intrigued humans since ancient times. Whether by using a ball of thread during the hunt of the monstrous minotaur [101] or by taking advantage of greedy computer algorithms, people have come up with creative solutions to the problem. In the past decades, several approaches relying on physical, chemical or biological processes, were demonstrated to aid in determining the shortest path through a maze. For instance, the amoeba-like slime mould *Physarum polycephalum* found the shortest path connecting two nutrient blocks in a small maze [102]. After filling the maze with tube-like projections called *pseudopodia*, contact to a nutrient source increased the frequency of local periodic contractions of the *pseudopodia*. The contraction waves propagated through the cell and triggered the retraction of *pseudopodia* with lower contraction frequencies, until only the *pseudopodia* on the shortest path were left.

Also some physical processes are suited for the task. Glow discharge in a gas medium between two electrodes takes the path of lowest resistance, *i.e.* typically the shortest path. Applying a high voltage to electrodes positioned at entrance and exit of a microfluidic maze therefore yields an electric arc tracing the shortest path [103]. Similarly, liquid flowing through a filled microfluidic maze takes the path of the lowest fluidic resistance. Hence, pumping a coloured liquid through a pre-filled maze with homogeneous channel geometry, again visualises the shortest path to the exit [104].

Yet another approach involves the initiation of a chemical wave (Belousov-Zhabotinsky reaction) at the entrance of a maze, followed by its propagation through the whole maze to the exit [105]. By tracing the propagation of the wave and excluding paths with counterpropagating waves, the shortest path can be found. Similar to this concept, we here designed several types of maze-shaped DNA brushes and showed how their condensation can facilitate the determination of the shortest path between an entrance and an exit.

6.1.1 Design

Before creating a DNA maze, it was necessary to decide on the type of maze, the routing of paths and to consider nucleation and the spacing of lines. In general, there are various types of mazes, *e.g.* the ancient and medieval depictions of labyrinths consisting of a single unbranched, wound path, or also logic mazes or three-dimensional ones. We here chose to design a two-dimensional maze with branching paths, dead ends and loops, one entrance and one exit. In contrast to traditional representations of mazes depicting walls which limit movement (figure 49a), our design - which was later written *via* ebeam lithography - consisted of the paths and therefore resembles a graph formed by lines interconnected at node positions (figure 49c).

Regarding the routing of paths, we opted for a regular structure based on a hexagonal lattice. In such a maze, we considered the junction of three lines as a node. In this configuration, lines at a node fan out at a large angle of 120° relative to each other, reducing the probability of bridging close to the node. In order to avoid bridging between unconnected lines even in the case of some unspecifically bound DNA, we set the length of a path element (side length of a hexagon) to 1.2 μm (see also sections 5.5 & 6.2.1).

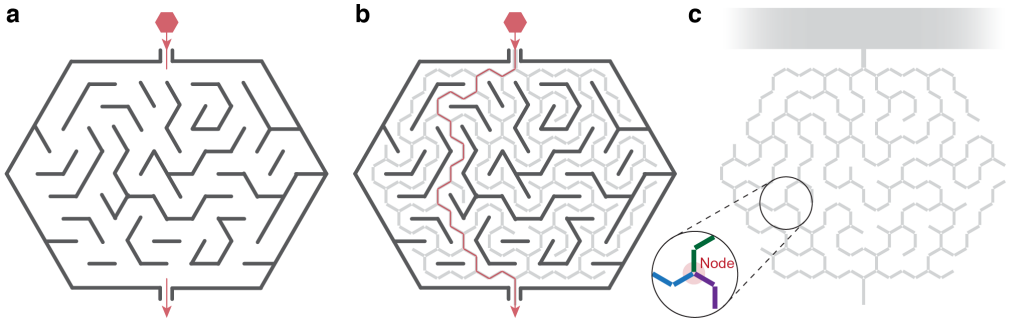

Figure 49: **Traditional and graph representation of a maze. a**, Traditional representation of a maze with lines representing walls, an entrance at the top (red hexagon) and an exit at the bottom (red arrow). **b**, Paths (light grey, aligned with a hexagonal lattice) added to the traditional representation. The red line indicates the shortest path connecting entrance and exit. **c**, Design written *via* ebeam lithography for a DNA condensation experiment. This representation resembles a graph constituted by nodes (or "vertices") at the junctions of lines ("edges"). In the following we only considered the junctions of *three* path elements as nodes (inset), whereas several consecutive path elements between two nodes were considered a single edge.

We also investigated whether the branching of condensation at a node influenced the dynamics of front propagation. We therefore created and condensed the two types of brushes shown in figure 50, which consisted of a loop and a stem protruding from a nucleation-prone region. The loop of the brush shown in figure 50a was asymmetric with two branching points on the right side, while the symmetric brush in figure 50b acted as a control. After condensation, the position Δx of the domain wall in the loop was measured in several such structures to determine whether or not branching introduced a bias towards one of the two sides. We found a distribution of Δx which was caused by the general variation of growth speeds (see section 5.2), but on average no significant deviation of domain walls from the central position (figure 50c). At least for the purpose of this work, we hence neglected potential effects of branching on condensation dynamics.

Yet another decision in the designing process concerns nucleation-prone regions. Our maze experiments required the condensation to start from a single, spatially defined position ("the entrance") and to propagate to the exit without the emergence of additional nucleation sites within the maze. Figure 51 shows two possible options for the positioning of the nucleation-prone region, either as a large patterned area outside the maze, or at the center of it. Figure 51a shows the latter option,

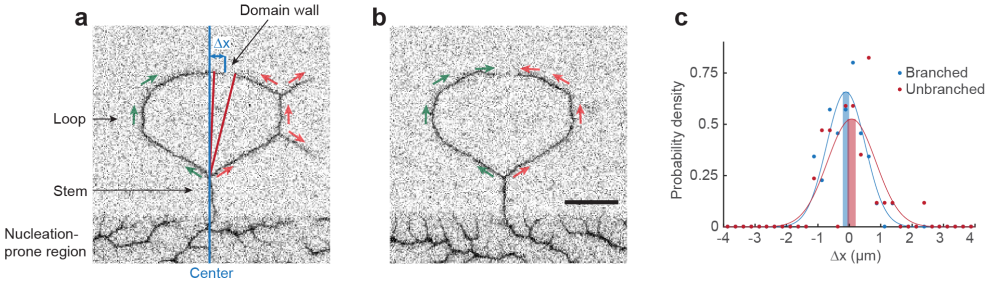

Figure 50: **Influence of branching on condensation dynamics.** To test whether the branching of condensation fronts influences the propagation speed, we designed a brush which consists of a loop region connected to a nucleation-prone region *via* a "stem". **a**, In the asymmetric design, one side of the loop contained two branching positions. A shift Δx of the location of the domain wall away from the central position (opposite of the stem) would indicate an influence of the branching on condensate growth. **b**, The symmetric design acted as a control. **c**, The normalised histograms of Δx gained from several replicas ($n = 35$) revealed no significant effect of branching on the growth speed (asymmetric (branched): Δx= (-0.12 ± 0.10) μm; symmetric (unbranched): Δx= (0.11 ± 0.13) μm; values are mean $\pm$ standard error of the mean; fitted curves to the histograms are Gaussian). SEM images, scale bar: 2 μm.

however also the only such maze (out of several tens of replicas) with a single nucleation site at the designated position. In this design, undesired nucleation along the paths was not surprising, considering that only one seventh of all DNA was located in the nucleation-prone region[2]. In contrast, another type of maze, which consisted of a total path length of ≈ 250 μm with a large, nucleation-prone region at the top (figure 51b), yielded approximately 25% of correct condensates. The remaining 75% of these mazes displayed additional nucleation sites (figure 51c). Due to the better performance of the latter design, external nucleation-prone regions were utilised in all other mazes displayed in this section.

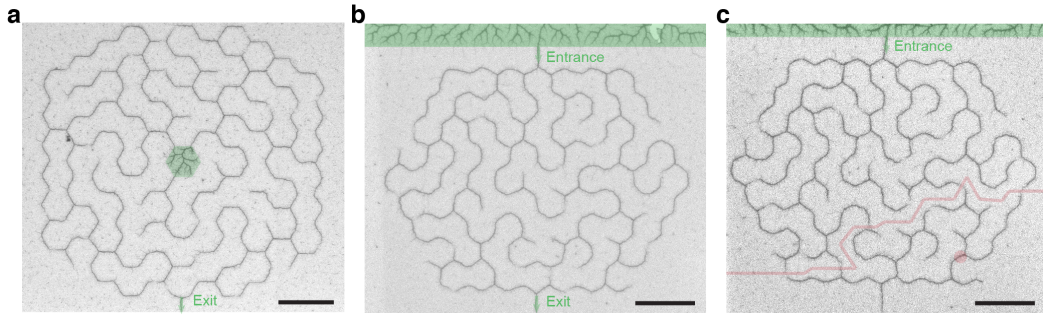

Figure 51: **Nucleation-prone regions for mazes.** The size and positioning of nucleation-prone regions strongly influences the portion of mazes with a single nucleation at a designated location. **a**, A small area in the center (highlighted in green) is unlikely to yield correct nucleation. The maze shown here was the only successful one, out of several tens of replicas. **b**, With a large nucleation-prone region (not fully shown, green) connected to the entrance of a maze we were able to achieve correct nucleation in 25% of the examined replicas ($n = 56$). **c**, The remaining 75% displayed one or more nucleation sites directly on the maze, making the structures useless in the determination of the shortest path from entrance to exit. The maze displayed here was condensed from the entrance and another nucleation site (presumed location highlighted by red circle). The red line separates the two condensation domains. SEM images, scale bars: 5 μm.

[2]Even though we could not use this type of maze in our studies, coloured versions of the SEM image in figure 51a were successful after all - as cover image of Nature Nanotechnology (Dec 2016, Vol. 11) [106], as image of the month in Nature News (Aug 2016) [107], Bild der Wissenschaft (Oct 2016) [108] and Wired UK (Feb 2017). Additionally, one of the mazes shown in figure 52 appeared in a feature on the occasion of Nature Nanotechnology's tenth anniversary [109].

6.1.2 Large Mazes - Finding the Shortest Path

When condensation fronts propagate through a maze starting from its entrance, they branch at each node, proceed on both branches and stop only at dead ends, domain walls or the exit. Without additional nucleation sites, bundles fill the whole maze, establishing a bundle which connects entrance and exit. Assuming an approximately constant bundle growth speed, the condensation front which reaches the exit first, must have taken the shortest route. Furthermore, since bundles only split, but never merge (section 5.4), the condensation of all loop-shaped brushes leads to the formation of domain walls and it is therefore impossible that multiple condensation fronts reach the exit. Therefore, the continuous bundle connecting entrance and exit indicates the shortest path. Figure 52a displays a condensed maze (design shown in figure 49c) with such a bundle (highlighted in green) connecting entrance and exit.

As discussed in section 5.2, bundle growth is however not constant, but varying stochastically, making each condensed maze unique (figure 52b&c). Here, the difference in path length between shortest and second shortest path was large enough that the bundle on the shortest path was always faster. Mazes with paths of very similar lengths are discussed in the following section 6.1.4.

The most convenient way of actually determining the shortest path by condensation consists in acquiring a fluorescence video of the condensation. Then, the condensation front which reached the exit can be tracked back to the entrance by playing the video in reverse.

Looking only at the outcome of condensation (figure 52a), finding the shortest path is apparently only facilitated, since the path connecting entrance and exit must still be determined in the tree-like structure. While finding this path in small condensed mazes is a quite easy task, it can be much more tedious for large ones. It is therefore interesting to see whether or not the simplification of the maze by condensation can aid algorithms in finding the shortest path.

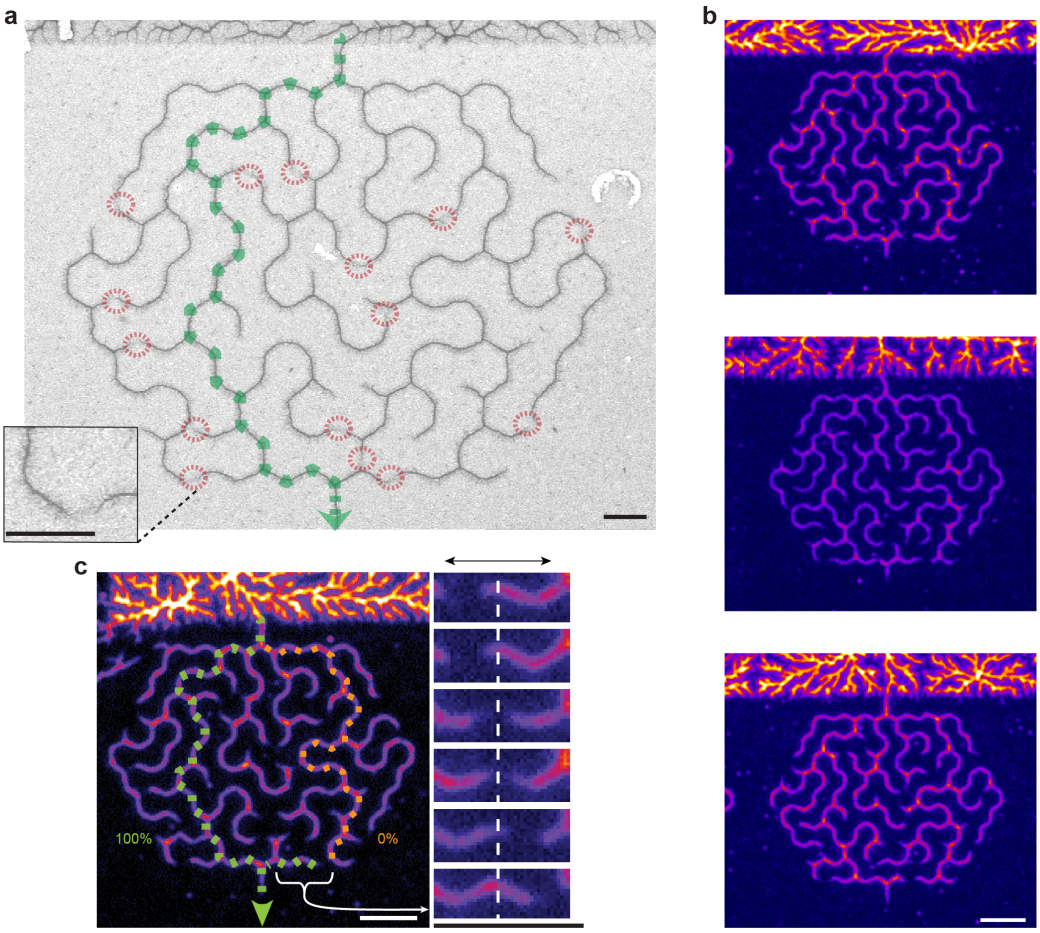

Figure 52: **Large mazes.** **a**, SEM image of a condensed maze. Red circles and the inset in the lower left corner highlight domain walls, where counterpropagating condensation fronts met. The green path indicates the only continuous bundle connecting entrance (top) and exit (bottom), which also corresponds to the shortest path through the maze. **b**, Fluorescence images of replicas of the maze shown in **a**. **c**, Due to fluctuations in growth speed, the positions of domain walls are unique in each condensed maze. The right inset shows the same magnified area in several replicas. Despite the variation, in all 14/56 correctly nucleated mazes we observed a continuous bundle on the shortest path (green), while the second shortest (orange) was never realised. Scale bars: a, 2 μm; b&c, 5 μm.

6.1.3 Condensation and Path-Finding Algorithms

Comparing the maze as an uncondensed brush to the condensed pattern, we note one major topological difference. While the designed graph G contains circular paths ("cycles"), the condensed pattern corresponds to a spanning tree, *i.e.* a connected graph which contains the same vertices as G, but edges do not form cycles. This change in topology can simplify the identification of the shortest path from entrance to exit, but also the determination of an escape path from within the maze.

Finding a Path through or out of a Condensed Maze

Without cycles, the condensed maze forms a "simple" maze, *i.e.* a maze from which it is very easy to escape by following two rules: Starting at any position in the maze, 1) consistently turn left (or right) at any junction. 2) Only when reaching a dead end, turn around 180°, then continue walking (figure 53a). The reason for this algorithm to work is that - due to the lack of loops - there are no "isolated" walls, which also means that all walls are "outer" walls. Consistently following the outer wall in one direction will inevitably lead you to a breach, in our case to the entrance or the exit. Furthermore, if one starts at the entrance of our condensed maze and follows this algorithm, the first breach will be the exit. Especially when starting from within the maze, this strategy might not work in the presence of closed loops, since one might end up running in circles (figure 53a). The simplification of the maze therefore allows for a very simple determination of a solution, which for now however does not necessarily correspond to the shortest one.
Inspired by the way Theseus navigated the labyrinth of the Minotaur in Greek mythology, an algorithm can be devised to find the shortest path through the condensed maze (in terms of graph theory, the algorithm corresponds to a depth-first search). Theseus (or also a very simple-minded robot) immobilises one end of Ariadne's thread at the entrance and looks for a way through the unknown maze. Keeping the thread tight at all times and again following the two simple rules, he will eventually find the exit. Additionally to determining the exit (location of the Minotaur), the thread now traces the shortest path back to the entrance, which might be useful as a fast escape route (figure 53b). In mazes containing loops, the algorithm does not necessarily yield the shortest path.

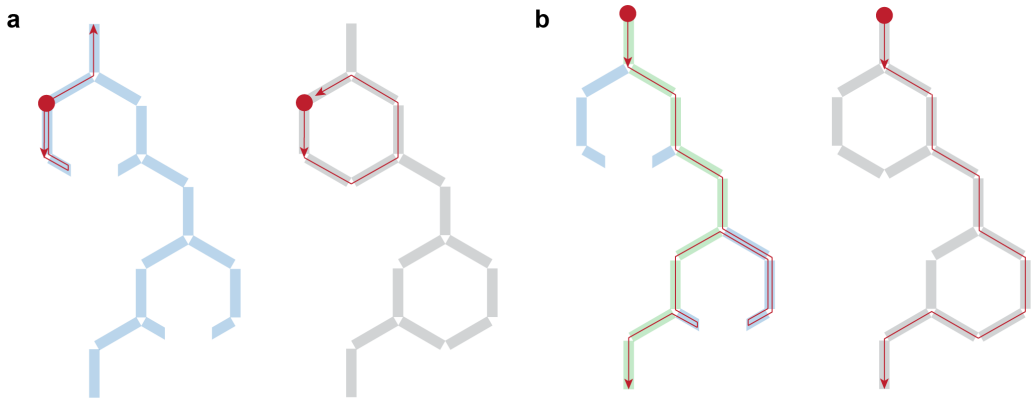

Figure 53: **Paths through a maze.** Escaping "simple" mazes such as the condensed ones, can be achieved by following two rules: 1) Consistently turn left (or right), 2) turn around at dead ends, then proceed. **a**, Starting from within the maze (red circle) and following this simple algorithm, it is easy to find an exit from the condensed maze (blue maze), while one might end up running in circles in a maze containing loops (grey maze). **b**, Starting from the entrance (red circle), the method reliably leads to the exit in both types of mazes. In a condensed maze (blue) it is possible to determine the shortest path simply by attaching one end of a thread at the entrance and holding the thread tight at all times. Once the exit is found *via* the algorithm, the shortest path is traced by the thread (highlighted in green). This procedure does not work in the case of the non-condensed maze (grey).

Condensation and Dijkstra's Algorithm

The shortest path between two vertices in a graph (or two cities on a road map) can be exactly computed by "Dijkstra's algorithm" [110]. This greedy algorithm operates on a graph which contains only edges with non-negative weights (here: distances between nodes). In the following we will discuss how it can be related to the condensation-based determination of the shortest path through a maze. In this context, we defined a node as a junction of *three* path elements. Consecutive path elements connecting two nodes are considered a single edge.
Figure 54 illustrates how the following steps are executed in order to find the shortest path between a *starting* node and a *destination*:

1. Mark the starting node as the *current* node and as *visited*, determine the distances to all neighbouring nodes and remember them in a *list*. Then find the closest neighbour, mark it as *current* and *visited* node, and delete its distance from the *list*. Remember the *parent* node (in this case the *starting* node), *i.e.* the previously *visited* node which is now closest to the *current* node.

2. Determine the distance between each non-*visited* neighbour of the *current* node and the *starting* node, and add the distances to the *list*. Set the node with the shortest distance in the *list* as *current* and *visited* node and delete the distance from the list. Remember the *parent* node.

3. Repeat step 2 until the *destination* is marked as *current* node.

4. The shortest path can now be traced back following the *parent* nodes.

In the case that in steps 1 or 2 the list contains two or more equally long, shortest distances, one corresponding node can be selected at random as the next *current* node.
In order to compare Dijkstra's algorithm with the condensation-based method, we first establish a defined procedure for finding the fastest route by condensation. We thereby consider path junctions in the DNA maze as nodes and neglect the stochasticity of growth.

1. The maze is condensed from the entrance (*starting* node) and the process is recorded in a fluorescence microscopy video.

2. Acquisition of the video is terminated, when a condensation front reaches the exit (*destination*).

3. To identify the shortest path, play the video in reverse and trace back the condensation front from the exit to the entrance.

We can identify several similarities between the two approaches. Until their termination, both processes *visit* (or condense) all nodes which are closer to the *starting* node than the *destination*. Here, one difference lies in the serial *visiting* of Dijkstra's algorithm versus the parallel propagation of condensation. Another common characteristic is that nodes are only *visited* once and that connections between *visited* nodes are excluded from further considerations, since Dijkstra's algorithm ignores all *visited* nodes in the search for the next *current* node and condensation between *visited* nodes yields domain walls. Also the backtracking of condensation fronts in a video resembles the determination of the shortest path *via parent* nodes. Due to the strong similarities, the condensation-based method can be roughly regarded as a physical implementation of Dijkstra's algorithm.

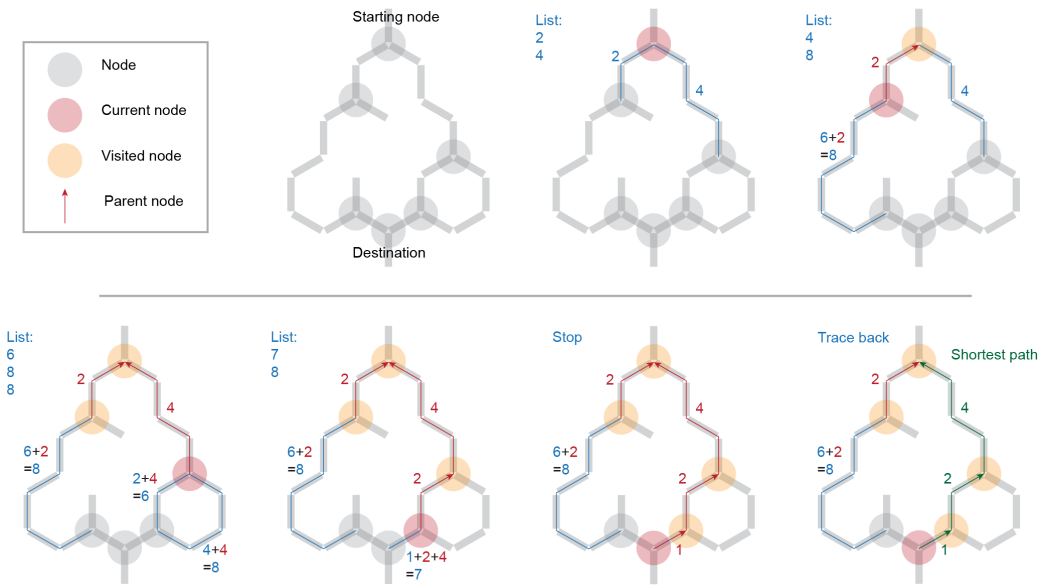

Figure 54: **Dijkstra's algorithm.** Demonstration of the algorithm on a graph consisting of several nodes, a *starting* node, a *destination* and paths connecting them. Step by step, it thereby searches for the next node to visit, which, among the neighbours of already *visited* nodes, is closest to the *starting* node (for details, see page 107). Blue numbers and lines indicate the distances to nodes which could be *visited* next. The *list* keeps track of these distances. The node corresponding to the smallest distance in the *list*, is *visited* next, *i.e.* set as the *current* node in the next step. The algorithm terminates, when the *destination* is *visited*. Remembering the *parent* node (indicated by the red arrows) at each step, allows for tracing the shortest path (green).

6.1.4 Stochastic Mazes - Ranking Several Paths

In contrast to the large mazes shown previously, we also designed smaller versions with paths of very similar lengths connecting entrance and exit (figure 55a). Due to stochastic variations in bundle growth speed (see also section 5.2), we expected to observe not only the shortest path, but a small ensemble of solutions. As displayed in figure 55b&c, the condensation indeed proceeds at varying speeds through identically patterned mazes, thereby yielding two individual condensed patterns.

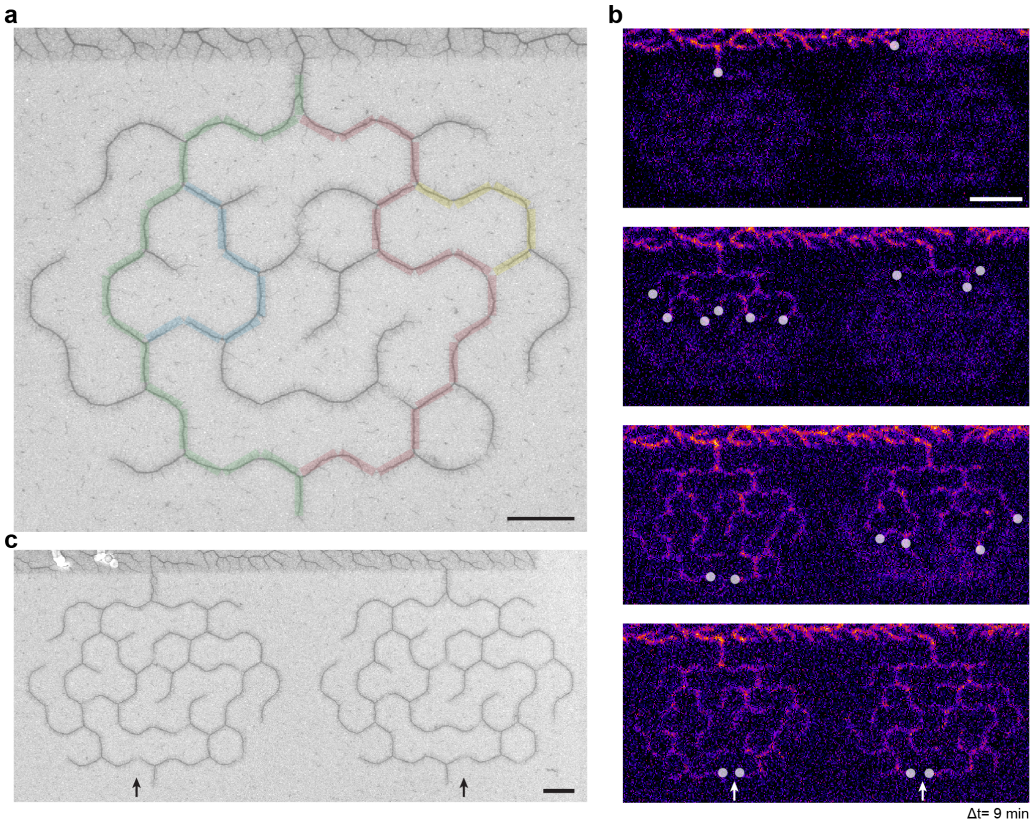

Figure 55: **Condensation of stochastic mazes.** **a**, SEM image of a condensed maze with several paths of similar length. The coloured lines highlight the solutions which were observed experimentally in replicas of this maze. **b**, Time-lapse fluorescence images (time intervals of $\Delta t = 9$ min, condensation fronts highlighted by white circles) of two identically patterned mazes. Due to stochastic fluctuations in bundle growth, the condensates are however not identical. In the left maze, the bundle on the shortest path reaches the exit first, resulting in a domain wall on the right side of the exit (highlighted by a white arrow). In the right maze a slightly longer solution is realised (domain wall on the left side of the exit). **c**, SEM image of mazes like the ones shown in **b**. Scale bars: a&c, 2 μm; b, 5 μm.

In order to observe and quantify the frequency of different solutions, we designed three types of small mazes and patterned several hundred replicas on a chip, of which ≈70% displayed correct nucleation. Figure 56a shows a symmetric type of maze with two main paths of the same length. As expected, left and right solutions were observed with approximately the same frequency. Another version (figure 56b) with very different path lengths showed only a single, *i.e.* the shortest, solution, analogously to the large mazes in section 6.1.2. The third type (figures 55&56c) contained several potential solutions of similar lengths, four of which were observed experimentally. In 157 correctly nucleated mazes, the shortest path was observed most often by far (85%), while the other three solutions were found in less than 10% each. The analysis of such an ensemble of stochastic mazes therefore provides a means to find not only the shortest path, but also to determine the probabilities of realisation for several other, slightly longer solutions.

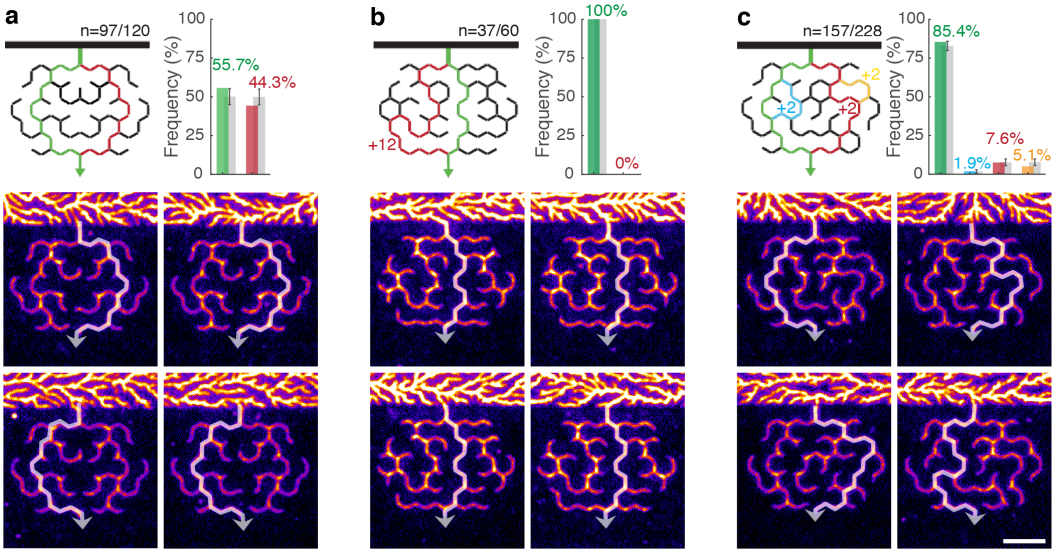

Figure 56: **Competing solutions in stochastic mazes.** Three designs of mazes with competing solutions: **a**, symmetric, **b**, with one short and one long solution, **c**, with several paths of similar lengths. Coloured paths were observed experimentally as solutions of the maze. Coloured numbers indicate additional path segments compared to the shortest solution. The fluorescence images show examples of condensed mazes for each design with the realised solution highlighted by a white arrow. n gives the ratio of correctly nucleated mazes and patterned brushes. For the correctly condensed mazes, the bar graphs next to each design indicate the observed frequency of solutions (colours of bars and paths in the design correspond). Grey bars with standard deviation as error bars display simulated data (for details see page 111). Scale bar: 5 μm.

The distributions of solutions (bar graphs in figure 56) are readily reproduced *in silico* based on a simple algorithm. For the mazes with only two competitive paths (figure 56a&b), two competing bundles were simulated with the position of the condensation front $x(t)$ determined by $x(t+\tau) = x(t)+\tau x'$, $x(0) = 0$, where x' denotes a growth rate taken from a normal distribution with a mean rate of 840 nm/min and a standard deviation of 240 nm/min, and τ=1 min. Mean growth rate and deviation were determined experimentally specifically for these mazes, since the lines investigated in figure 36 in section 5.2 were written at a different electron dose. Whichever condensation front reached the end first (or advanced further in the last step), was picked as the solution.

For the maze in figure 56c, 4 competitive paths were considered. Here, two paths each shared a part of their route. Therefore, a pre-selection was performed to determine which of two paths (green (5 path segments) or blue (7); red (7) or yellow (7)) was faster on the separate track. Then, the two faster paths were compared to determine the overall winner which reached the exit first.

In order to compare the simulation results to the experiment, we ran the simulation of a single maze for the same number of times as the number of mazes analysed in the experiment (n=97 (symmetric paths), n=37 (2 very different path lengths), n=157 (similar paths)). These simulated experiments were then repeated 1000 times to determine the mean outcome (height of grey bars in the graphs in figure 56) and the standard deviation (displayed as error bars). In spite of the simplistic nature of this simulation, the results agree well with the experiment, indicating that the condensation of DNA brush networks represents a robust and - within limits - predictable process.

In summary, we conclude that the condensation of a maze not only helps finding the shortest path, but also - based on the stochasticity of the process - some of the fastest routes.

6.2 Stochastic Circuits

Apart from solving mazes, we also applied condensation in our interpretation of "stochastic switching circuits", a circuit model based on probabilistic components. In contrast to deterministic switches, whose state (open or closed) is dictated externally or by logic circuit components (figure 57a), the circuits proposed by Daniel Wilhelm and Jehoshua Bruck contain stochastic switches [15], *i.e.* switches which are open or closed with a certain probability (figure 57b). A few simple circuits are shown in figure 57c, the first of which consists of a single switch with a probability $p = 0.25$ for the closed state (in general: $p \in (0, 1)$). This means that out of a large ensemble of circuits ≈25% are closed, while the rest is open. If two switches with different probabilities $p = 0.25$ and $q = 0.5$ are placed in series, the probability for finding a closed circuit drops to $p \cdot q \approx 0.13$. In contrast, a circuit containing the same two switches in parallel is more likely to be closed than a single switch: $p + q - pq \approx 0.63$. Similar to combinations of resistors or capacitors in electronic circuits, also many complicated stochastic circuits can be reduced to serial and parallel arrangements of sub-circuits and single switches, *e.g.* the last circuit shown in figure 57c with the overall probability for closed circuits: $p \cdot (p + q - pq) \approx 0.16$.
Interestingly, a serial arrangement of two switches can be interpreted as an AND gate with stochastic inputs (the states of the two switches). Similarly, the parallel circuit represents a "stochastic OR gate" (figure 57d). In their work, Wilhelm & Bruck furthermore showed that more advanced circuits could be used to generate probability distributions [15].
In the following sections we first show that condensation can bridge narrow gaps between DNA brushes with a stochastic time delay. We then demonstrate how we implemented these stochastically bridged gaps in systems inspired by the stochastic circuits discussed above.

6.2.1 Gap Bridging

In sections 5.2 & 5.3, we investigated the propagation and the variability of DNA bundle growth and modelled the process assuming that it is governed by stochastic reaction-diffusion mechanisms. Here, we intensified and visualised the stochasticity of bundle growth by creating brushes separated by gaps of various widths. When a condensation front reached a gap larger than ≈ 0.6 μm, propagation temporarily

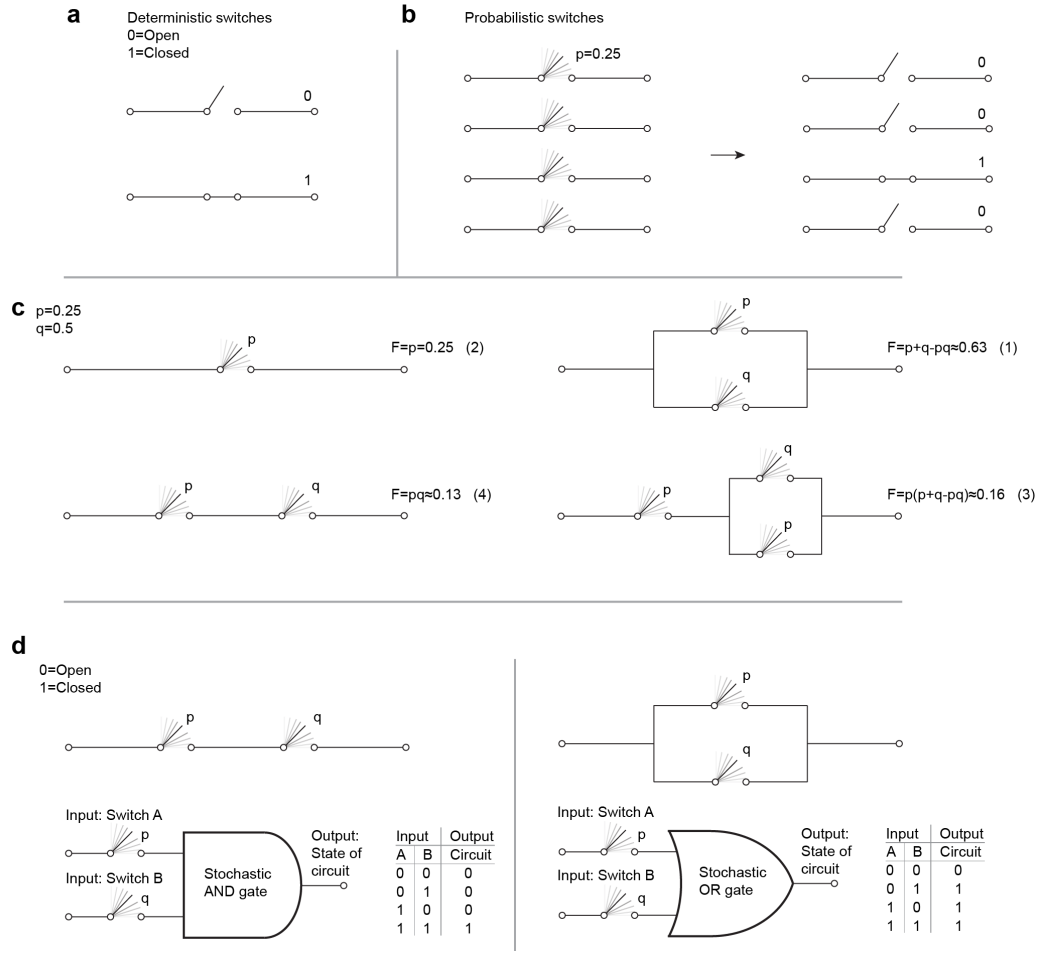

Figure 57: **Stochastic circuits.** **a**, Illustration of a circuit containing a deterministic switch in two different states (open and closed), drawn in analogy to electronic circuits. Deterministic switches are typically controlled externally or by logic circuit elements. **b**, In contrast, the state of a probabilistic switch is determined by its intrinsic stochasticity and is only biased by the probability p towards the closed state. For instance, the repeated observation of four switches with probability $p = 0.25$ yields - on average - one closed circuit and three open ones. **c**, The combination of two or more stochastic switches with probabilities p, q results in a circuit with an overall probability F for the closed state, which depends on the type of arrangement (in series, in parallel) and on the probabilities p, q. The numbers in brackets behind F relate them to the condensed stochastic circuits shown in figure 60. **d**, Interpretation of serial and parallel arrangements as logic gates with stochastic inputs. A circuit with switches in series is only closed (output: 1), if the two switches are closed (both inputs: 1, "stochastic AND gate"). In contrast, a circuit with two parallel switches is only open, if both switches are open ("stochastic OR gate").

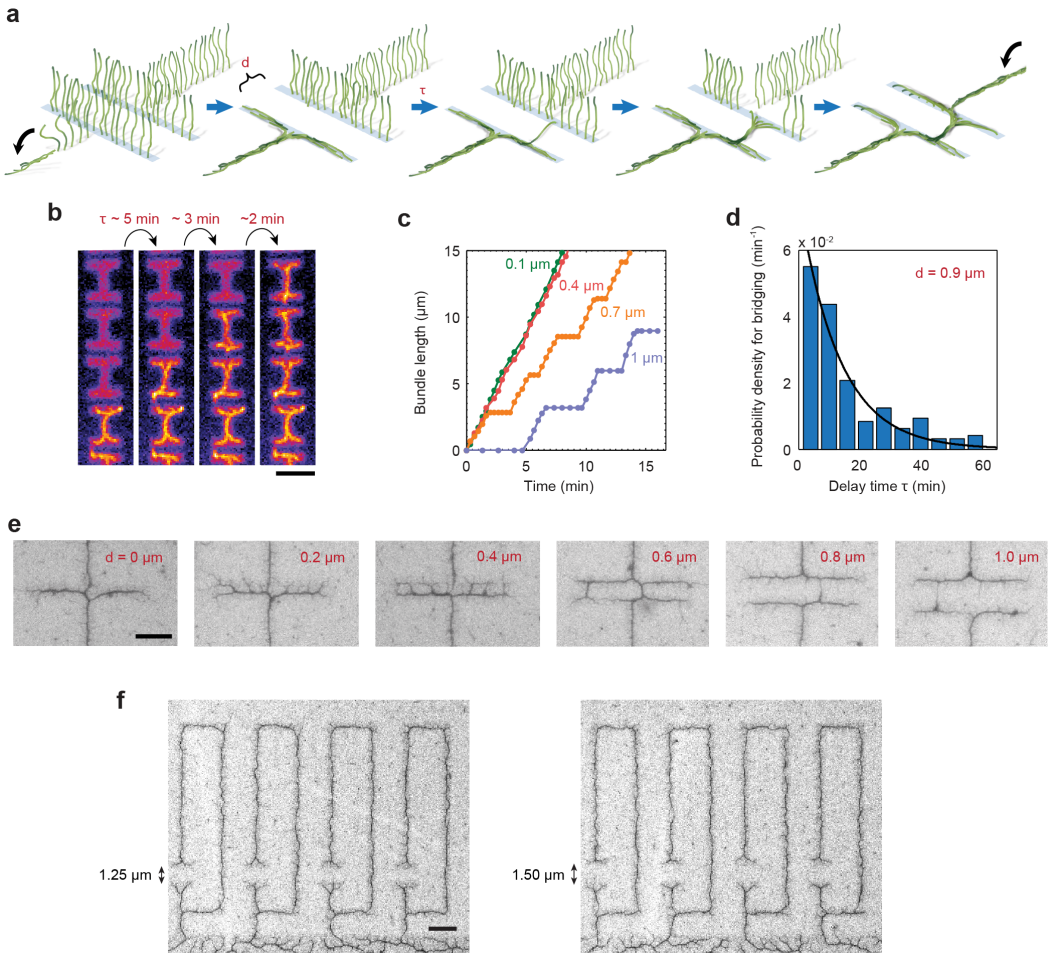

Figure 58: **Gap bridging.** **a**, Illustration of a condensation front reaching a gap of width d and spontaneously bridging it after a delay time τ. **b**, Time-lapse fluorescence images of a condensing brush (1 μm wide) with several gaps of 1 μm width. Even though the gaps were of the same width, a variety of delay times was observed. **c**, Tracking the condensation fronts in such brushes reveals a stepwise growth (blue and orange curves). In contrast, small gaps (< 0.6 μm) result in a (relatively) constant bundle growth (red and green curves), probably due to a continuous overlap of strands across the gaps. **d**, Normalised histogram ($n = 160$, 0.5 μm wide DNA brushes) of delay times for a gap of width $d = 0.9$ μm. The black line represents an exponential fit, $\mu^{-1} \exp(-\tau/\mu)$, to the data with an average bridging time $\mu \approx 13$ min. This probability density function is the result of a bridging probability which is constant in time - similar to radioactive decay. **e**, SEM images of bridged gaps (0.1 μm brush width). Many bridges per gap again hint at a strong overlap of DNA strands, while a singular bridge indicates a long delay time terminated by a spontaneous bridging event. **f**, Gaps larger than the DNA contour length (> 1 μm) block the condensation process (0.5 μm wide DNA brushes). The loops connecting both sides of the gaps prove that the gaps are not bridged by bundles, which are too thin for SEM to resolve, since in that case the loops would contain domain walls. Scale bar: b, 5 μm; e, 1 μm; f, 2 μm.

stopped, until the gap was spontaneously bridged by one or more strands from the non-condensed side (figure 58a-c). The observation of many such bridging events revealed that the delay times are exponentially distributed (figure 58d). Similar gaps of 0.9 μm width were later used as stochastic switches with two states ("bridged" or "not bridged") for the construction of stochastic circuits. Small gaps (< 0.6 μm) did not show a significant time delay, presumably due to a constant overlap of DNA strands from both sides, resulting in the fast formation of several bridges (figure 58e). Gaps larger than the contour length (> 1 μm) completely blocked the propagation of condensation (figure 58f).

In contrast to the gap designs shown in figure 58, gaps can also be simply inserted into linear brushes in order to regulate bundle growth. Figure 59 displays arrays of small brush islands separated by gaps of various widths. Shortly after the complete condensation of the line without gaps (figure 59c, top), the sample was dried and imaged in SEM. The positions of the condensation fronts revealed that large gaps considerably slow down the propagation of growth.

Apart from the interesting behaviour of gap bridging, the observations also support our hypothesis that the dynamics of brush condensation is governed by reaction-diffusion mechanisms and especially by the amount of condensed DNA in the vicinity of still uncondensed strands (sections 5.2 & 5.3).

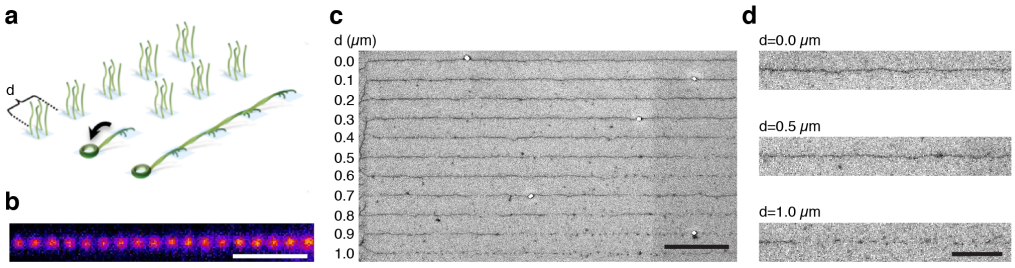

Figure 59: **Condensed brush arrays.** **a**, Condensation of an array of small brush islands separated by gaps of width d. **b**, Fluorescence image of non-condensed brush islands (diameter: 100 nm) separated by a distance $d = 0.9$ μm. **c**, SEM image of condensed arrays with a nucleation-prone region on the left. The positions of the condensation fronts at the time of drying suggest that large distances d considerably slow down the bundle growth. **d**, Magnified images from **c**. When the condensing sample was dried, arrays with small separating distances (*e.g.* $d = 0.5$ μm) had already formed long, continuous bundles. For $d = 1.0$ μm this time was too short, yielding only a short bundle and leaving the remaining islands uncondensed (black dots). Scale bars: b&c, 5 μm; d, 2 μm.

6.2.2 Stochastic Circuits

Inspired by the stochastic circuits described at the beginning of this section (6.2), we created DNA brushes resembling the circuits shown in figure 57c. Thereby, the switches were replaced by 0.9 μm wide gaps acting as stochastic circuit elements (figure 60a). Condensation of many replicas of these brushes was initiated at a nucleation-prone region and its progress could be tracked *via* fluorescence microscopy (figure 60b). Especially bridging events could be clearly observed in time-lapse images. We found that - similar to the original concept - the state of a DNA brush circuit (entirely "condensed" or "uncondensed") at a certain point in time depends on the arrangement of stochastic circuit elements. On average, circuits with two gaps in parallel condensed faster than circuits with a single element (figure 60c). A parallel arrangement in series with a single element was generally again slower, while two gaps in series resulted in the slowest circuit out of the four types.
The main difference to the original stochastic circuits is the time evolution of the condensing system. While the theoretical model treats all switches independently,

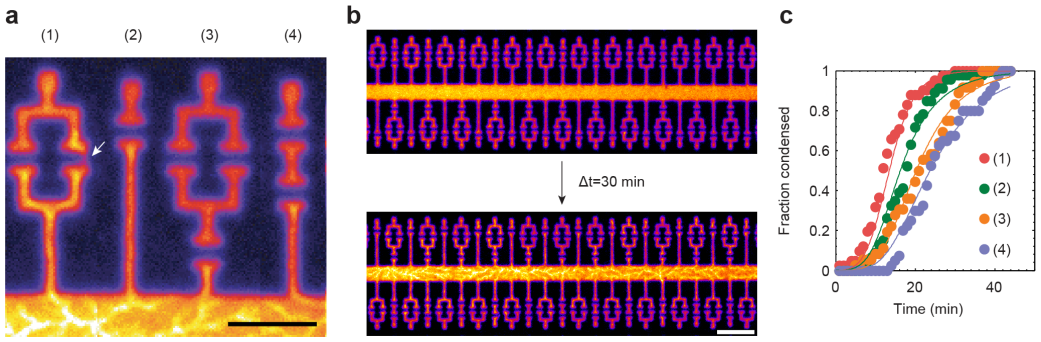

Figure 60: **Condensed stochastic circuits.** **a**, Fluorescence image (stitched) of four types of circuits with gaps as stochastic elements, connected to a nucleation-prone region (bottom): (1) two switches in parallel; (2) single switch; (3) two parallel switches in series with a single one; (4) two switches in series. The white arrow indicates a condensation bridge. **b**, Uncondensed brush (top) and condensing circuits (bottom, time interval $\Delta t = 30$ min). The circuits were arranged in alternating fashion along a nucleation-prone stripe in order to approximately synchronise their condensation. **c**, For each type of circuit ≈ 48 copies were analysed and for each of them the time of complete condensation was determined. From these times we constructed the four cumulative histograms over time (numbers (1)-(4) correspond to those in **a**). The propagation of condensation through the circuits is indeed influenced by the arrangement of gaps, *e.g.* causing the parallel circuit to condense fastest and the serial circuit slowest. The solid lines are fits to the data based on the model described on page 117. Scale bars: a, 5 μm; b, 10 μm.

our circuits condense in one direction, meaning that the second gap in a series cannot be bridged before the first one. Also, the different behaviour of the four types of circuits was only observable during a certain time window, because in the beginning and in the end all of our circuits were in the same state: "uncondensed" or "condensed", respectively. Since the formulas given in figure 57c do not apply to this dynamic system, we used the distribution of bridging times (figure 58d) to describe the time evolution of the different types of circuits.
The propagation of condensation was modelled as a series of waiting processes with their respective normalised waiting time distributions $w(t)$ (the probability for an event to occur in the time interval $[t, t + dt]$).
The first waiting time corresponds to the initial nucleation and growth of condensates on the central stripe connecting the circuits and providing (approximate) synchronisation. The time required for this growth process, which enables the condensation of the actual circuits, was assumed to follow a Gaussian distribution, since multiple domains nucleate and grow simultaneously:

$$w_0(t) = \frac{1}{\sqrt{2\pi}\sigma} e^{-\frac{(t-\mu)^2}{2\sigma^2}}$$

The waiting time distribution for bridging a single gap is exponentially distributed (confirmed experimentally; figure 58d):

$$w_s(t) = \lambda e^{-\lambda t}$$

Similarly, two gaps in parallel yield:

$$w_p(t) = 2\lambda e^{-2\lambda t}$$

In figure 58d not the probability densities of the waiting time distributions are displayed, but their integrated (cumulative) forms $W(t)$ (the number of circuits condensed *until* time t).

$$W(t) = \int_0^t w(x)\ dx$$

The functions $W(t)$ that model the four different circuits investigated here (single, parallel, serial, and combined) follow from the concatenation of two or three waiting processes. For the single element ($w_1 = w_s$) and the parallel arrangement ($w_1 = w_p$)

we thus used:

$$W(t) = \int_0^t w_0(x) \int_0^{t-x} w_1(y)\ dy\ dx$$

For the serial elements ($w_1 = w_2 = w_s$) and the combined serial-parallel arrangement ($w_1 = w_s$ & $w_2 = w_p$) we used:

$$W(t) = \int_0^t w_0(x) \int_0^{t-x} w_1(y) \int_0^{t-x-y} w_2(z)\ dz\ dy\ dx$$

These cumulative functions were then used to simultaneously fit the four curves obtained from a single experiment, resulting in a fitted parameter $\lambda \approx 0.1$ min^{-1} (with only a slight variation among experiments), which corresponds to an average bridging time of ≈ 10 min for a single gap and which roughly agrees with the analysis of single gaps (figure 58d).

If salt and buffer conditions were suitable for both DNA condensation and gene expression, condensing non-coding DNA brushes between gene brushes might be used for the spatiotemporal coordination of gene inhibition. Thereby, simple brush lines would yield rather deterministic time delays, while the circuits described above could contribute stochasticity to the regulation of genes. Adding stochasticity to synthetic gene expression systems could enhance their capabilities in modelling actual biological systems.

7 Conclusion and Outlook

In summary, we explored ways to generate biomolecular patterns on biochip surfaces on the micron and the nanometer scale, specifically by direct lithographic patterning and by self-assembly *via* DNA condensation.

Regarding the development of biochips, we enhanced the patterning possibilities of Daisy chips towards higher precision and presented the alternative method Bephore. In future experiments, we will use the multi-step lithographic capabilities of Bephore to spatially organise biomolecules and biochemical reactions on a chip, *e.g.* to separate transcription and translation of a gene, as illustrated in figure 61.

Our investigation of the condensation of linear DNA brushes resulted in the demonstration of a novel type of condensate that can be guided along arbitrarily shaped pathways. We further explored potential computational capabilities of the process towards the spatiotemporal coordination of gene expression.

A major hurdle towards this goal is the incompatibility of many biochemical processes and the salt concentrations required for spermidine-induced condensation. A potential remedy is the replacement of spermidine by protamines, histones or by a condensing agent called "AzoTAB" [112].

AzoTAB is an azobenzene-based condensing agent which can be toggled between a condensing and a non-condensing conformation by ultraviolet or blue illumination [113], and was already demonstrated to switch transcription in a cell-

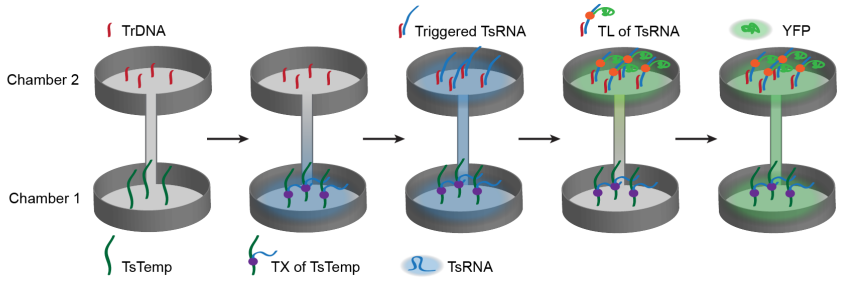

Figure 61: **Concept for the spatial separation of transcription and translation on a chip,** based on a "toehold switch" [111]. A gene (TsTemp) coding for a fluorescent protein (YFP) is immobilised in chamber 1. After the transcription (TX) of TsTemp to mRNA (TsRNA), translation is inhibited by the secondary structure of the RNA, which hides the ribosome binding site. The secondary structure is only opened by so-called "trigger-DNA" (TrDNA), which is immobilised in chamber 2, allowing for the translation (TL) of the fluorescent protein.

free expression system. Furthermore, AzoTAB might help to locally trigger nucleation and allow for the condensation of very large brushes from a single nucleation region.

On the other hand, histones and protamines represent naturally occurring condensing agents and might be expressed locally on a chip. Post-translational modifications of histones, *e.g.* by phosphorylation or methylation, would additionally increase the variety and specificity of condensation processes, potentially enabling the study of epigenetic mechanisms on a chip. Next to histones, protamines may be interesting candidates for protein-based condensation studies. They contain a large number of positively charged amino acids, *e.g.* 21 arginines on a total of 32 amino acids (salmon protamine [45]). In sperm cells, they condense DNA to partially ordered phases [114] and thereby disable gene transcription. *In vitro* condensation of DNA yielded toroidal structures similar to those formed from trivalent ions [55] and preliminary data of protamine condensation on a Bephore chip shows that protamines can form small dendritic structures even at high monovalent salt concentrations (figure 62). Whether these alternative condensing agents can also yield extended dendritic or one-dimensional bundles, remains to be explored in future experiments. Eventually, we hope that investigations of DNA brush interactions *via* biological, biophysical and biochemical processes will allow for the precise engineering of synthetic, complex genetic circuits. In some aspects, such systems may display cell-like behaviour and hence serve as precursors or testing ground towards the development of artificial biological systems.

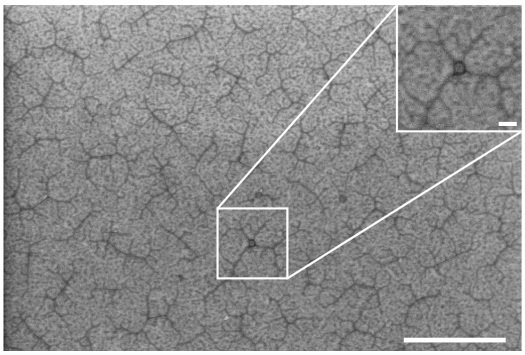

Figure 62: **DNA brush condensed by protamines.** SEM image of an extended DNA brush on a Bephore chip, condensed by 1 ng/μl of protamine from salmon in a 1×PBS solution. The image shows small dendritic domains and a toroidal nucleation site (inset). Scale bars: 1 μm; inset: 100 nm.

References

1. Buxboim, A. *et al.* A Single-Step Photolithographic Interface for Cell-Free Gene Expression and Active Biochips. *Small* **3,** 500–510 (2007).
2. Bracha, D., Karzbrun, E., Shemer, G., Pincus, P. A. & Bar-Ziv, R. H. Entropy-driven collective interactions in DNA brushes on a biochip. *Proc. Natl. Acad. Sci. U.S.A.* **110,** 4534–4538 (2013).
3. Bracha, D. & Bar-Ziv, R. H. Dendritic and Nanowire Assemblies of Condensed DNA Polymer Brushes. *J. Am. Chem. Soc.* **136,** 4945–4953 (2014).
4. Bar, M. & Bar-Ziv, R. H. Spatially resolved DNA brushes on a chip: gene activation by enzymatic cascade. *Nano Lett.* **9,** 4462–6 (2009).
5. Pardatscher, G. *et al.* DNA condensation in one dimension. *Nat. Nanotechnol.* **11,** 1076–1081 (2016).
6. Karzbrun, E., Tayar, A. M., Noireaux, V. & Bar-Ziv, R. H. Programmable on-chip DNA compartments as artificial cells. *Science* **345,** 829–832 (2014).
7. Tayar, A., Karzbrun, E., Noireaux, V. & Bar-Ziv, R. H. Propagating gene expression fronts in a one-dimensional coupled system of artificial cells. *Nat. Phys.* **11,** 1037–1041 (2015).
8. Kim, J., White, K. & Winfree, E. Construction of an in vitro bistable circuit from synthetic transcriptional switches. *Mol. Syst. Biol.* **2** (2006).
9. Montagne, K., Plasson, R., Sakai, Y., Fujii, T. & Rondelez, Y. Programming an in vitro DNA oscillator using a molecular networking strategy. *Mol. Syst. Biol.* **7,** 466–466 (2011).
10. Niederholtmeyer, H., Stepanova, V. & Maerkl, S. Implementation of cell-free biological networks at steady state. *Proc. Natl. Acad. Sci. U.S.A.* **110,** 15985–15990 (2013).
11. Caschera, F., Lee, J., Ho, K., Liu, A. & Jewett, M. Cell-free compartmentalized protein synthesis inside double emulsion templated liposomes with in vitro synthesized and assembled ribosomes. *ChemComm* **52,** 5467–5469 (2016).
12. Weitz, M. *et al.* Diversity in the dynamical behaviour of a compartmentalized programmable biochemical oscillator. *Nat. Chem.* **6,** 295–302 (2014).

13. Bracha, D., Karzbrun, E., Daube, S. S. & Bar-Ziv, R. H. Emergent Properties of Dense DNA Phases toward Artificial Biosystems on a Surface. *Acc. Chem. Res.* **47,** 1912–21 (2014).

14. Gosule, L. & Schellman, J. Compact form of DNA induced by spermidine. *Nature* **259,** 333–335 (1976).

15. Wilhelm, D. & Bruck, J. Stochastic switching circuit synthesis. *2008 IEEE International Symposium on Information Theory,* 1388–1392 (2008).

16. Sbirkova, H. & Shivachev, B. Crystal structure of a DNA sequence d(CGTGA ATTCACG) at 130K. *Bul.Chem.Commn.* **48,** 589–592 (2016).

17. Berman, H. *et al.* The Protein Data Bank. *Nucleic Acids Res.* **28,** 235–242 (2000).

18. Rose, A. & Hildebrand, P. NGL Viewer: a web application for molecular visualization. *Nucleic Acids Res.* **43,** 576–579 (2015).

19. Rose, A. *et al.* Web-based molecular graphics for large complexes. *Proceedings of the 21st International Conference on Web3D Technology,* 185–186 (2016).

20. Miescher, F. Ueber die chemische Zusammensetzung der Eiterzellen. *Hoppe-Seyler's Medicinisch-chemische Untersuchungen* **4,** 441–460 (1871).

21. Watson, J. D. & Crick, F. H. C. Molecular Structure of Nucleic Acids: A Structure for Deoxyribose Nucleic Acid. *Nature* **171,** 737–738 (1953).

22. Watson, J. D. & Crick, F. H. C. Genetical Implications of the Structure of Deoxyribonucleic Acid. *Nature* **171,** 964–967 (1953).

23. Seeman, N. C. Nucleic acid junctions and lattices. *J. Theor. Biol.* **99,** 237–247 (1982).

24. Yurke, B., Turberfield, A. J., Mills, A. P., Simmel, F. C. & Neumann, J. L. A DNA-fuelled molecular machine made of DNA. *Nature* **406,** 605–608 (2000).

25. Rothemund, P. W. Folding DNA to create nanoscale shapes and patterns. *Nature* **440,** 297–302 (2006).

26. Langecker, M. *et al.* Synthetic Lipid Membrane Channels Formed by Designed DNA Nanostructures. *Science* **338,** 932–936 (2012).

27. Kuzyk, A. *et al.* DNA-based self-assembly of chiral plasmonic nanostructures with tailored optical response. *Nature* **483,** 311–314 (2012).

28. Taub, F., JM, D. & Thompson, E. Sequential comparative hybridizations analyzed by computerized image processing can identify and quantitate regulated RNAs. *DNA* **2,** 309–27 (1983).

29. Hoheisel, J. Microarray technology: beyond transcript profiling and genotype analysis. *Nat. Rev. Genet.* **7,** 200–210 (2006).

30. Carrara, S. *et al.* Fully Integrated Biochip Platforms for Advanced Healthcare. *Sensors* **12,** 11013–11060 (2012).

31. Bochet, C. G. Photolabile protecting groups and linkers. *Perkin Trans.* **1,** 125–142 (2001).

32. Shimizu, Y. *et al.* Cell-free translation reconstituted with purified components. *Nat. Biotechnol.* **19,** 751–755 (2001).

33. Venter, J. *et al.* The sequence of the human genome. *Science* **291,** 1304–1351 (2001).

34. Ou, H. *et al.* ChromEMT: Visualizing 3D chromatin structure and compaction in interphase and mitotic cells. *Science* **357,** eaag0025 (2017).

35. Davey, C., Sargent, D., Luger, K., Maeder, A. & Richmond, T. Solvent Mediated Interactions in the Structure of the Nucleosome Core Particle at 1.9Å Resolution. *J. Mol. Biol.* **319,** 1097–1113 (2002).

36. Alberts, B. *et al. Molecular Biology of the Cell* (Garland Science, New York, USA, 2008).

37. Dame, R., Kalmykowa, O. & Grainger, D. Chromosomal Macrodomains and Associated Proteins: Implications for DNA Organization and Replication in Gram Negative Bacteria. *PLOS Genet.* **7,** e1002123 (2011).

38. Qian, Z. *et al.* A New Noncoding RNA Arranges Bacterial Chromosome Organization. *mBio* **6,** e00998–15 (2015).

39. Rill, R., Livolant, F., Aldrich, H. & Davidson, M. Electron microscopy of liquid crystalline DNA: direct evidence for cholesteric-like organization of DNA in dinoflagellate chromosomes. *Chromosoma* **98,** 280–286 (1989).

40. Livolant, F. Ordered phases of DNA in vivo and in vitro. *Physica A* (1991).

41. Chattoraj, D. K., Gosule, L. C. & Schellman, J. A. DNA condensation with polyamines II. Electron microscopic studies. *J. Mol. Biol.* **121,** 327–337 (1978).

42. Widom, J. & Baldwin, R. Cation-induced toroidal condensation of DNA studies with Co3+(NH3)6. *J. Mol. Biol.* **144,** 431–453 (1980).

43. Koltover, I., Wagner, K. & Safinya, C. R. DNA condensation in two dimensions. *Proc. Natl. Acad. Sci. U.S.A.* **97,** 14046–14051 (2000).

44. Rackstraw, B. J. *et al.* Microscopic Investigations into PEG-Cationic Polymer-Induced DNA Condensation. *Langmuir* **17,** 3185–3193 (2001).

45. Brewer, L., Corzett, M. & Balhorn, R. Protamine-induced condensation and decondensation of the same DNA molecule. *Science* **286,** 120–123 (1999).

46. Jordan, C., Lerman, L. & Venable, J. Structure and circular dichroism of DNA in concentrated polymer solutions. *Nature New Biol.* **236,** 67–70 (1972).

47. Eickbush, T. & Moudrianakis, E. The compaction of DNA helices into either continuous supercoils or folded-fiber rods and toroids. *Cell* **13,** 295–306 (1978).

48. Livolant, F., Levelut, A., Doucet, J. & Benoit, J. The highly concentrated liquid-crystalline phase of DNA is columnar hexagonal. *Nature* **339,** 724–726 (1989).

49. Evdokimov, Y., Platonov, A., Tikhonenko, A. & Varshavsky, Y. A compact form of double-stranded DNA in solution. *FEBS Lett.* **23,** 180–184 (1972).

50. Petrov, A. & Harvey, S. Packaging Double-Helical DNA into Viral Capsids: Structures, Forces, and Energetics. *Biophys. J.* **95,** 497–502 (2008).

51. Pelta, J., Livolant, F. & Sikorav, J. DNA aggregation induced by polyamines and cobalthexamine. *J. Biol. Chem.* **271,** 5656–5662 (1996).

52. Baeza, I. *et al.* Possible prebiotic significance of polyamines in the condensation, protection, encapsulation, and biological properties of DNA. *Orig. Life Evol. Biospheres* **21,** 225–242 (1992).

53. Hud, N. V. & Downing, K. H. Cryoelectron microscopy of λ phage DNA condensates in vitreous ice: The fine structure of DNA toroids. *Proc. Natl. Acad. Sci. U.S.A.* **98,** 14925–14930 (2001).

54. Lambert, O., Letellier, L., Gelbart, W. & Rigaud, J. DNA delivery by phage as a strategy for encapsulating toroidal condensates of arbitrary size into liposomes. *Proc. Natl. Acad. Sci. U.S.A.* **97,** 7248–7253 (2000).

55. Allen, M., Bradbury, E. & Balhorn, R. AFM analysis of DNA-protamine complexes bound to mica. *Nucleic Acids Res.* **25,** 2221–2226 (1997).

56. Plum, G., Arscott, P. & Bloomfield, V. Condensation of DNA by trivalent cations. 2. Effects of cation structure. *Biopolymers* **30,** 631–643 (1990).

57. Hud, N. & Vilfan, I. Toroidal DNA Condensates: Unraveling the Fine Structure and the Role of Nucleation in Determining Size. *Annu. Rev. Biophys. Biomol. Struct.* **34,** 295–318 (2005).

58. He, S., Arscott, P. & Bloomfield, V. Condensation of DNA by multivalent cations: Experimental studies of condensation kinetics. *Biopolymers* **53,** 329–341 (2000).

59. Conwell, C., Vilfan, I. & Hud, N. Controlling the size of nanoscale toroidal DNA condensates with static curvature and ionic strength. *Proc. Natl. Acad. Sci. U.S.A.* **100,** 9296–9301 (2003).

60. Shen, M., Downing, K., Balhorn, R. & Hud, N. Nucleation of DNA Condensation by Static Loops: Formation of DNA Toroids with Reduced Dimensions. *J. Am. Chem. Soc.* **122,** 4833–4834 (2000).

61. Marx, K. & Ruben, G. Evidence for hydrated spermidine-calf thymus DNA toruses organized by circumferential DNA wrapping. *Nucleic Acids Res.* **11,** 1839–1854 (1983).

62. Marx, K. A. & Ruben, G. C. Studies of DNA Organization in Hydrated Spermidine-Condensed DNA Toruses and Spermidine-DNA Fibres. *Journal of Biomolecular Structure and Dynamics* **1,** 1109–1132 (1984).

63. Schellman, J. & Parthasarathy, N. X-ray diffraction studies on cation-collapsed DNA. *J. Mol. Biol.* **175,** 313–329 (1984).

64. Böttcher, C., Endisch, C. & Fuhrhop, J. High-yield preparation of oligomeric C-type DNA toroids and their characterization by cryoelectron microscopy. *J. Am. Chem. Soc.* **120,** 12–17 (1998).

65. Russel, W. B., Saville, D. A. & Schowalter, W. R. *Colloidal Dispersions* (ed Batchelor, G. K.) (Cambridge University Press, 1989).

66. Gelbart, W. M., Bruinsma, R. F., Pincus, P. A. & Parsegian, A. DNA-Inspired Electrostatics. *Physics Today* **53,** 38–44 (2000).

67. Bloomfield, V. DNA condensation by multivalent cations. *Biopolymers* **44,** 269–282 (1997).

68. Yoo, J. & Aksimentiev, A. The structure and intermolecular forces of DNA condensates. *Nucleic Acids Res.* **44,** 2036–2046 (2016).

69. Rau, D., Lee, B. & Parsegian, V. Measurement of the repulsive force between polyelectrolyte molecules in ionic solution: hydration forces between parallel DNA double helices. *Proc. Natl. Acad. Sci. U.S.A.* **81,** 2621–2625 (1984).

70. Todd, B., Parsegian, V., Shirahata, A., Thomas, T. & Rau, D. Attractive Forces between Cation Condensed DNA Double Helices. *Biophys. J.* **94,** 4775–4782 (2008).

71. Kornyshev, A., Lee, D., Leikin, S. & Wynveen, A. Structure and interactions of biological helices. *Rev. Mod. Phys.* **79,** 943 (2007).

72. Senefelder, A. *Lehrbuch der Steindruckerey* (ed Schlichtegroll, F.) (Fleischmann, München, 1821).

73. McCord, M. A. & Rooks, M. J. *Handbook of Microlithography, Micromachining, and Microfabrication* (ed Rai-Choudhury, P.) chap. 2 (SPIE Optical Engineering Pr., Bellingham, Wash, 1997).

74. Rayleigh, J. W. S. XXXI. Investigations in optics, with special reference to the spectroscope. *Phil. Mag. S. 5* **8,** 261–274 (1879).

75. Abbe, E. Beitrage zur Theorie des Mikroskops und der mikroskopischen Wahrnehmung. *Archiv fuer Mikroskopische Anatomie* **9,** 413–420 (1871).

76. Vogele, K. *et al.* A Self-Assembled Active Plasmonic Waveguide with a Peptide-Based Thermo-Mechanical Switch. *ACS Nano* (2016).

77. Jones, J. On the Determination of Molecular Fields. II. From the Equation of State of a Gas. *Proc. Royal Soc. B* **106,** 463–477 (1924).

78. Binnig, G., Quate, C. & Gerber, C. Atomic Force Microscope. *Phys. Rev. Lett.* **56,** 930 (1986).

79. Martin, Y., Abraham, D. & Wickramasinghe, H. High-resolution capacitance measurement and potentiometry by force microscopy. *Appl. Phys. Lett.* **52,** 1103–1105 (1988).

80. Schönenberger, C. Charge flow during metal-insulator contact. *Phys. Rev. B* **45,** 3861–3864 (1992).

81. Cohen, H. *et al.* Polarizability of G4-DNA Observed by Electrostatic Force Microscopy Measurements. *Nano Lett.* **7,** 981–986 (2007).

82. Lei, C., Das, A., Elliott, M. & Macdonald, J. Quantitative electrostatic force microscopy-phase measurements. *Nanotechnology* **15,** 627–634 (2004).

83. Fumagalli, L., Edwards, M. & Gomila, G. Quantitative electrostatic force microscopy with sharp silicon tips. *Nanotechnology* **25,** 495701 (2014).

84. Sun, Z. *et al.* Protocols for Implementing an Escherichia coli Based TX-TL Cell-Free Expression System for Synthetic Biology. *J. Vis. Exp.* 50762 (2013).

85. Sun, Z., Yeung, E., Hayes, C. A., Noireaux, V. & Murray, R. Linear DNA for Rapid Prototyping of Synthetic Biological Circuits in an Escherichia coli Based TX-TL Cell-Free System. *ACS Synth. Biol.* **3,** 387–397 (2014).

86. Krsko, P., Sukhishvili, S., Mansfield, M., Clancy, R. & Libera, M. Electron-Beam Surface-Patterned Poly(ethylene glycol) Microhydrogels. *Langmuir* **19,** 5618–5625 (2003).

87. Christman, K. L. *et al.* Positioning Multiple Proteins at the Nanoscale with Electron Beam Cross-Linked Functional Polymers. *J. Am. Chem. Soc.* **131,** 521–527 (2009).

88. Bae, M., Gemeinhart, R. A., Divan, R., Suthar, K. J. & Mancini, D. C. Fabrication of poly(ethylene glycol) hydrogel structures for pharmaceutical applications using electron beam and optical lithography. *J. Vac. Sci. Technol. B* **28,** C6P24–C6P29 (2010).

89. Lau, U. Y., Saxer, S. S., Lee, J., Bat, E. & Maynard, H. D. Direct Write Protein Patterns for Multiplexed Cytokine Detection from Live Cells Using Electron Beam Lithography. *Acs Nano* **10,** 723–729 (2016).

90. Seiler, H. Secondary electron emission in the scanning electron microscope. *J. Appl. Phys.* **54,** R1–R18 (1983).

91. Olejnik, J., Sonar, S., E, K. & Rothschild, K. Photocleavable biotin derivatives: a versatile approach for the isolation of biomolecules. *Proc. Natl. Acad. Sci. U.S.A.* **92,** 7590–7594 (1995).

92. Huang, F., Xu, H., Tan, W. & Liang, H. Multicolor and Erasable DNA Photolithography. *ACS Nano* **8,** 6849–6855 (2014).

93. Chirieleison, S. M., Allen, P. B., Simpson, Z. B., Ellington, A. D. & Chen, X. Pattern transformation with DNA circuits. *Nat. Chem.* **5,** 1000–1005 (2013).

94. Berggren, K. & Pepper, M. Electrons in one dimension. *Philos. Trans. Royal Soc. A* **368,** 1141–1162 (2010).

95. Schwabl, F. *Statistische Mechanik* 3rd ed. (Springer, Berlin, 2006).

96. Gillespie, D. T. A general method for numerically simulating the stochastic time evolution of coupled chemical reactions. *J. Comput. Phys.* **22,** 403–434 (1976).

97. Bockrath, M. *et al.* Scanned Conductance Microscopy of Carbon Nanotubes and λ-DNA. *Nano Lett.* **2,** 187–190 (2002).

98. Bloomfield, V. Condensation of DNA by multivalent cations: considerations on mechanism. *Biopolymers* **31,** 1471–1481 (1991).

99. Euler, L. Solutio problematis ad geometriam situs pertinentis. *Commentarii academiae scientiarum Petropolitanae* **8,** 128–140 (1735).

100. Cormen, T. H., Leierson, C. E., Rivest, R. L. & Stein, C. *Introduction to Algorithms* 3rd ed. (The MIT Press, 2009).

101. Kern, H. *Through the labyrinth: designs and meanings over 5000 years* (Prestel, Munich, 2000).

102. Nakagaki, T., Yamada, H. & Tóth, A. Maze-solving by an amoeboid organism. *Nature* **407,** 470 (2000).

103. Reyes, D., Ghanem, M., Whitesides, G. & Manz, A. Glow discharge in microfluidic chips for visible analog computing. *Lab Chip* **2,** 113–116 (2002).

104. Fuerstman, M. *et al.* Solving Mazes Using Microfluidic Networks. *Langmuir* **19,** 4714–4722 (2003).

105. Steinbock, O., Tóth, A. & Showalter, K. Navigating complex labyrinths: optimal paths from chemical waves. *Science* **267,** 868–71 (1995).

106. Dec. 2016. <`http://www.nature.com/nnano/journal/v11/n12/covers/index.html`>.

107. Aug. 2016. <`http://www.nature.com/news/floods-fires-zika-and-a-hidden-portrait-1.20493?WT.mc_id=FBK_NatureNews`>.

108. Oct. 2016. <`http://www.spektrum.de/magazin/labyrinth-aus-kondensiertem-erbgut/1422601`>.

109. Ten years in images. *Nat. Nanotechnol.* **11,** 836–840 (2016).

110. Dijkstra, E. A note on two problems in connexion with graphs. *Numer. Math.* 269–271 (1959).

111. Green, A., Silver, P., Collins, J. & Yin, P. Toehold Switches: De-Novo-Designed Regulators of Gene Expression. *Cell* **159,** 925–939 (2014).

112. Estévez-Torres, A. *et al.* Sequence-independent and reversible photocontrol of transcription/expression systems using a photosensitive nucleic acid binder. *Proc. Natl. Acad. Sci. U.S.A.* **106,** 12219–12223 (2009).

113. Ny, A. & Lee, C. Photoreversible DNA Condensation Using Light-Responsive Surfactants. *J. Am. Chem. Soc.* **128,** 6400–6408 (2006).

114. Blanc, N., Senn, A., Leforestier, A., Livolant, F. & Dubochet, J. DNA in Human and Stallion Spermatozoa Forms Local Hexagonal Packing with Twist and Many Defects. *J. Struct. Biol.* **134,** 76–81 (2001).

Appendix

Additional Figures

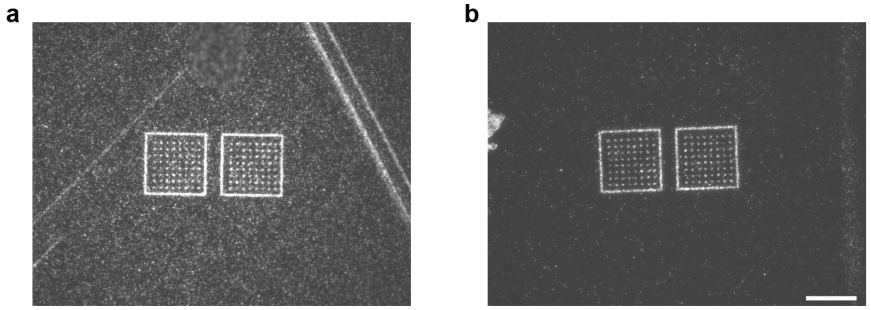

Figure 63: **Passivation of Daisy before EBL.** Fluorescently labelled DNA origami structures attached to a Daisy chip patterned *via* EBL: **a,** without prior passivation, **b,** with passivation using Methyl-$(PEG)_8$-NHS Ester. Scale bar: 20 μm.

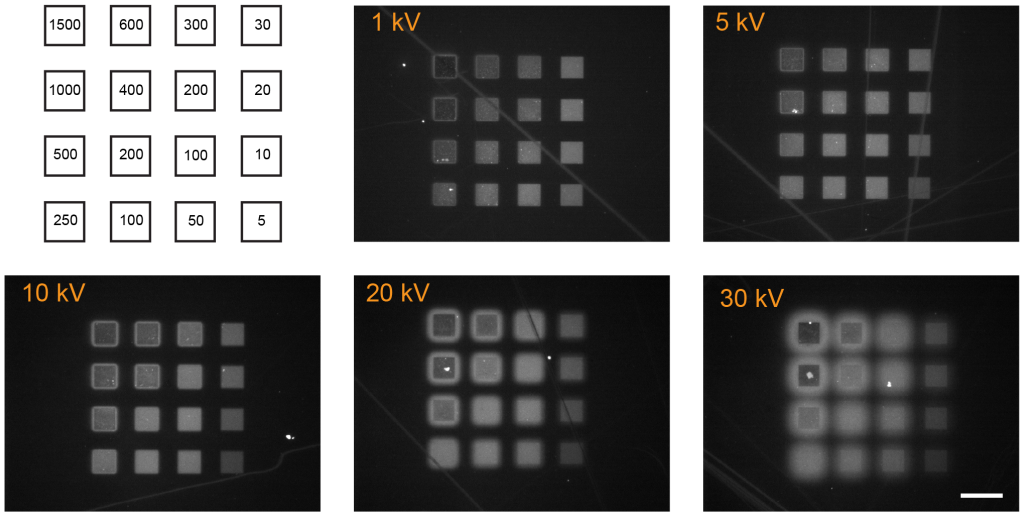

Figure 64: **EBL dose tests on Daisy.** Fluorescence images of Alexa Fluor 647-labelled streptavidin bound to squares written *via* EBL at different acceleration voltages. The numbers in the squares indicate the electron doses used for the dose tests (in $\mu C/cm^2$). Scale bar: 20 μm.

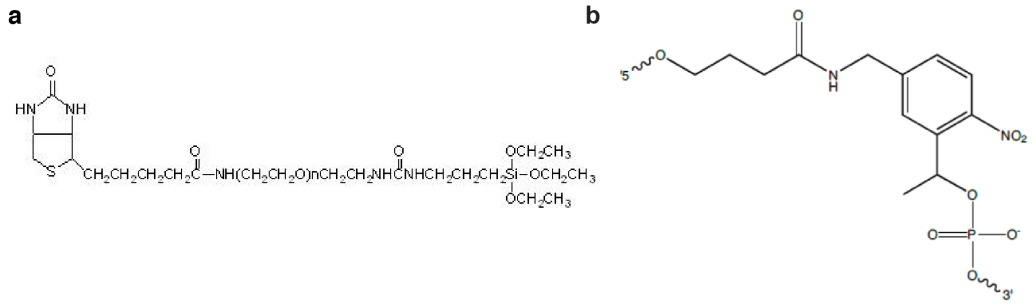

Figure 65: **Biotin-PEG-Silane and PC linker. a,** Chemical structure of the heterobifunctional PEG used to coat silicon dioxide surfaces as part of Bephore. **b,** Photocleavable linker in the PC strand of Bephore.
a, Adapted from Laysan Bio, Inc.; `http://laysanbio.com/index.php?src=directory&view=products&category=BIO-SIL-5K&submenu=Products` (accessed 4 May, 2017)
b, Adapted from Integrated DNA Technologies, Inc.; `https://eu.idtdna.com/pages/decoded/decoded-articles/oligo-modifications/decoded/2012/04/26/modification-highlight-photo-cleavable-spacer` (accessed 4 May, 2017); licensed from Ambergen, Inc., Watertown, MA 02472, USA.

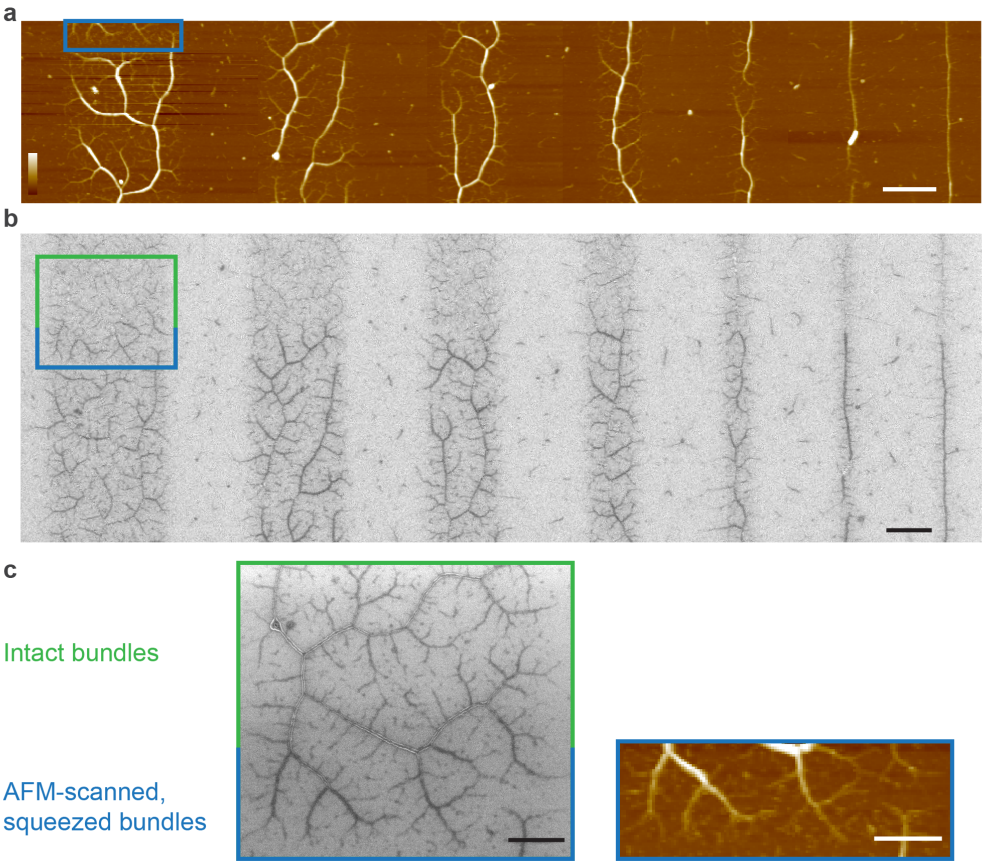

Figure 66: **Flattening of DNA bundles by AFM scans. a,** AFM scans of DNA bundles prepared *via* the gentle drying procedure (montage of several scans). **b,** SEM image of the same area as in **a**. **c,** Zoom-in images of the highlighted regions in **a** and **b**. Bundles in the scanned region appear dark, similar to bundles dried *via* the fast procedure (see section 3.4.5), indicating a degradation of the bundles by AFM scanning. Also a comparison of bundle widths measured in AFM and SEM (figures 33b and 34c) suggests a flattening of condensates by AFM. Scale bars: a&b, 1 μm; c, 500 nm; height bar: 20 nm.

DNA Sequences

Name	5' Sequence 3'
a) Bephore	
PC	BTTGCCGGTTGATTGATTTAGGAGTAGTGAGCGCGATAGGC PTTTTTGCCTATCG
PH	CGCTCACTACTCCTAAATCAATCAACCGGC
DIS	CTATCGCGCTCACTACTCCTAAATCAATCAACCGGC
FL+DIS	FL CTATCGCGCTCACTACTCCTAAATCAATCAACCGGC
b) Primers	
Fwd (Primer)	TGCCACCTGACGTCTAAGAA
DIS+TT+S+TT+Fwd	CTATCGCGCTCACTACTCCTAAATCAATCAACCGGCTTSTTT GCCACCTGACGTCTAAGAA
Rev (Primer)	ATTACCGCCTTTGAGTGAGC
FL+TT+Rev	FLTTATTACCGCCTTTGAGTGAGC

B: Biotin
P: Photocleavable spacer, IDT
S: Spacer 9, IDT (triethylene glycol spacer)
FL: ATTO 425, ATTO 532 or Alexa Fluor 647

Table 1: **a,** DNA strands used as components in Bephore. **b,** Primers for the generation of linearised templates for fluorescent proteins. Modifications are coloured in red. DNA strands were purchased from Integrated DNA Technologies Inc. (IDT) and biomers.net GmbH (Ulm, Germany).

Fwd Primer – T7 promoter – RBS (BBa_B0034) - mTurquoise2 – T7 Terminator – **Rev Primer**
tgccacctgacgtctaagaaattcaggatcccttaatacgactcactatagggagagtttaaagtcagtaaagaggagaaatag acatggttagcaagggtgaagaactgttcaccggcgtcgtgccgattctggttgagctggatggtgatgtcaacggtcacaagttta gcgttagcggtgagggcgagggcgacgccacctacggtaaattgaccctgaagtttatctgcacgaccggtaagctgccggttcc gtggccgaccctggtgacgactctgtcgtggggcgtgcaatgtttcgcgcgctatccggatcacatgaaacagcatgacttctttaa gagcgcgatgccggaaggctacgttcaggaacgtacgatcttttttcaaagacgacggtaactataagacccgcgcagaagtcaa gttcgagggtgacacgctggtgaatcgtattgagctgaaaggtattgactttaaagaggacggtaacatcctgggtcacaaactgg agtataattacttcagcgacaatgtgtacatcaccgctgataaacagaaaaacggcattaaagcaaacttcaagatccgtcacaat attgaagatggcggcgtgcaattggccgatcactatcaacagaacaccccgattggcgatggtccggtcctgctgccagataatc actacttgagcacgcaatccaaactgtccaaagatccgaacgaaaaacgtgaccacatggtcctgctggaatttgttaccgcggc gggtatcacgctgggtatggacgaactgtacaagacccgtggtggcggcggcagcagcggtccgcgtcctcgtggtacccgcgg taagggtcgtcgcattcgtcgttaataatggtacctactagcataaccccttggggcctctaaacgggtcttgaggggttttttg**gctca** **ctcaaaggcggtaat**

Fwd Primer– T7 promoter – RiboJ - RBS (BBa_B0034) - YPet – Terminator (ECK120033737) - **Rev Primer**
tgccacctgacgtctaagaaaccattattatcatgacattaacctataaaaataggcgtatcacgaggcagaatttcagataaaa aaaatccttagctttcgctaaggatgatttctggaattcgagtaagcccctctagaggaccacgcatcgtgatgcctatgcgcggtag tcccaccttgtccactagaatggaagattggcacgtatcaagactttggagtagtaccataacgccgtaatacgactcactataggg tagcgcagcgctcaacgggtgtgcttcccgttctgatgagtccgtgaggacgaaagcgcctctacaaataattttgtttaatcatgag aaagaggagaaaactagatgtctaaaggtgaagaactgtttacgggtgtcgtgccgattctggtcgagttggacggcgacgtgaa cggtcacaaattcagcgtgagcggcgagggcgagggtgacgcgacgtacggtaagctgactctgaagctgctgtgcaccacgg gtaaattgccggttccgtggccgaccctggtcacgacgctgggttatggtgtacaatgttttgcacgctatccggaccacatgaaac agcacgatttcttcaagagcgcgatgccggaaggctatgttcaggaacgtaccatctttttcaaagatgatggtaattacaaaaccc gcgcagaagtgaagttcgagggtgacaccctggtgaaccgtattgagctgaagggtattgacttcaaggaagatggcaatattctg ggtcacaaactggagtacaactataacagccataacgtctacatcaccgcggataagcaaaaaaatggtatcaaagcaaatttc aagattcgccacaacatcgaagatggcggcgtgcaactggccgatcattatcagcagaataccccaatcggtgacggtccggtg ctgttgccggataaccactacctgagctatcaaagcgcgttgttcaaagacccgaatgaaaaacgtgaccacatggttctgctgga atttctgaccgctgcgggcatcactgaaggcatgaatgaactgtacaagacgcgtggtggcggcggttcgatgagcaagactatc gttttgtccgtcggcgaggctacccgtaccttgaccgaaattcaatccaccgcggaccgtcaaatttttgaggaaaaagtcggtcctc tggtgggtcgtctgcgtctgaccgcgagcctgcgccagaacggtgccaaaacggcataccgtgttaatctgaaactggatcaggc cgacgttgtggacagcggtctgccgaaagtccgctacacccaggtgtggagccacgatgtgacgatcgttgcgaatagcaccga agcgagccgcaagagcctgtacgacctgaccaagagcctggtggcaacgtcccaagttgaagatctggttgttaacctggtgcc gctgggtcgttaaagcatgccggaggaaacacagaaaaaagcccgcacctgacagtgcgggctttttttttcgaccaaaggggtg catactagtagcggccgctgcagtccggcaaaaaagggcaaggtgtcaccaccctgccctttttctttaaaaccgaaaagattactt cgcgttatgcaggcttcctcgctcactgactcgctgcgctcggtcgttcggctgcggcgagcggtatca**gctcactcaaaggcggt** **aat**

Table 2: Top: DNA sequence for the cyan fluorescent protein (CFP) mTurquoise2. Bottom: Sequence for the yellow fluorescent protein (YFP) YPet.

Fwd Primer - T7 promoter – RBS (BBa_B0034)– mScarlet - AAV- Terminator (ECK120033737) –Spacer – **Rev Primer**
tgccacctgacgtctaagaaaaggaatattcagcaatttgcccgtgccgaagaaaggcccacccgtgaaggtgagccagtga gttgattgctacgtaattagttagttagcccttagtgactcgaattctaatacgactcactatagggtactagagaaagaggagaaaa tggtgtcaaagggagaggcggttatcaaggaatttatgcgctttaaagtccacatggagggcagcatgaacgggcacgagtttga aattgagggggagggggagggccgtccttatgaaggtactcagactgctaaactgaaggtgacaaaaggtggccccttgcctttc tcgtgggacatcctgtcgccacaattcatgtacgggagccgcgcctttatcaaacatcccgcagatattcctgattactataaacaat ctttcccggaaggtttcaaatgggaacgcgtcatgaattttgaggacgggggcgctgtcacagttactcaggacacctccttggaag acggcacattgatttacaaggttaagttgcgcggcacaaacttccccccctgacgggccagtaatgcaaaagaaaactatgggttg ggaggcgtctacagaacgtttataccccgaagacggggtgctgaaaggtgacattaagatggccctgcgcctgaaggacggcg gtcgctatcttgccgactttaaaactacttataaggctaaaaaaccagtccagatgccaggcgcctataatgttgaccgcaagttag acatcacctcacataatgaagactataccgttgtagaacaatacgagcgcagcgagggtcgtcacagtaccgggggggatggatg aattatacaaacgtcctgctgcgaacgacgaaaattatgcggctgcggtttgataaggaaacacagaaaaaagcccgcacctga cagtgcgggctttttttttcgaccaaaggttaattaaacctataggatcgtataggtttacgcaagaaaatggtttgttatagtcgaataa acctaggccccccgaggagtagcacatgattgtgcaaatcggccgccgtgaggagttcgataaaaagctgcttggggaaatgca taaacttcgtgctcaggtgttcaaggagcgtaaggggtgggatgtttccgttattgacgaaatggaaattgatgggtacgatgcattat caccttactatatgctgattcaagaagacacacctgaggcccaggtattcggttgctggcgcatttttgacacgacggggccttacat gttgaagaacacgtttcctgaattgttacacggcaaagaagctccctgctcaccccatatttgggaactgagccgtttcgctatcaatt ccggtcaaaagggctccctgggcttttcggactgcacccttgaagccatgcgcgcacttgcccgttactccctgcaaaacgacattc aaaccttagttactgttactaccgttggcgtagagaagatgatgatccgtgcgggtcttgacgtatctcgctttggaccgcatctgaag attggaatcgagcgtgcggtggcgttgcgcatcgaattgaacgcaaaaacgcaaattgcgttatacggcggggtcttggttgaaca gcgtttagccgtgagttgataatccggcaattaaaaaagcggctaaccacgccgctttttttacgtctgcactgcaggagtcactaag ggttagttagttagattagcagaaagtcaaaagcctccgaccggaggcttttgactaaaacttcccttggggttatcattggg**gctca ctcaaaggcggtaat**

Table 3: DNA sequence for the red fluorescent protein (RFP) mScarlet I.

Danksagung

Zum Abschluss meiner Promotionszeit blicke ich auf spannende Jahre am Lehrstuhl E14 zurück, auf wissenschaftliche und technische Herausforderungen, auf deren gemeinsame Bewältigung, auf interessante Diskussionen, Konferenzen und Forschungsreisen. Allen voran verdanke ich dies Professor Friedrich Simmel, der mir die Möglichkeit zur Promotion eröffnete, mich bei der Umsetzung der Projekte stets unterstützte und mir auch den Freiraum zur Entwicklung eigener Ideen bot. Hierfür ein herzliches Dankeschön!

Ich danke allen Mitarbeitern und Kollegen des Lehrstuhls für ihre Hilfsbereitschaft und die konstruktiven Anregungen, für die freundschaftliche Atmosphäre und die gemeinsamen Erlebnisse während der Arbeitszeit und darüber hinaus. Besonders möchte ich an dieser Stelle auch Helene Budjarek und Susanne Kinzel für ihre Hilfe bei verwaltungs- und laborbezogenen Fragen meinen Dank aussprechen, außerdem Ali und Matthaeus für ihre konstruktiven Anmerkungen zu der vorliegenden Arbeit. Des Weiteren bedanke ich mich bei den ehemaligen Mitarbeitern Anton Kuzyk und Max Scheible, deren Einfluss auch in dieser Abschlussarbeit noch nachwirkt.

Ich danke auch den Mitarbeitern des Physik-Departments, die mir im Laufe meiner Arbeit behilflich waren, im Besonderen dem Lehrstuhl Dietz und den Mitarbeitern des WSI, hier besonders Peter Weiser für die Unterstützung im Reinraum.

Meine Forschungsaufenthalte am Weizmann Institut in Israel zählen sicherlich zu den besonderen Erfahrungen im Laufe dieser Jahre. Hierbei bedanke ich mich bei Professor Roy Bar-Ziv und Dan Bracha sowie der ganzen Gruppe für ihre Gastfreundschaft und die gelungene wissenschaftliche Zusammenarbeit.

Für die großzügige finanzielle Unterstützung der Forschungsprojekte und der internationalen Kollaboration danke ich der Volkswagen Stiftung.

Zum Schluss möchte ich mich bei meiner Familie, Steffi und allen Freunden bedanken, die mich durch diese Zeit begleitet haben.

Four Years in Microscopy Images

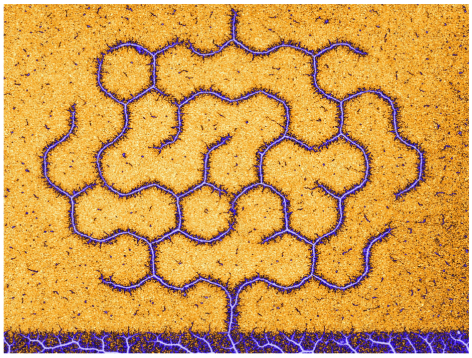

Small DNA maze (SEM, figure 55)

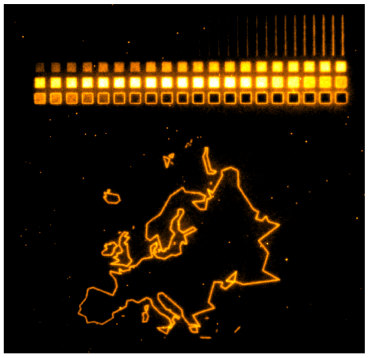

EBL dose test (figure 25) and geographical map of Europe (fluorescence)

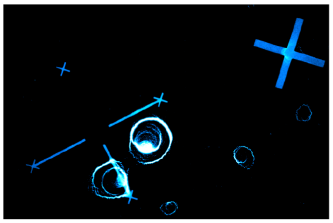

Fluorescently labelled DNA origami printed from a lithographically patterned silicon chip to a glass slide (fluorescence). Spirals are artefacts from drying.

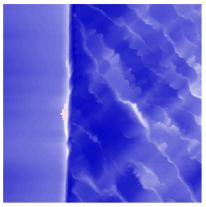

Masked silicon etching; left: gold, right: etched silicon (AFM)

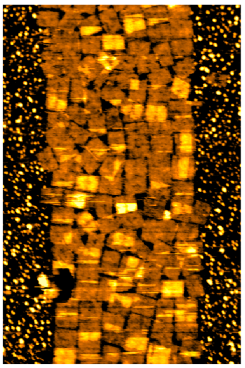

DNA origami structures on a lithographically patterned stripe (AFM)

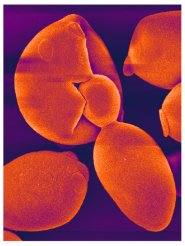

Yeast cells (SEM, prepared by Kaian Hoi, TUM)

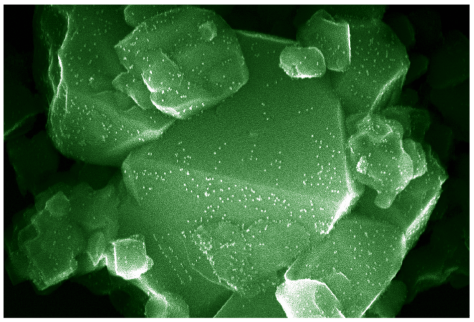

Silica particle covered with DNA origami carrying gold nanoparticles (SEM, prepared by Kilian Vogele, TUM)

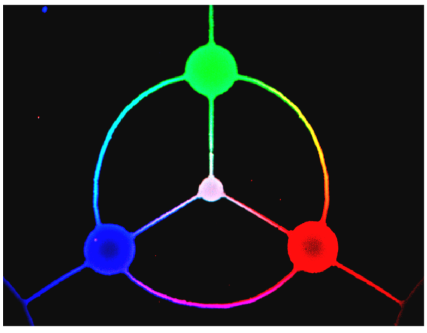

Multi-colour gene expression (fluorescence, figure 29)

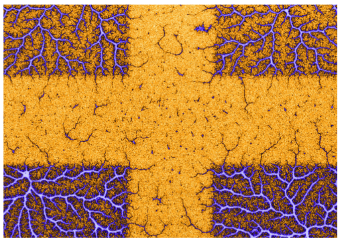

Condensed DNA brush squares (SEM)

The Tiger (fluorescence, figure 24) - miniaturised replica of Franz Marc's oil painting "Tiger" (1912)

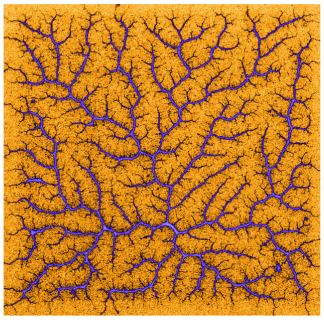

Dendritic condensate (SEM)

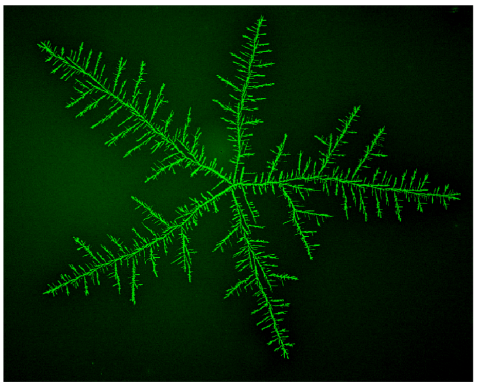

Chip dried during PEG-silanisation (SEM)

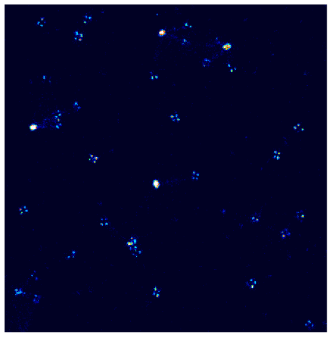

Rectangular DNA origami labelled with four docking sites for DNA PAINT super-resolution microscopy (reconstructed from TIRF microscopy)

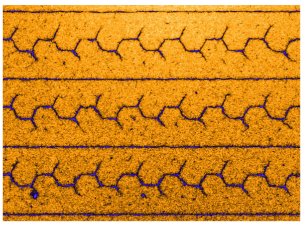

Guided growth of DNA bundles (SEM)

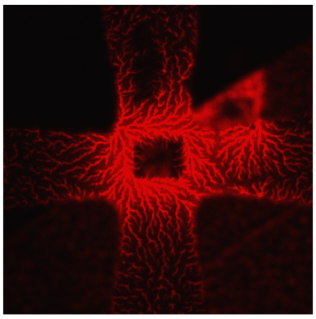

Alignment mark on a Daisy chip with condensed DNA (fluorescence). The dark square results from overexposure during the ebeam adjustment.

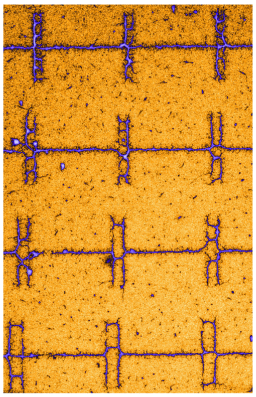

Condensed "capacitor"-shaped DNA brushes (SEM)

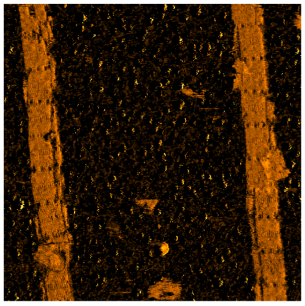

DNA origami structures on lithographically defined stripes (AFM)

Abstract

The immobilisation of DNA on a solid substrate enables the *in vitro* observation of biochemical and biophysical processes under strictly defined conditions.

First, we here assembled and characterised brushes of DNA on two types of biocompatible silicon chips. “Daisy”-biochips were developed in R. H. Bar-Ziv’s lab to investigate gene expression from lithographically patterned DNA brushes. We augmented the capabilities of the Daisy system with electron beam lithography, thereby increasing the patterning precision from the micrometer- to the nanometer-scale. Additionally, we developed an alternative resist termed “Bephore”, which is especially suited for multi-step lithography and assembled entirely from commercially available materials.

On Daisy chips, we applied electron beam lithography to create thin DNA brush stripes and to investigate DNA condensation by trivalent spermidine, *i.e.* the compaction of DNA from a brush-like conformation to a dense, bundled phase. DNA molecules of 1 µm length were patterned as brush stripes of various widths and condensed by the addition of spermidine. Starting in a nucleation site, condensates grew similar to a domino effect by adsorbing neighbouring DNA strands and forming elongated bundles. With decreasing brush width, we observed changes in morphology and condensation dynamics from two-dimensional, dendritic condensates to one-dimensional DNA bundles. In contrast to previously described DNA condensates, 1D bundles could be guided over tens of micrometers along arbitrary pathways.

Eventually, we explored the condensation of extensive DNA brush networks. We tracked bundle growth through a maze-shaped brush to determine the fastest route through the maze. Also, we tuned the propagation of condensation *via* delay elements inspired by a computer model of “stochastic switches”.